



저작자표시-비영리-변경금지 2.0 대한민국

이용자는 아래의 조건을 따르는 경우에 한하여 자유롭게

- 이 저작물을 복제, 배포, 전송, 전시, 공연 및 방송할 수 있습니다.

다음과 같은 조건을 따라야 합니다:



저작자표시. 귀하는 원저작자를 표시하여야 합니다.



비영리. 귀하는 이 저작물을 영리 목적으로 이용할 수 없습니다.



변경금지. 귀하는 이 저작물을 개작, 변형 또는 가공할 수 없습니다.

- 귀하는, 이 저작물의 재이용이나 배포의 경우, 이 저작물에 적용된 이용허락조건을 명확하게 나타내어야 합니다.
- 저작권자로부터 별도의 허가를 받으면 이러한 조건들은 적용되지 않습니다.

저작권법에 따른 이용자의 권리는 위의 내용에 의하여 영향을 받지 않습니다.

이것은 [이용허락규약\(Legal Code\)](#)을 이해하기 쉽게 요약한 것입니다.

[Disclaimer](#)

공학박사 학위논문

# Nanophotonic Engineering of Light–Matter Interactions in Organic Optoelectronic Devices

유기 광전자소자에서의 빛–물질 사이  
상호작용의 나노광학적 제어

2020 년 2 월

서울대학교 융합과학기술대학원  
나노융합학과

김형채



공학박사 학위논문

# Nanophotonic Engineering of Light–Matter Interactions in Organic Optoelectronic Devices

유기 광전자소자에서의 빛–물질 사이  
상호작용의 나노광학적 제어

2020 년 2 월

서울대학교 융합과학기술대학원  
나노융합학과

김 형 채



# Nanophotonic Engineering of Light–Matter Interactions in Organic Optoelectronic Devices

지도교수 김 창 순

이 논문을 공학박사 학위논문으로 제출함

2020 년 1 월

서울대학교 융합과학기술대학원

나노융합학과

김 형 채

김 형 채의 공학박사 학위논문을 인준함

2020 년 1 월

위 원 장	<u>김 연 상</u>	인
부위원장	<u>김 창 순</u>	인
위 원	<u>김 선 경</u>	인
위 원	<u>송 윤 규</u>	인
위 원	<u>이 강 원</u>	인



# Abstract

## Nanophotonic Engineering of Light–Matter Interactions in Organic Optoelectronic Devices

Hyungchae Kim

Department of Nano Science and Technology  
Graduate School of Convergence Science and Technology  
Seoul National University

Optical properties of materials are influenced not only by their inherent characteristics but also by the electromagnetic environment. The nanocavity composed of metal–dielectric–metal is a widely used nanophotonic platform to control the electromagnetic environment due to the high photonic density of states in the dielectric region. For example, a light-emitting diode or photodiode based on the cavity structure enhances photon emission or absorption. In addition, the cavity structure can be used as a platform to realize perfect absorbers and ultrafast emitter that do not exist in nature. Another example that has recently emerged is chiral plasmonics. If the structure have chirality, the molecules coupled to the cavity modes can selectively emit or absorb circularly polarized light depending on the helicity.

The aim of this study is to control the electromagnetic environment of organic optoelectronic devices, e.g., organic light-emitting diodes (OLED), organic solar cells (OSC), and organic photodiodes (OPD), thereby improving their performances or inducing new functionality. Organic materials are chosen as the photoactive media since they have excellent emission and absorption

properties even in a subwavelength scale device. In addition, it is easy to control the polarizability, desirable for tailoring the light–matter interaction. One dimensional nanophotonic engineering will be demonstrated to solve the problems, such as low light absorption in the near-infrared region and the severe thermalization loss. I will propose two types of solar cell structures and show how to design them considering nanophotonic phenomena. Next, I will demonstrate a numerical simulation of circularly polarized light emitting organic diodes for deep understanding of their optical and chiroptical characteristics. Finally, a promising chiral plasmonic platform consisting of a chirally patterned metal–dielectric–metal (chiral MDM) structure will be demonstrated to overcome the fundamental tradeoff between the quantum efficiency and the dissymmetry factor of chiral optoelectronics.

**Keywords:** nanophotonics, plasmonics, organic light emitting diodes, organic solar cells, organic photodetectors, organic semiconductor, chirality

**Student Number:** 2011-23984

# Contents

<b>Abstract</b>	<b>i</b>
<b>1 Introduction</b>	<b>1</b>
1.1 Nanophotonic Engineering for Organic Optoelectronics . . . . .	1
1.1.1 Organic Molecules . . . . .	1
1.1.2 Optoelectronic Devices Based on Organic Thin Films . . . . .	2
1.1.3 Nanophotonic Engineering . . . . .	3
1.2 Light–Matter Interaction of Organic Molecules . . . . .	8
1.3 Overview of the Thesis . . . . .	11
1.4 Bibliography . . . . .	13
<b>2 One-Dimensional Nanophotonic Engineering for Organic Optoelectronics</b>	<b>17</b>
2.1 Introduction . . . . .	17
2.2 Efficient Photon Management in Multi-junction Solar Cells . . . . .	18
2.2.1 Strategy to Overcome Thermalization Loss of Solar Cells . . . . .	18
2.2.2 Tailoring Optical Field Distribution for Current Matching . . . . .	19
2.3 Enhancement of Near-Infrared Sensitivity of Organic Solar cells . . . . .	26

2.3.1	Effects of Nanoscale Morphology of Lead Phthalocyanine Thin Films . . . . .	26
2.3.2	Absorption Coefficients of Lead Phthalocyanine Films . . . . .	28
2.3.3	Solar Cell Performances . . . . .	30
2.3.4	Analysis of the Enhanced Spectral Responsivity in the Near-Infrared Spectral Region . . . . .	32
2.3.5	Experimental Details . . . . .	37
2.4	Circularly Polarized Light Emission from Multilayer Organic Light Emitting Diodes . . . . .	39
2.4.1	Electromagnetic Description of Circularly Polarized Light Emitters . . . . .	39
2.4.2	Circularly Polarized Light Emitters in Vacuum . . . . .	41
2.4.3	Circularly Polarized Light Emitters in a Multilayer Structure . . . . .	43
2.5	Bibliography . . . . .	52
<b>3</b>	<b>Three Dimensional Nanophotonic Engineering for Organic Optoelectronics</b>	<b>57</b>
3.1	Introduction . . . . .	57
3.2	Chiral Cavity Structure for Inducing Circular Dichroic Plasmons	58
3.2.1	Limits of Chiral Molecular Optoelectronics . . . . .	58
3.2.2	Simulation Geometry . . . . .	60
3.2.3	Circular Dichroic Plasmons in the Chiral Cavity Structure	62
3.2.4	Hybridization of Surface Plasmon Polaritons . . . . .	64
3.2.5	Light–Matter Interactions in the Chiral Cavity . . . . .	68
3.3	Circular-Polarization-Sensitive Organic Photodetectors using the Chiral Cavity . . . . .	72
3.3.1	Circularly Polarized Light Detectors . . . . .	72

3.3.2	Investigation of the Dependence of Chiroptical Responses on the Position and Orientation of Absorbers . . . . .	74
3.3.3	Optimization of Circularly Polarized Light Dissymmetry Value . . . . .	79
3.4	Bibliography . . . . .	84
<b>4</b>	<b>Conclusions</b>	<b>90</b>
	<b>Appendix</b>	<b>92</b>
<b>A</b>	<b>Morphology of Lead Phthalocyanine Thin Films</b>	<b>92</b>
A.1	Analysis of Grazing Incidence Wide Angle X-ray Scattering Spectra . . . . .	92
A.2	Bibliography . . . . .	97
<b>B</b>	<b>Analysis of the Internal Quantum Efficiency of Lead Phthalocyanine– C<sub>60</sub> Heterojunction Based Solar Sells</b>	<b>99</b>
B.1	Coupled Optical and Exciton Diffusion Analyses . . . . .	99
B.2	Charge Transferred- and Charge Separated-State Energetics . .	103
B.3	Bibliography . . . . .	111
<b>요 약</b>	<b>(국문초록)</b>	<b>116</b>

# List of Figures

1.1	Schematic illustration of surface plasmon polariton (SPP) at the metallodielectric interface. SPPs are transverse magnetic wave propagating along the in-plane direction. The lines indicate the electric field ( $\mathbf{E}$ ) and the $\pm$ signs denote the polarity of the induced charges. . . . .	4
1.2	(a) Transverse magnetic dispersion relations (symbols) of a structure consisting of a dielectric ( $n = 1.8$ ) sandwiched by two flat silver films, where the upper and lower correspond to real and imaginary parts of the in-plane wavevector ( $\mathbf{k}$ ), respectively. The black solid line represents light lines in vacuum and the red line indicate the bounded SPP modes for guide to eyes. (b–d) $ E_z ^2$ , $\text{Re}(E_z)$ , and $\text{Re}(H_x)$ profiles, respectively, at $\text{Re}(\mathbf{k}) = 2\pi/\Lambda$ and energy = 1.27 eV. . . . .	5
1.3	(a) Schematic of a surface plasmon polariton (SPP) wave coupler consisting of periodically arranged square-gratings with periodicity $\Lambda$ . (b) Schematic diagram of dispersion relation of the bounded SPP wave on a metallodielectric surface with periodic gratings. . . . .	7

1.4	(a) Light emission from the mutually orthogonal electric dipole moment (ED) and magnetic dipole moment (MD) oscillating $\pi/2$ out-of-phase. (b) Light emission from the mutually parallel ED and MD oscillating in-phase. . . . .	8
1.5	Schematic of a (M)-(-)-(6) helicene molecule with anticlockwise (or left-handed) helicity. When applied by an external magnetic field, electric current is induced along the spiral structure of the molecule, which leaves a separated hole–electron pair across the molecule. . . . .	9
2.1	(a) Structure of the triple-junction hybrid solar cell. (b) Complex refractive index of the main absorber in each subcell constituting the triple-junction solar cell. . . . .	20
2.2	(a) Internal quantum efficiency of the PTB7–PC <sub>61</sub> BM heterojunction based solar cell as a function of the active layer thickness (symbols). The dashed line is a quadric fit with polynomial regression. (b) Simulated short-circuit current density as a function of the active layer thickness of each subcell. . . . .	23
2.3	(a) TiO <sub>2</sub> thickness dependency on a short-circuit current density of each subcell. (b) Current density–voltage characteristics of the a-Si/a-Si double-junction solar cell (red), the single-junction PTB7:PC <sub>61</sub> BM based organic solar cell (green), the triple-junction solar cells with out ultraviolet ozone (UVO) treatment (cyan), that with 5 sec UVO treatment (blue), and that with 15 sec UVO treatment (olive), respectively. . . . .	24
2.4	Spectrally and spatially resolved absorbed photon flux spectra of the triple-junction hybrid solar cell. . . . .	25

2.5	Two dimensional grazing incidence wide angle X-ray scattering (2D-GIWAXS) spectra of (a) n-PbPc, (b) c-PbPc, and (c) bi-PbPc films prepared on glass / ITO substrates. The color scale shown to the right of (c) applies to all spectra. Schematics of the crystalline structures of the (d) n-PbPc, (e) c-PbPc, and (f) bi-PbPc films. PbPc, ZnPc, and CuI are represented by angled purple rods, blue rods, and orange layers, respectively. . . . .	28
2.6	Absorption coefficient spectra of the three types of PbPc films.	29
2.7	Dependence of short-circuit current density on the thickness of the PbPc layer. The symbols are experimental data and the lines are fits to them. . . . .	31
2.8	Normalized optical density $ E(\lambda, z) ^2/ E_0 ^2$ of the (a) n-PbPc, (b) c-PbPc, and (c) bi-PbPc devices, where the $E$ and $E_0$ are the complex electric field in each device and the amplitude of the incident electric field, respectively, and $z$ is the distance from the glass–ITO interface. The time averaged absorbed power $\Phi$ of the (d) n-PbPc, (e) c-PbPc, and (f) bi-PbPc devices, calculated using the relation: $\Phi(\lambda, z) = \frac{1}{2}\omega\text{Im}(\epsilon) E ^2$ , where $\omega$ and $\epsilon$ are the angular frequency of the incident light and the permittivity in each layer, respectively. . . . .	33
2.9	Current density–voltage characteristics ( $J$ – $V$ ) of the n-PbPc (blue), c-PbPc (green), and bi-PbPc (red) devices under 1-sun AM 1.5G illumination. . . . .	34

2.10	(a) External quantum efficiency of the n-PbPc (blue), c-PbPc (green), and bi-PbPc (red) devices. Solid and dashed lines indicate the measured and simulated data, respectively. (b) Absorption efficiency $\eta_{\text{abs}}$ of the PbPc (solid lines) and C <sub>60</sub> (dashed lines) layers in each device. (c) Internal quantum efficiency of each device. . . . .	35
2.11	Schematic illustration of the simulation geometry of a CPL emitter in vacuum. The yellow lines denote the monitoring surface of $r = 1.5 \mu\text{m}$ . . . . .	41
2.12	(a) The dissymmetry factor and (b) the radiation power per unit area from ED $\perp$ ED. (c) The dissymmetry factor and (d) the radiation power per unit area from ED $\parallel$ MD. They are calculated at the monitoring surface of $r = 1.5 \mu\text{m}$ . . . . .	42
2.13	(a) Schematic illustration of the simulation geometry of a CP-OLED. (b) Horizontally- and (c) vertically-oriented ED $\perp$ EDs. (d) Horizontally- and (e) vertically-oriented ED $\parallel$ MDs. . . . .	44
2.14	Radiation-power-weighted averages of the dissymmetry factor in luminous intensity for the (a) horizontally-, (b) vertically-, and (c) randomly-oriented CPL emitters. . . . .	46
2.15	The dipole energy transfer efficiencies from ED $\perp$ ED (a–c) and ED $\parallel$ MD (d–f) whose orientations are denoted in top of each figure. . . . .	49

- 3.1 (a) Schematic of the simulation geometry of the chiral MDM structure investigated in this study. (b) The volume average of  $|\tilde{\mathbf{E}}|^2$  in the top electrode (top left) and the dielectric gap (top right) under  $r$ -CPL (red) and  $l$ -CPL (blue) illumination. Also shown are the associated dissymmetry factors in the top electrode (bottom left) and the dielectric gap (bottom right). . . . . 60
- 3.2 (a)  $|\tilde{E}_z|^2$  profiles at  $x = \Lambda/2$ . (b)  $|\tilde{E}_{xy}|^2$  profiles at  $x = \Lambda/2$ . (c)  $|\tilde{E}_z|^2$  profiles at  $z = -40$  nm (the midpoint on the  $z$ -axis in the dielectric layer). (d)  $|\tilde{H}_{xy}|^2$  profiles at  $z = -40$  nm. (e)  $H_x$  profiles at  $x = \Lambda/2$ . (f)  $H_x$  profiles at  $z = -40$  nm. The arrows in (e) represent the induced current density. The left and right panels in (a)–(f) correspond to the cases of  $r$ -CPL and  $l$ -CPL illumination, respectively. . . . . 63
- 3.3 Optical power absorbed in the bottom electrode as a function of the frequency  $f$  (or wavelength  $\lambda$ ) and the incident angle  $\theta$  under (a)  $r$ -CPL and (b)  $l$ -CPL illumination. The  $\mathbf{k}$  vector is in the  $yz$ -plane and  $\theta$  is the angle between  $\mathbf{k}$  and  $-\hat{\mathbf{z}}$ . The linear dependence of the resonance frequency on  $\theta$  (dashed lines) indicates that the resonance features originate from the grating-coupled SPPs. . . . . 65
- 3.4 Surface average of  $|\tilde{\mathbf{E}}|^2$  at the dielectric–bottom metal interface ( $z = -t_D$ ) as a function of the thickness of the dielectric layer  $t_D$  and the wavelength  $\lambda$  (or frequency  $f$ ) of the incident  $r$ -CPL (a) and  $l$ -CPL (b). The dotted lines in (a) are a guide to the eye, drawn to better identify the resonance conditions. . . . . 66

3.5	<p><math>E_z</math> profiles in the <math>yz</math> plane at <math>x = \Lambda/2</math> corresponding to point A (a,b), point B (c), and point C (d). The profiles in (a, c, d) are captured when <math> E_z </math> is maximized (<math>\tau = \tau_E</math>), while the profile in (b) is captured at <math>\tau = \tau_E + T/4</math>. The left and right plots in each figure correspond to the cases of <math>r</math>-CPL and <math>l</math>-CPL illumination, respectively. . . . .</p>	67
3.6	<p>(a) Difference in the dissymmetry factor between the chiral molecules in the chiral cavity and the chiral molecules in the vacuum (<math>\Delta g_{CC0}</math>). (b) Difference in the dissymmetry factor between the chiral molecules in the chiral cavity and the achiral molecules in the chiral cavity (<math>\Delta g_{CCA}</math>). (c) Line cuts of the <math>\Delta g_{CC0}</math> (blue) and <math>\Delta g_{CCA}</math> (red) spectra along <math>f = 454</math> THz, respectively. . . . .</p>	69
3.7	<p>(a) Difference in the optical chirality (<math>\Delta C = C^l - C^r</math>) at <math>z = -t_D/2</math>. (b) Difference in the square of the electric field intensity (<math>\Delta  \mathbf{E} ^2 =  \mathbf{E}^l ^2 -  \mathbf{E}^r ^2</math>) at <math>z = -t_D/2</math>. . . . .</p>	70
3.8	<p>Dissymmetry factor of absorption by molecules in the chiral cavity with different molecular orientation and chirality. The black, orange, and green solid lines correspond to randomly-, vertically-, and horizontally-oriented anisotropic molecules, respectively. The blue and red dashed lines correspond to the isotropic chiral molecules with <math>g_0 = 1.23</math> and those with <math>g_0 = -1.23</math>, respectively. . . . .</p>	71

3.9	(a) Layer structure of the plasmonic CP-OPD. The absorption efficiencies of the CP-OPD with $t_A = 5 \text{ nm}$ and $\alpha = 1 \times 10^5 \text{ cm}^{-1}$ as a function of $d$ and the orientation of $\mathbf{p}$ under $r$ -CPL (b) and $l$ -CPL (c) illumination. (d) The dissymmetry factor of absorption calculated from (b,c). . . . .	75
3.10	The absorption efficiencies for case $p_\perp$ as a function of $\alpha$ and $t_A$ under $r$ -CPL (a) and $l$ -CPL (b) illumination. (c) The dissymmetry factor calculated from (e,f). The value of $t_A$ (in nm) is shown for each line. . . . .	78
3.11	Volume integral of $ \tilde{E}_z(\lambda, \alpha) ^2$ in the absorption layer with $t_A = 20 \text{ nm}$ under $r$ -CPL (a) and $l$ -CPL (b) illumination, calculated with $\alpha$ varying from $1 \times 10^4$ to $2 \times 10^5 \text{ cm}^{-1}$ in $1 \times 10^4 \text{ cm}^{-1}$ increments. (c) The volume integral of $ \tilde{E}_z(\lambda, \alpha) ^2$ in the absorption layer (blue), the imaginary part of the $z$ -component of the relative permittivity ( $\text{Im}(\tilde{\epsilon}_z)$ , orange) of the absorption layer, and their product (red), which is proportional to $\eta_A$ , under $r$ -CPL (c) and $l$ -CPL (d) illumination with $\lambda = 660 \text{ nm}$ . In the case of $r$ -CPL, the tradeoff between the volume integral of $ \tilde{E}_z ^2$ and $\text{Im}(\tilde{\epsilon}_z)$ is clearly shown, resulting in a maximum of $\eta_A$ at $\alpha = 6 \times 10^4 \text{ cm}^{-1}$ . In the case of $l$ -CPL, on the other hand, $\eta_A$ increases monotonically with $\alpha$ because the $ \tilde{E}_z(\lambda) ^2$ integral decreases much more slowly compared to the $r$ -CPL case. . . .	80

3.12	Absorption efficiencies of the CP-OPD with $t_A = 20$ nm and $\alpha = 1 \times 10^4$ cm <sup>-1</sup> under $r$ -CPL (a) and $l$ -CPL (b) illumination, calculated with $\text{Im}(\tilde{\epsilon}_r)$ of the top and bottom electrodes varying from 0 to 0.38 in 0.038 increments. The data denoted by red dashed lines correspond to the $\text{Im}(\tilde{\epsilon}_r)$ value of a silver film (= 0.19) taken from the literature [22]. (c) Dissymmetry factor of absorption at $\lambda = 660$ nm (gray triangles) calculated from (a,b) and absorption efficiencies at $\lambda = 660$ nm under $r$ -CPL (filled squares) and $l$ -CPL (open squares) illumination. . . . .	81
A.1	2D-GIWAXS spectra of the (a) n-PbPc, (b) c-PbPc, and (c) bi-PbPc films prepared on glass / ITO substrates, and those of the (d) n-PbPc, (e) c-PbPc, and (f) bi-PbPc films on Si substrates, in the $q_{xy}$ - $q_z$ plane with $q < 2 \text{ \AA}^{-1}$ . . . . .	93
A.2	(a) Absorption coefficient $\alpha$ spectra of the three types of PbPc films. Line cuts (b) along the arc defined by $q = 0.54 \text{ \AA}^{-1}$ , and (c) along the directions of $\chi \simeq 60^\circ$ of the GIWAXS spectra of the c-PbPc (green) and bi-PbPc (red) films. The dashed lines in (b,c) are the Gaussian fits to the line cuts. The fit for the bi-PbPc in (b) can be decomposed into the two dotted lines that represent Bragg peaks in Regions 1 and 2. . . . .	95
A.3	(a) A GIWAXS spectrum and (b) a schematic of the crystalline structure of a 6-nm-thick ZnPc layer. (c) A GIWAXS spectrum and (d) a schematic of the crystalline structure of a 20-nm-thick ZnPc layer. In both cases, the ZnPc films were deposited on a 1-nm-thick CuI layer deposited on a glass substrate pre-coated with an ITO layer. . . . .	96

B.1	Calculated (a) exciton diffusion efficiency $\eta_{ed}$ and (b) CT-dissociation efficiency $\eta_{cs}$ of the n-PbPc (blue), c-PbPc (green), and bi-PbPc (red) devices. Solid, dotted, and dashed lines are the data calculated with the non-quenching ( $k_q = 0$ ), perfect-quenching ( $k_q = \infty$ ), and partial-quenching ( $k_q$ [s <sup>-1</sup> ] shown near each dashed line) boundary conditions, respectively. Note that the solid (and dotted) lines in (a) are very closely located. . . . .	102
B.2	Temperature-dependence of open-circuit voltages $V_{oc}$ of the (a) n-PbPc, (b) c-PbPc, and (c) bi-PbPc devices. Symbols and dashed lines indicate the measured data and the fits, respectively. The extracted parameters (average energy of charge-transfer (CT) states $E_{ct}$ , standard deviation of CT state energy distribution $\sigma_{ct}$ , and a variable proportional to the recombination current of CT excitons $J_{s0}$ ) are listed inside the figures. . . . .	105
B.3	(a) Origins of open-circuit voltage $V_{oc}$ loss. (b) Enthalpy $H$ and (c) free energy $G$ of an electron-hole pair as functions of their separation $r$ . Open circles in (b) and (c) denote the enthalpy $H_{cs}$ and the free energy $G_{cs}$ of the CS state, respectively, while filled circles in (b) and (c) denote the enthalpy $H_{ct}$ and the free energy $G_{ct}$ of the CT state, respectively. . . . .	106

# List of Tables

2.1	Solar cell parameters (short-circuit current density $J_{sc}$ , open-circuit voltage $V_{oc}$ , fill factor FF, and power-conversion efficiency PCE) extracted from the current density–voltage characteristics measured under 1-sun AM 1.5G illumination. Also listed in the table are the optical band gaps $E_{opt}$ of the PbPc films and a ZnPc film. Averages of the solar cell parameters were taken across 6–8 devices. . . . .	32
3.1	Dissymmetry factor of photocurrent ( $g_{Ph}$ ) and external quantum efficiency ( $\eta_E$ ) of previously demonstrated circular-polarization-sensitive photodetectors compared with those of my photodetector. . . . .	83



# Chapter 1

## Introduction

### 1.1 Nanophotonic Engineering for Organic Optoelectronics

#### 1.1.1 Organic Molecules

Organic molecules have attracted much attention as a photoactive material due to their unique optical characteristics. A number of organic molecules, featuring a very high absorption coefficient, can absorb light very efficiently even in a nanoscale thin film, desirable for low-cost solar energy harvesting [1]. A near-unity luminescence quantum yield is another feature that organic molecules often attain, enabling highly efficient display and lighting devices based on organic molecular emitters [2]. Moreover, their controllable polarizability allows their optical characteristics to be fully explored as applied into organic optoelectronics [3, 4, 5]. In this thesis, I thus deal with the organic molecules, desired to the photoactive layer of optoelectronic devices.

### 1.1.2 Optoelectronic Devices Based on Organic Thin Films

Owing to the unique optical properties of organic molecules, optoelectronic devices based on organic molecular thin films have attained significant progress in information technology. Organic light emitting diodes (OLEDs) have been commercially successful as display devices, and organic solar cells (OSCs) have come close to 15 % of power conversion efficiency (PCE) being a requirement expected to be commercialize [6, 7, 8]. Together with the superior quantum efficiency, their functionalities, such as flexibility, transparency, and low-cost engineering make organic electronics more promising than inorganic counterparts as building blocks for next-generation information technology. These functionalities arise from the properties of organic media bonded together with weak Van der Waals force. Such thin film property eliminates the lattice-matching requirement, thus enabling a number of superior heterojunctions composed of organic molecules. This is in contrast to the inorganic counterparts, formed by stronger ionic or covalent bonds, which are stiff and require the lattice matching for epitaxial growth of thin films. The morphological and energetic disorder inherent in organic thin films gives rise to unique charge transfer characteristics at organic–metal and organic–organic interfaces [9, 10, 11], considered as a key of the device operation. At the same time, however, the intrinsic disorder also causes high thermalization loss of OSCs [12, 13], broad emission spectra of OLEDs [2], and low electrical conductivity. In addition, the weak bonding force results in those organic media being less susceptible to damage from moisture and oxygen. Thus, organic optoelectronics based on organic thin films have often come to the limit, as technological advances have more requirements for materials.

### 1.1.3 Nanophotonic Engineering

Nanophotonic engineering is a promising way to improve the optical properties of organic molecules or to induce new functionalities. The optical behavior of molecules, e.g., optical absorption, emission, and their polarization sensitivity, are influenced by the local photonic density of states ( $\rho_P$ ) as well as their inherent properties in vacuum (this will be mathematically discussed in more detail in the Section 1.2). Since the total thickness of multilayer organic optoelectronic devices, such as OSCs and OLEDs, is typically smaller than the operation wavelength in the visible spectral range, their structure should be treated with coherent behavior: the internal interference should be taken into account. In addition, the metal-to-photoactive layer separation may be within the range in which Förster-like energy transfer takes place between them. Therefore, the multilayer OSCs and OLEDs should be considered as a kind of one-dimensional nanophotonic structure. When a plane wave impinges a conventional organic optoelectronic devices, the presence of an optically thick metal layer that serves as a cathode in general gives rise to specularly reflected EM wave, which in turn interfere with the incident EM wave, forming a standing wave. Since the degree of spatial overlap between the photoactive layer and the high field region of the standing wave is crucial to the performance of OLEDs and OSCs, one should optimize the thicknesses of the constituting layers to maximize it [14, 15]. For the top metal, the use of a thin metal layer as the top electrode that serves as the anode in general compared to the typically used a transparent conductive oxide (TCO) is a way to make nanocavity structure, which significantly increase the field intensity in the position of a photoactive layer. OLEDs based on the nanocavity structure enable a highly directional light emission with a high out-coupling efficiency, determined by the ratio of the number of photons emitted into air and the

number of generated photons in the device [16, 17].

Plasmonics has opened the door to innovations in transferring information and energy in the form of confined electromagnetic fields in a much smaller space than the operation wavelength. Controlling the geometry of three dimensional plasmonic structures to induce the desired functionality is generally easier than chemical designing of a molecule, which makes them promising platforms. A metal–dielectric bilayer support a EM mode, called surface plas-

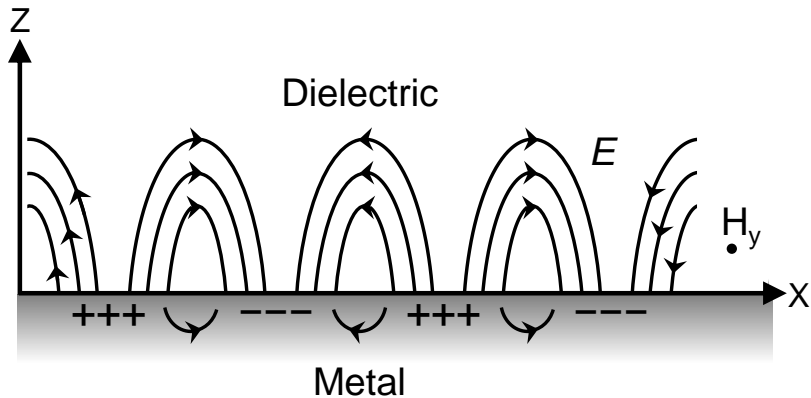


Figure 1.1 Schematic illustration of surface plasmon polariton (SPP) at the metal-dielectric interface. SPPs are transverse magnetic wave propagating along the in-plane direction. The lines indicate the electric field ( $\mathbf{E}$ ) and the  $\pm$  signs denote the polarity of the induced charges.

mon polariton (SPP) featuring a highly confined EM field intensity at the interface (Fig. 1.1). Due to the very high photonic density of states, SPP can be a nanophotonic route for increasing the optical absorption and photon emission rates of molecules placed near the interface [18].

A nanocavity structure consisting of a subwavelength-thick-dielectric interposed by two metal layers (MDM) allows more confined EM waves with higher field intensity than the metal–dielectric bilayer (Fig. 1.2) [19]. Figure 1.2 shows a MDM structure and the bounded SPP modes (the red lines

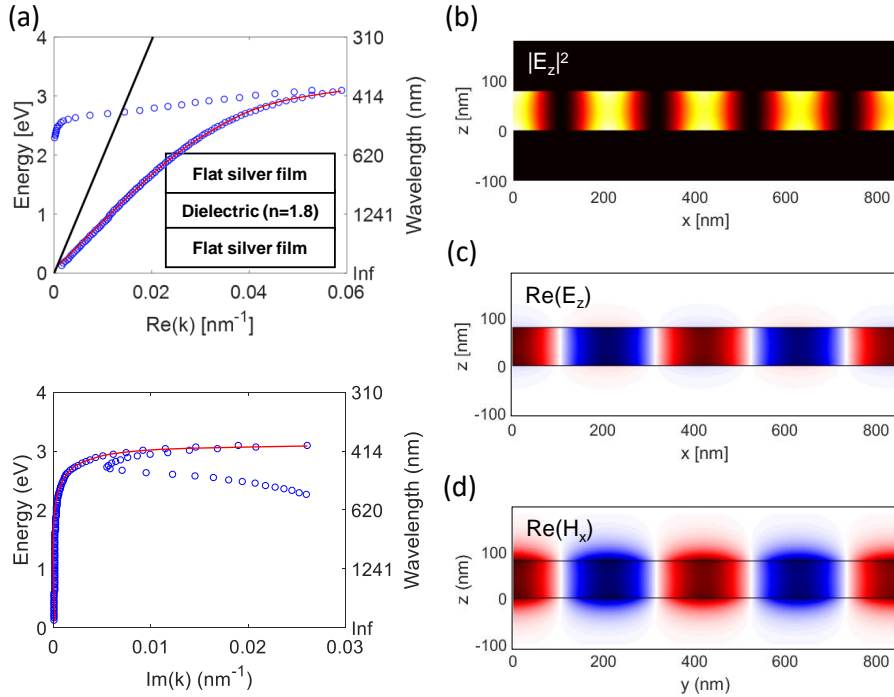


Figure 1.2 (a) Transverse magnetic dispersion relations (symbols) of a structure consisting of a dielectric ( $n = 1.8$ ) sandwiched by two flat silver films, where the upper and lower correspond to real and imaginary parts of the in-plane wavevector ( $\mathbf{k}$ ), respectively. The black solid line represents light lines in vacuum and the red line indicate the bounded SPP modes for guide to eyes. (b–d)  $|E_z|^2$ ,  $\text{Re}(E_z)$ , and  $\text{Re}(H_x)$  profiles, respectively, at  $\text{Re}(\mathbf{k}) = 2\pi/\Lambda$  and  $\text{Energy} = 1.27$  eV.

for guide to eyes), featuring a high EM field intensity in the dielectric gap. These SPPs in the dielectric gap originate from the hybridization between two SSP waves at the top metal–dielectric interface and at the bottom metal–dielectric interface [19]. Because the in-plane wavevector ( $\mathbf{k}$ ) of the SPP waves are larger than  $\mathbf{k}$  of a planewave propagating in air (black line; air mode) at the same photon energy, SPP waves cannot be coupled into the air mode in general [Fig. 1.2(a)]. In order to enable SPPs to be out-coupled into the air, a widely employed nanophotonic platform is a periodically arranged nanopattern (Fig. 1.3). When a nanograting with a period ( $\Lambda$ ) is engraved on the metallodielectric interface, thus scattering SPP waves propagating along the interface (or scattering the incident planewaves), their  $\mathbf{k}$  vector loses (or adds) momentum by a factor of  $2\pi n/\Lambda$ , where  $n$  is an integer.

Three-dimensional metal nanostructures support more various plasmonic modes, enabling more advanced nanophotonic applications. When a plasmonic nanostructure is engineered to allow excitation of electric dipolar and magnetic dipolar modes oscillating at a same frequency, anomalous optical characteristics can be obtained depending on the mutual phase difference and the relative dipole orientation. In Fig. 1.4, if an oscillating electric dipole moment ( $\mathbf{p}$ ) aligned with  $y$ -axis and an oscillating magnetic dipole moment ( $\mathbf{m}$ ) aligned with  $x$ -axis oscillate in  $\pi/2$  out-of-phase, they radiate EM waves unidirectionally: two EM waves emitted by the dipoles in  $-z$  direction are constructively interfered while they are destructively interfered in the opposite direction. Figure 1.4(b) shows  $\mathbf{p}$  and  $\mathbf{m}$  polarized along to  $y$ -axis, which emit circularly polarized light into  $\pm z$  direction when oscillating in-phase. Note that the radiation power of the single  $\mathbf{p}$  is scaled to be identical to that of the single  $\mathbf{m}$ . Additional examples are available elsewhere, e.g., a perfect absorber with an absorption efficiency close to 100% [20], a holography that has a different

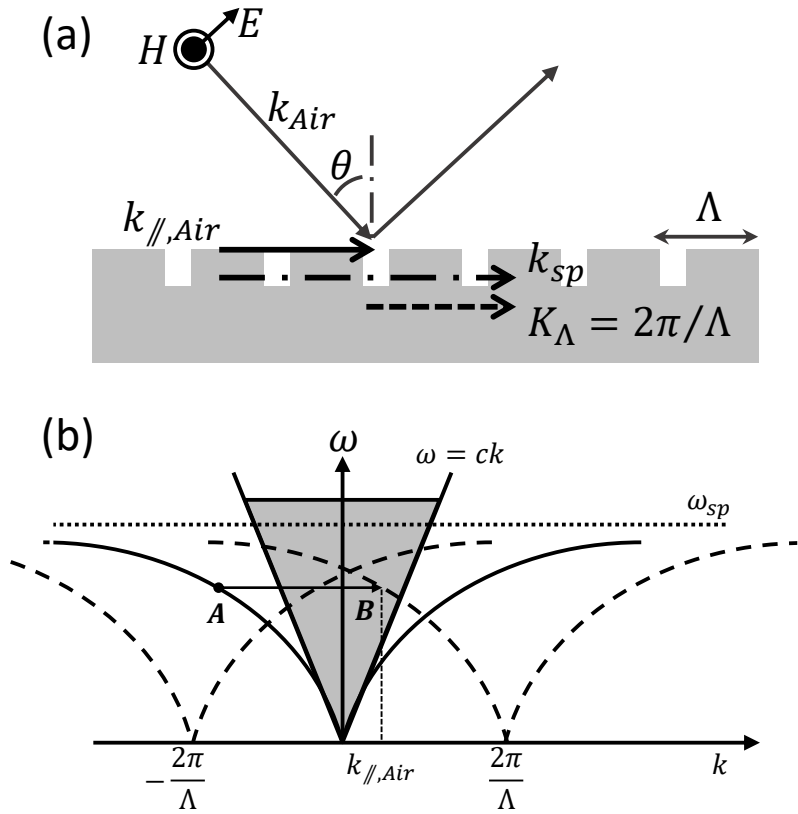


Figure 1.3 (a) Schematic of a surface plasmon polariton (SPP) wave coupler consisting of periodically arranged square-gratings with periodicity  $\Lambda$ . (b) Schematic diagram of dispersion relation of the bounded SPP wave on a metallodielectric surface with periodic gratings.

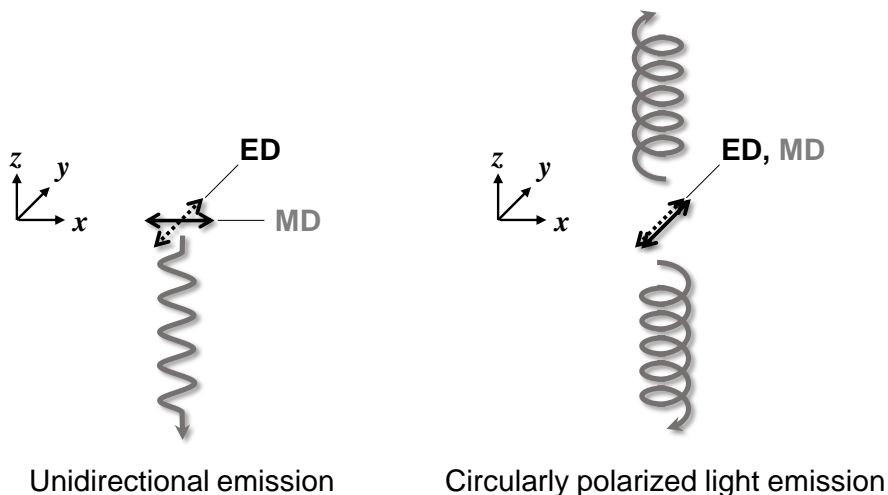
(a)  $ED \perp MD$ ,  $90^\circ$  out-of-phase(b)  $ED // MD$ , in-phase

Figure 1.4 (a) Light emission from the mutually orthogonal electric dipole moment (ED) and magnetic dipole moment (MD) oscillating  $\pi/2$  out-of-phase. (b) Light emission from the mutually parallel ED and MD oscillating in-phase.

reflection pattern depending on the polarization state of the incidence EM wave [21], and nanorobots that can control the mechanical walk of nanostructures depending on the polarization state [22].

## 1.2 Light–Matter Interaction of Organic Molecules

In this section, I discuss mathematically in detail how the EM environment in which a molecule is located affects its light absorption or emission characteristics. In most textbooks of electromagnetics, electric dipole moments ( $\tilde{\mathbf{p}}$ ) are introduced proportional to the electric field ( $\tilde{\mathbf{E}}$ ) in a linear system, where the proportional constant is the electrical polarizability ( $\tilde{\alpha}$ ). Here, a parameter with the tilde sign is a complex quantity. This implicitly ignores the dependence of  $\tilde{\mathbf{p}}$  on magnetic fields ( $\tilde{\mathbf{B}}$ ), which in most cases is true. Depending on the shape of organic molecule, the presence of  $\tilde{\mathbf{B}}$  can lead to  $\tilde{\mathbf{p}}$ , and helicene

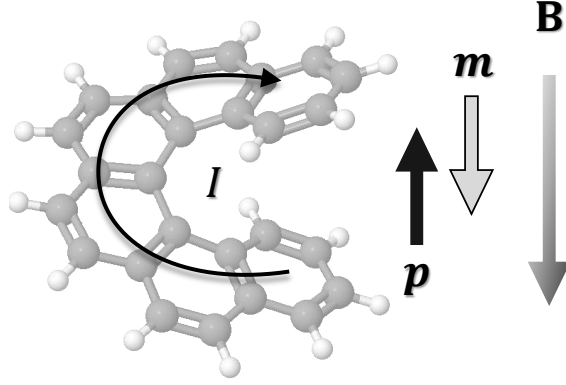


Figure 1.5 Schematic of a (M)-(6) helicene molecule with anticlockwise (or left-handed) helicity. When applied by an external magnetic field, electric current is induced along the spiral structure of the molecule, which leaves a separated hole–electron pair across the molecule.

is a representative example of this phenomenon (Fig. 1.5). When a magnetic field is applied to a helicene molecule, the induced current leaves a separated charge on both ends of it, generating  $\tilde{\mathbf{p}}$ . Thus,  $\tilde{\mathbf{p}}$  can be generally expressed as [23]:

$$\tilde{\mathbf{p}} = \tilde{\alpha}\tilde{\mathbf{E}} - i\tilde{\mathbf{G}}\tilde{\mathbf{B}}, \quad (1.1)$$

where  $\tilde{\alpha}$  and the electro-magnetic dipole polarizability ( $\tilde{\mathbf{G}}$ ) are a third-order tensor. The presence of  $\tilde{\mathbf{G}}$  also allows electric field to induce magnetic dipole moment ( $\tilde{\mathbf{m}}$ ), which is expressed as:

$$\tilde{\mathbf{m}} = \tilde{\chi}\tilde{\mathbf{B}} + i\tilde{\mathbf{G}}\tilde{\mathbf{E}}, \quad (1.2)$$

where,  $\tilde{\chi}$  is the magnetic susceptibility. The optical absorption efficiency  $\eta_A$  can be described by [18]:

$$\eta_A = \langle \tilde{\mathbf{p}} \cdot \mathbf{E} + \tilde{\mathbf{m}} \cdot \mathbf{B} \rangle, \quad (1.3)$$

where this equation is assumed to be normalized by the incident power. In a homogeneous medium, EM fields are described by using the following equations:

$$\tilde{\mathbf{E}}(t) = \tilde{\mathbf{E}}_0 \exp(-i\omega t) = \begin{pmatrix} \tilde{E}_x \\ \tilde{E}_y \\ \tilde{E}_z \end{pmatrix} \exp(-i\omega t), \quad (1.4)$$

and

$$\tilde{\mathbf{B}}(t) = \tilde{\mathbf{B}}_0 \exp(-i\omega t) = \begin{pmatrix} \tilde{B}_x \\ \tilde{B}_y \\ \tilde{B}_z \end{pmatrix} \exp(-i\omega t), \quad (1.5)$$

and then substituting Eqs. (1.4) and (1.5) into Eq. (1.3) results in:

$$\eta_A = \frac{\omega}{2} [\text{Im}(\tilde{\alpha}) |\tilde{\mathbf{E}}|^2 + \text{Im}(\tilde{\chi}) |\tilde{\mathbf{B}}|^2] + \omega \text{Im}(\tilde{\mathbf{G}}) \text{Im}(\tilde{\mathbf{E}}^* \cdot \tilde{\mathbf{B}}) \quad (1.6)$$

Since most organic media are non-magnetic, the term with  $\text{Im}(\chi)$  can be ignored in general. Using the time-even pseudoscalar  $C$  [23]:

$$C = \omega \mu_0 2c^2 \text{Im}(\tilde{\mathbf{E}}^* \cdot \tilde{\mathbf{B}}), \quad (1.7)$$

$\eta_A$  can be simplified as:

$$\eta_A = \frac{\omega}{2} \text{Im}(\tilde{\alpha}) |\tilde{\mathbf{E}}|^2 + \frac{2G''C}{\varepsilon_0}, \quad (1.8)$$

where  $\varepsilon_0$  and  $\mu_0$  are the permittivity and permeability in vacuum, respectively. According to Tang *et al.*,  $C$  represents the optical chirality of the EM field. If there is no  $C$ , Eq. (1.8) can be expressed as:

$$\eta_A = \frac{\omega}{2} \text{Im}(\tilde{\alpha}) |\tilde{\mathbf{E}}|^2 = \frac{\omega}{2} [\text{Im}(\tilde{\alpha}_x) |\tilde{E}_x|^2 + \text{Im}(\tilde{\alpha}_y) |\tilde{E}_y|^2 + \text{Im}(\tilde{\alpha}_z) |\tilde{E}_z|^2], \quad (1.9)$$

where  $\tilde{\alpha}_i$  is the diagonal  $i$  component of a tensor  $\tilde{\boldsymbol{\alpha}}$ .

According to Fermi's golden rule [24], transition from one eigenstate to another eigenstate is the result of a weak perturbation by the vacuum field and its rate is governed by the degree of overlapped wavefunctions between the initial and final states and by the the local photonic density of states ( $\rho_P$ ) of the final quantum states. Thus, the light emission rate ( $\gamma_E$ ) of the molecule in the case of nonmagnetic can be described by the following equation [18]:

$$\gamma_E = \frac{4\pi\omega}{3h} |\mathbf{p}|^2 \rho_P, \quad (1.10)$$

where  $h$  is the Planck constant. To express light emission from molecules with various wavevector components,  $\rho_P$  can be determined using the dyadic Green's function ( $\vec{\mathbf{G}}$ ) of the system [18]:

$$\rho_P = \frac{6\omega}{\pi c^2} [\hat{\mathbf{p}} \cdot \text{Im}(\vec{\mathbf{G}}) \cdot \hat{\mathbf{p}}] \quad (1.11)$$

where  $\hat{\mathbf{p}}$  is a unit vector pointing in the identical direction of  $\mathbf{p}$ . Through the semiclassical representations of Fermi's golden rule, the degree of overlap between the two eigenstates and can be expressed as the degree of alignment between  $\mathbf{E}$  and  $\mathbf{p}$  (i.e.,  $\mathbf{p} \cdot \mathbf{E}/|\mathbf{p} \cdot \mathbf{E}|$ ) and the  $\rho_P$  is approximately represented by the square of the electric field intensity.

The results in this section point out that the increase of  $|\mathbf{E}|^2$  (or  $\rho_P$ ) is a key to improve the optical absorption and emission properties of molecules via nanophotonic engineering.

### 1.3 Overview of the Thesis

In this thesis, I investigate the interaction between molecules and their EM fields, and explore ways in which these interactions can positively affect the

performance of organic optoelectronic devices. In Chapter 2, one dimensional nanophotonic engineering will be demonstrated to solve the urgent problems in organic solar cell community, i.e., low light absorption in the near-infrared region and the severe thermalization loss, I will propose two types of solar cell structures and show how to design them considering optical interference. In addition, I will discuss the nanophotonic strategy to overcome the limits of circularly polarized light emitting organic diodes (CP-OLED) via numerical simulation. This is the first comprehensive study to guide the design of a CP-OLED structure in terms of the CPL dissymmetry factor and the external quantum efficiency. In Chapter 3, it will be introduced that a chirally patterned metal–dielectric–metal (chiral MDM) structure can selectively excite plasmonic hotspots depending on helicity of incident circularly polarized waves. It will be interpreted in the framework of hybridization between two surface plasmon polaritons arising bounded at each metallodielectric layer. In addition, the chiral nanocavity will be applied to organic photodetectors, which is a new type of optoelectronic devices attaining both high quantum efficiency and circular dichroism. In Chapter 4, I will summarize this work and discuss its prospects.

## 1.4 Bibliography

- [1] H. Kim, H. G. Park, M. J. Maeng, Y. R. Kang, K. R. Park, J. Choi, Y. Park, Y. D. Kim, and C. Kim, “Multifunctional bilayer template for near-infrared-sensitive organic solar cells,” *ACS Appl. Mater. Interfaces*, pp. 16681–16689, 2018.
- [2] K. Udagawa, H. Sasabe, F. Igarashi, and J. Kido, “Simultaneous realization of high  $\eta_{\text{eq}}$  of 30 %, low drive voltage, and low efficiency roll-off at high brightness in blue phosphorescent OLEDs,” *Adv. Opt. Mater.*, vol. 4, no. 1, pp. 86–90, 2016.
- [3] D. Yokoyama, “Molecular orientation in small-molecule organic light-emitting diodes,” *J. Mater. Chem.*, vol. 21, no. 48, pp. 19187–19202, 2011.
- [4] K. Vasseur, B. P. Rand, D. Cheyns, L. Froyen, and P. Heremans, “Structural evolution of evaporated lead phthalocyanine thin films for near-infrared sensitive solar cells,” *Chem. Mater.*, vol. 23, no. 3, pp. 886–895, 2011.
- [5] C. Schünemann, D. Wynands, K.-J. Eichhorn, M. Stamm, K. Leo, and M. Riede, “Evaluation and control of the orientation of small molecules for strongly absorbing organic thin films,” *J. Phys. Chem. C*, vol. 117, no. 22, pp. 11600–11609, 2013.
- [6] J. Zhao, Y. Li, G. Yang, K. Jiang, H. Lin, H. Ade, W. Ma, and H. Yan, “Efficient organic solar cells processed from hydrocarbon solvents,” *Nat. Energy*, vol. 1, no. 2, a. 15027, 2016.
- [7] V. Vohra, K. Kawashima, T. Kakara, T. Koganezawa, I. Osaka, K. Takimiya, and H. Murata, “Efficient inverted polymer solar cells em-

- ploying favourable molecular orientation,” *Nat. Photonics*, vol. 9, no. 6, pp. 403–408, 2015.
- [8] Y. Liu, J. Zhao, Z. Li, C. Mu, W. Ma, H. Hu, K. Jiang, H. Lin, H. Ade, and H. Yan, “Aggregation and morphology control enables multiple cases of high-efficiency polymer solar cells,” *Nat. Commun.*, vol. 5, a. 5293, 2014.
- [9] M. A. Baldo and S. R. Forrest, “Interface-limited injection in amorphous organic semiconductors,” *Phys. Rev. B*, vol. 64, no. 8, a. 085201, 2001.
- [10] B. N. Limketkai and M. A. Baldo, “Charge injection into cathode-doped amorphous organic semiconductors,” *Phys. Rev. B*, vol. 71, no. 8, a. 085207, 2005.
- [11] T. M. Burke, S. Sweetnam, K. Vandewal, and M. D. McGehee, “Beyond langevin recombination: how equilibrium between free carriers and charge transfer states determines the open-circuit voltage of organic solar cells,” *Adv. Energy Mater.*, vol. 5, no. 11, a. 1500123, 2015.
- [12] K. Vandewal, K. Tvingstedt, A. Gadisa, O. Inganäs, and J. V. Manca, “Relating the open-circuit voltage to interface molecular properties of donor:acceptor bulk heterojunction solar cells,” *Phys. Rev. B*, vol. 81, no. 12, a. 125204, 2010.
- [13] K. Vandewal, K. Tvingstedt, A. Gadisa, O. Inganas, and J. V. Manca, “On the origin of the open-circuit voltage of polymer-fullerene solar cells,” *Nat. Mater.*, vol. 8, no. 11, pp. 904–909, 2009.
- [14] R. Meerheim, M. Furno, S. Hofmann, B. Lussem, and K. Leo, “Quantification of energy loss mechanisms in organic light-emitting diodes,” *Appl. Phys. Lett.*, vol. 97, no. 25, a. 253305, 2010.

- [15] P. Peumans, A. Yakimov, and S. R. Forrest, “Small molecular weight organic thin-film photodetectors and solar cells,” *J. Appl. Phys.*, vol. 93, no. 7, pp. 3693–3723, 2003.
- [16] Q. Wang, Z. Deng, and D. Ma, “Realization of high efficiency microcavity top-emitting organic light-emitting diodes with highly saturated colors and negligible angular dependence,” *Appl. Phys. Lett.*, vol. 94, no. 23, a. 233306, 2009.
- [17] M. Agrawal, Y. Sun, S. R. Forrest, and P. Peumans, “Enhanced outcoupling from organic light-emitting diodes using aperiodic dielectric mirrors,” *Appl. Phys. Lett.*, vol. 90, no. 24, a. 241112, 2007.
- [18] anger, P. Bharadwaj, and L. Novotny, “Enhancement and quenching of single-molecule fluorescence,” *Phys. Rev. Lett.*, vol. 96, no. 11, a. 113002, 2006.
- [19] J. A. Dionne, L. A. Sweatlock, H. A. Atwater, and A. Polman, “Plasmon slot waveguides: Towards chip-scale propagation with subwavelength-scale localization,” *Phys. Rev. B*, vol. 73, no. 3, a. 035407, 2006.
- [20] J. Hao, L. Zhou, and M. Qiu, “Nearly total absorption of light and heat generation by plasmonic metamaterials,” *Phys. Rev. B*, vol. 83, no. 16, a. 165107, 2011.
- [21] W. M. Ye, F. Zeuner, X. Li, B. Reineke, S. He, C.-W. Qiu, J. Liu, Y. Wang, S. Zhang, and T. Zentgraf, “Spin and wavelength multiplexed nonlinear metasurface holography,” *Nat. Commun.*, vol. 7, a. 11930, 2016.
- [22] M. J. Urban, C. Zhou, X. Duan, and N. Liu, “Optically resolving the dynamic walking of a plasmonic walker couple,” *Nano Lett.*, vol. 15, no. 12, pp. 8392–8396, 2015.

- [23] Y. Tang and A. E. Cohen, “Optical chirality and its interaction with matter,” *Phys. Rev. Lett.*, vol. 104, no. 16, a. 163901, 2010.
- [24] D. J. Griffiths, *Introduction to Quantum Mechanics*. Pearson international edition (Pearson Prentice Hall, 2005), 2010.

## Chapter 2

# One-Dimensional Nanophotonic Engineering for Organic Optoelectronics

### 2.1 Introduction

In this chapter, I address the importance of nanophotonic engineering of one dimensional multilayer optoelectronics to rationally design the architecture, thus fully utilizing their potentials. First, I perform an nanophotonic simulation to design organic-inorganic triple-junction hybrid solar cells, which is a promising architecture to reduce thermalization loss of solar cells but is known to be highly challenging for experimental optimization. Next, the importance of complementary control of molecular orientation together with nanophotonic property is addressed to fully optimize the spectral sensitivity of organic solar cells (OSC) in the near-infrared (NIR) spectral region, where a structural templating method is used to control molecular orientation. Finally, a numerical simulation of CP-OLEDs is demonstrated, which is the first work comprehen-

sively understanding their optical characteristics in terms of  $g_L$  and the energy loss distribution of light from the CPL emitter. To investigate the nanophotonic characteristics of OSCs and OLEDs, the transfer matrix and the finite element based simulations are employed, respectively.

## 2.2 Efficient Photon Management in Multi-junction Solar Cells

### 2.2.1 Strategy to Overcome Thermalization Loss of Solar Cells

Solar cells based on organic semiconductors have advantageous of cheap, light-weight, flexible, and large-area processes, but their thermalization loss—loss of photon energy greater than bandgap by the difference between them—is usually exceeding 0.3 eV as compared to the inorganic counterpart. Employing multi-junction architecture, consisting of two or more subcells with complementary optical bandgap ( $E_{\text{opt}}$ ), is a way for efficient photon management, thus minimizing the thermalization loss. The largest portion of the energy output is occupied by the large- $E_{\text{opt}}$  subcell that absorb high energy photons, which is usually employed as the front cell being illuminated first. A hybrid multi-junction solar cell consisting of a subcell using hydrogenated amorphous silicon (a-Si) with large- $E_{\text{opt}}$  and an organic semiconductor based subcell with small  $E_{\text{opt}}$  can effectively reduce the thermalization loss while accepting the advantages of the organic solar cell described above. It is important for multi-junction solar cells to design the device architecture so that the identical current is generated from the top and bottom subcells. If the currents do not match in the two subcells, charges build up somewhere, leading to the reduction of power conversion efficiency (PCE). In the case of a-Si / organic hybrid double junction solar cells, organic semiconductor-based subcells limit current matching in general. The thickness of the a-Si layer needs to be less than the

thickness of the optimized single-junction device based on it, thereby reducing the absorption of a-Si and increasing absorption in the organic layer in the wavelength region where the two subcells are spectrally overlapped.

Here, it is demonstrated that triple junction solar cell consisting of a-Si (top) / a-Si (middle) / organic (bottom) layers is desirable to PCE compared to the a-Si (top) / organic (bottom) double-junction solar cell, despite the absorption-spectral overlap between the top and middle a-Si subcells. The main idea of this study is to minimize the absorption loss for current matching by translating the parasitically absorbed photons into a form that can contribute to device performance in terms of open-circuit voltage ( $V_{oc}$ ). In order to create the same current in three subcells, I optimized the thickness of each subcell and charge transport layer through transfer matrix based modeling. In order to generate the identical current density in three subcells, I optimized the thickness of each subcell and that of charge transport layer using the transfer matrix based optical modeling. Based on the results of the optical modeling, the triple-junction hybrid solar cell can be rationally designed, thus exhibiting a high PCE of 7.8 % and  $V_{oc}$  of 2.35 V, being the sum of the  $V_{oc}$  of each subcell.

### 2.2.2 Tailoring Optical Field Distribution for Current Matching

The architecture of triple-junction solar cell is comprised of two a-Si based solar cells (top and middle subcells, respectively) and a PTB7-PC<sub>61</sub>BM donor-acceptor mixed heterojunction based solar cell. The detailed structure is as follows [Fig. 2.1(a)]: glass / 230 nm indium tin oxide (ITO) / 8 nm p-doped a-Si /  $h_{a-Si1}$  nm a-Si / 10 nm n-doped a-Si / 7 nm p-doped a-Si /  $h_{a-Si2}$  nm a-Si / 25 nm n-doped a-Si / 20 nm ITO / 23 nm PEDOT:PSS /  $h_{OPV}$  nm

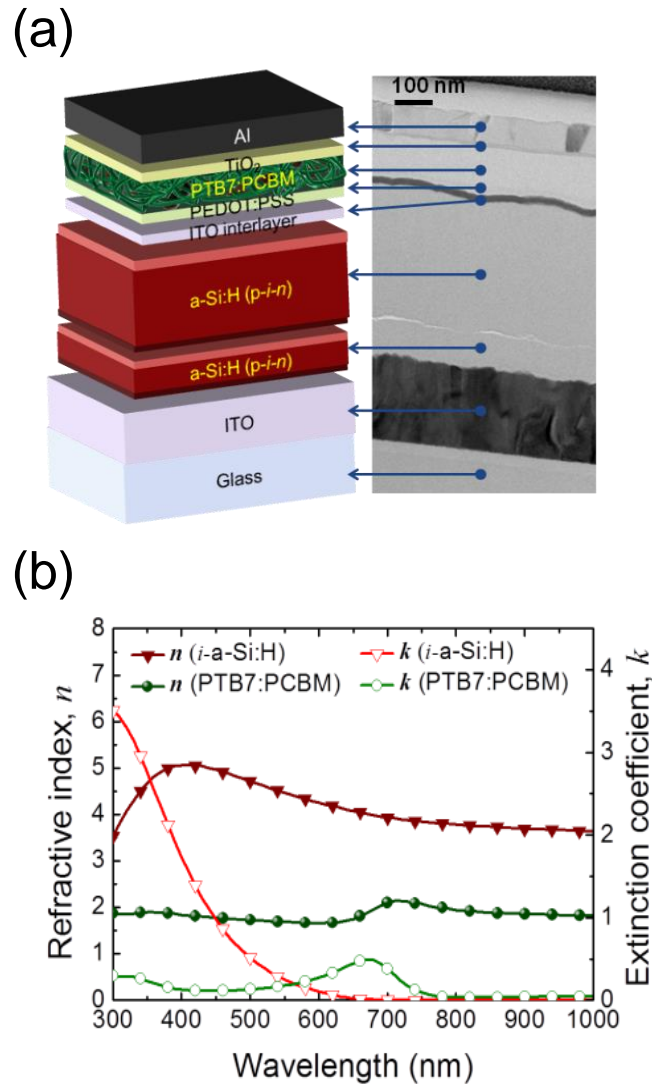


Figure 2.1 (a) Structure of the triple-junction hybrid solar cell. (b) Complex refractive index of the main absorber in each subcell constituting the triple-junction solar cell.

PTB7:PC<sub>61</sub>BM /  $h_{\text{TiO}_2}$  nm titanium dioxide (TiO<sub>2</sub>) / 100 nm Al, where PTB7 and PC<sub>61</sub>BM, PEDOT:PSS are abbreviation of poly4,8-bis[(2-ethylhexyl)oxy] benzo[1,2-b54,5-b9]dithiophene-2,6-diyl-alt-3-fluoro-2-[(2-ethylhexyl)carbonyl] thieno[3,4-b]thiophene-4,6-diyl, (6,6)-phenyl C<sub>61</sub> butyric acid methyl ester and poly(3,4-ethylenedioxythiophene) polystyrene sulfonate, respectively.

$$J_{\text{sc}} = e \int \Phi_{\text{AM1.5G}} \cdot \eta_{\text{A}} \cdot \text{IQE} \, d\lambda, \quad (2.1)$$

I first calculated the optical absorption of the multi-junction solar cells using the transfer matrix based optical modeling with free parameters of  $h_{\text{a-Si1}}$ ,  $h_{\text{a-Si2}}$ ,  $h_{\text{OPV}}$ , and  $h_{\text{TiO}_2}$ , respectively, where complex refractive indices used for simulation are determined from ellipsometry [Fig. 2.1(b)]. Then,  $J_{\text{sc}}$  of each subcell is calculated using the following equation: where  $e$  and  $\Phi_{\text{AM1.5G}}$  are the elementary charge and the photon flux of the standard air mass 1.5 G solar spectrum, respectively.  $\eta_{\text{A}}$  is the excitation rate of the photoactive layer in each subcell calculated using Eq. (1.9). I use the solar-spectrum-weighted IQE of the OPV cells determined from the ratio of  $J_{\text{sc}}$  (obtained from measured EQE) to  $J_{\text{sc,max}}$  (calculated from optical absorption assuming that the IQE is unity) as shown in Fig. 2.2(a). For a-Si cells, the IQE was assumed to have a typical value of 0.95. The lowest value among  $J_{\text{sc}}$  of each subcell is chosen to be the representative value since it must govern the  $J_{\text{sc}}$  of the triple-junction solar cells consisting of subcells connected in series. Figure 2.2(b) shows  $J_{\text{sc}}$  of the triple-junction solar cell with  $h_{\text{TiO}_2} = 20$  nm as functions of  $h_{\text{a-Si1}}$ ,  $h_{\text{a-Si2}}$ , and  $h_{\text{OPV}}$ , respectively. The maximum  $J_{\text{sc}}$  of 4.3 mA cm<sup>-2</sup> is found at  $h_{\text{a-Si1}} = 60$  nm,  $h_{\text{a-Si2}} = 400$  nm, and  $h_{\text{OPV}} = 107$  nm, which is in good agreement with the measured one of 5.1 mA cm<sup>-2</sup> at  $h_{\text{a-Si1}} = 70$  nm,  $h_{\text{a-Si2}} = 350$  nm, and  $h_{\text{OPV}} = 110$  nm. The little discrepancy between the calculated and the experimented values is likely attributed to the surface roughness that may be present in the

fabricated solar cell giving rise to scattering and then a light-trapping inside the solar cell and/or to the inaccuracy of the extracted ellipsometry data.

Figure 2.3(a) shows the effect of changes in  $t_{\text{TiO}_2}$  on  $J_{\text{sc}}$  for the triple-junction solar cell with  $h_{\text{a-Si1}} = 60$  nm,  $h_{\text{a-Si1}} = 400$  nm, and  $h_{\text{OPV}} = 107$  nm. It is found that the  $J_{\text{sc}}$  values of bottom and middle subcells depend strongly on  $h_{\text{TiO}_2}$ , while the  $J_{\text{sc}}$  of top subcell is less affected by the change. To better understand this, I investigated the spectrally and spatially resolved absorbed photon flux ( $\Phi$ ) determined by the product of  $\eta_{\text{A}}$  [Eq. (1.3)] and the incidence photon flux of solar spectrum. In Fig. 2.4, the  $\Phi$  spectrum of the bottom and the middle subcells shows interfered patterns as a consequence of multiple reflections in the multilayered architecture, while the  $\Phi$  of the top subcell shows exponentially decaying behavior due to absorption. The absorption characteristic of the top subcell seems to follow the Beer–Lambert law because of the very high extinction coefficient of the a-Si layer in the spectral range from 300 nm to 500 nm (Fig. 2.1). Thus the number of photons escaping the top subcell region is negligible in this wavelength range, meaning that changes in the layers below it have less effect on the absorption characteristics. In the wavelength range from 600 nm to 700 nm, an anti-node of standing wave appears in the bottom subcell region. The degree of positional overlap between the anti-node and the bottom subcell is mainly determined by  $h_{\text{TiO}_2}$ . This in turn affects the  $J_{\text{sc}}$  of the middle subcell as well as that of the bottom subcell since the bottom and middle subcells compete for photon absorption in the wavelength range from 550 nm to 650 nm. From the results, I can expect that  $J_{\text{sc}}$  of the triple-junction solar cell becomes maximum at  $h_{\text{TiO}_2} = 27$  nm. The  $J_{\text{sc}}$  were evaluated with varying  $h_{\text{TiO}_2}$  around 27 nm as a reference point, and found that the  $J_{\text{sc}}$  is experimentally optimized at  $h_{\text{TiO}_2} = 20$  nm. As  $h_{\text{TiO}_2}$  increased, the decrease in the electrical conductivity of  $\text{TiO}_2$  likely leads to

the optimum point appearing at a smaller  $h_{\text{TiO}_2}$  value than expected.

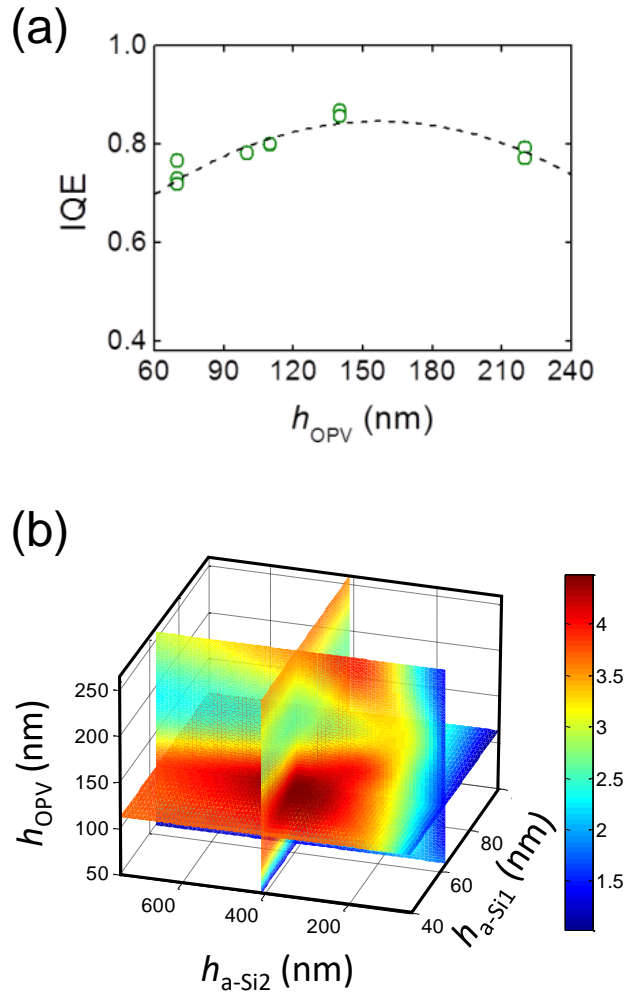


Figure 2.2 (a) Internal quantum efficiency of the PTB7-PC<sub>61</sub>BM heterojunction based solar cell as a function of the active layer thickness (symbols). The dashed line is a quadric fit with polynomial regression. (b) Simulated short-circuit current density as a function of the active layer thickness of each subcell.

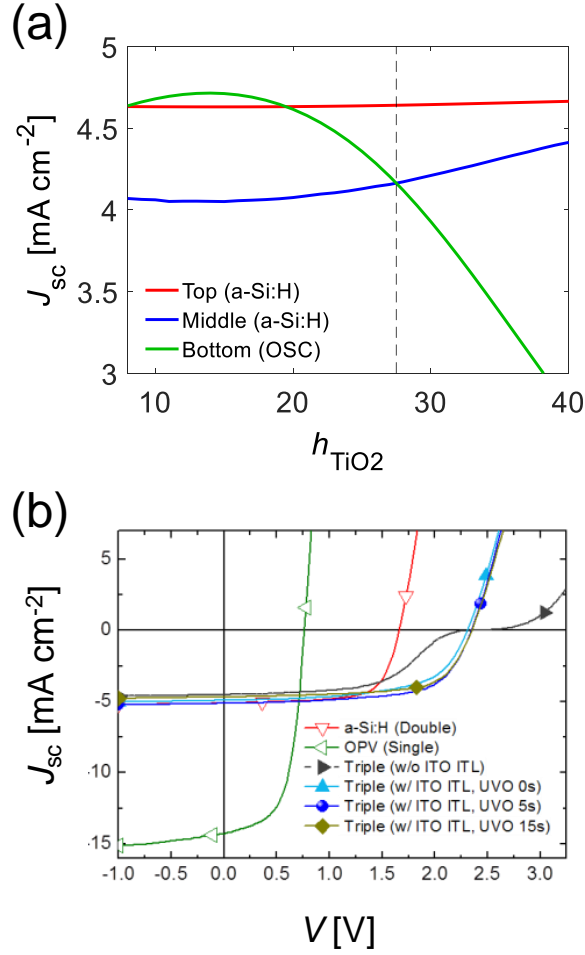


Figure 2.3 (a) TiO<sub>2</sub> thickness dependency on a short-circuit current density of each subcell. (b) Current density–voltage characteristics of the a-Si/a-Si double-junction solar cell (red), the single-junction PTB7:PC<sub>61</sub>BM based organic solar cell (green), the triple-junction solar cells with out ultraviolet ozone (UVO) treatment (cyan), that with 5 sec UVO treatment (blue), and that with 15 sec UVO treatment (olive), respectively.

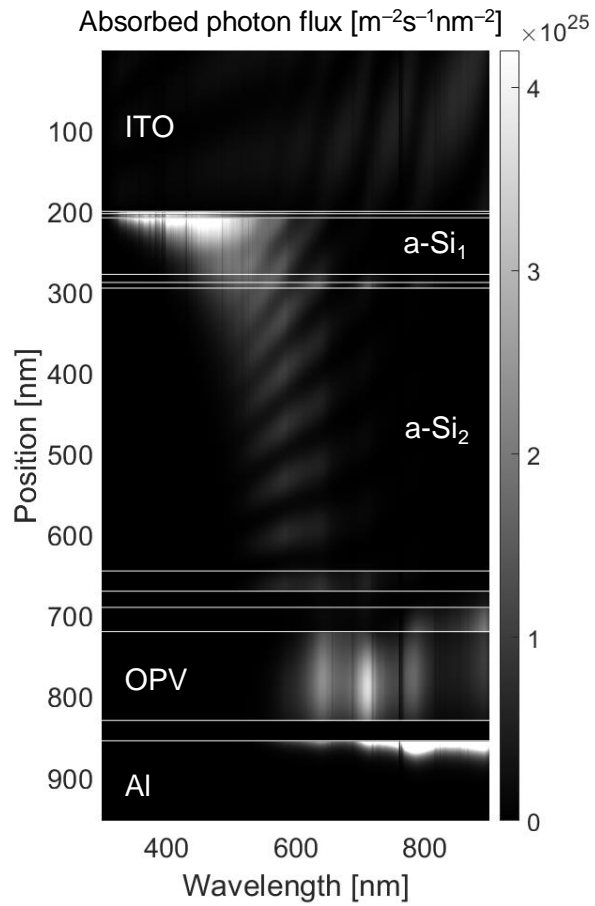


Figure 2.4 Spectrally and spatially resolved absorbed photon flux spectra of the triple-junction hybrid solar cell.

## 2.3 Enhancement of Near-Infrared Sensitivity of Organic Solar cells

### 2.3.1 Effects of Nanoscale Morphology of Lead Phthalocyanine Thin Films

In order to increase the efficiency of organic solar cells (OSCs), a number of researchers have focused not only on developing new materials for photoactive layers but also on optimizing their morphological characteristics. These efforts have led to the achievement of power conversion efficiency (PCE) of  $\sim 12\%$  for single-junction OSCs based on absorbers with optical band gaps  $E_{\text{opt}}$  of 1.5 – 1.6 eV [1, 2, 3], which is as high as an empirical estimate of the efficiency limit [4]. To further increase the PCE, the use of a tandem architecture—a serial connection of two sub-cells with different  $E_{\text{opt}}$  for complementary optical absorption—is necessary [5]. Although improving the efficiency of near-infrared (NIR) sensitive OSCs with small  $E_{\text{opt}}$  is strongly desired for overcoming the PCE limit, as well as for transparent solar cells applications, the number of organic semiconductors absorbing light in a wide NIR spectral region is quite limited. In this respect, morphological optimization of pre-developed NIR sensitive OSCs is important.

Lead phthalocyanine (PbPc) is a promising donor material for NIR sensitive OSCs because of its excellent chemical stability and high absorption coefficient in a spectral region from 550 nm to 1000 nm [6, 7]. To improve the spectral sensitivity of PbPc-based OSCs, a few studies have been performed to control the morphology of PbPc thin films, where crystalline domain size, crystal phase, and/or molecular orientation have been controlled by using a template layer [8, 9, 10, 11, 12, 13, 14], or by adjusting the deposition rate and/or the substrate temperature. [15] In particular, a template layer com-

posed of copper iodide (CuI) has been widely used to increase the optical absorption in the NIR by inducing an amorphous (or monoclinic)-to-triclinic phase transition and by aligning the direction of the transition dipole moment lying on the molecular plane with the incident electric field (i.e., by inducing a face-on molecular arrangement) [10, 11]. The increase in the crystallinity upon employing the CuI template layer, together with the face-on orientation, enhances the excitonic couplings in the  $\pi$ -stacking direction, thus facilitating the exciton diffusion [11]. However, there have been less efforts to discuss negative effects of the CuI template layer, such as exciton quenching at the CuI–PbPc interface, which may have severely limited the internal quantum efficiency (IQE) of the OSCs. Furthermore, although the morphology near donor–acceptor (D–A) interfaces may have been considerably altered in these demonstrations, discussions of the effects of change in morphology on solar cell properties have mainly been limited to bulk processes (exciton diffusion and generation), not addressing charge transfer (CT) and charge separation (CS) processes considered the key in determining the open-circuit voltage  $V_{oc}$  and the short-circuit current density  $J_{sc}$  of OSCs [16, 17, 18, 19]. In addition, previous discussions of exciton diffusion in these devices are rather incomplete, since recombination loss of CT excitons has been ignored. [10, 11]

Here, I demonstrate that, like the widely used CuI template, a new bilayer template consisting of a zinc phthalocyanine (ZnPc) layer deposited on a CuI layer induces the formation of triclinic crystallites of a PbPc film deposited on it, but introduces an increase in disorder of the orientation of PbPc molecules, which in turn enhances the solar cell performance. It is addressed that the control of molecular orientation together with the one-dimensional nanophotonic engineering is important to fully maximize the spectral sensitivity in the NIR region.

### 2.3.2 Absorption Coefficients of Lead Phthalocyanine Films

To find the effects of the change in morphology of PbPc films on their optical properties, I deposited 25-nm-thick PbPc films on the following samples: (i) glass / 160 nm ITO, (ii) glass / 160 nm ITO / 1 nm CuI, and (iii) glass / 160 nm ITO / 1 nm CuI / 6 nm ZnPc, where the CuI and CuI/ZnPc layers in the cases of (ii) and (iii), respectively, function as template layers, as in the solar cells discussed in the previous section. To characterize their morphology, I performed 2D-grazing incidence wide angle X-ray scattering (GIWAXS) measurement. The GIWAXS spectra shown in Fig. 2.5(a) to 2.5(c) are analyzed

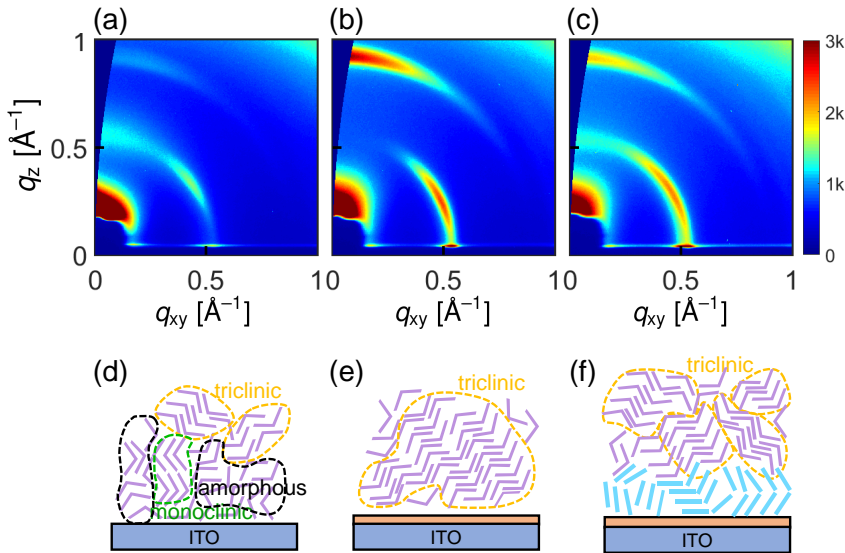


Figure 2.5 Two dimensional grazing incidence wide angle X-ray scattering (2D-GIWAXS) spectra of (a) n-PbPc, (b) c-PbPc, and (c) bi-PbPc films prepared on glass / ITO substrates. The color scale shown to the right of (c) applies to all spectra. Schematics of the crystalline structures of the (d) n-PbPc, (e) c-PbPc, and (f) bi-PbPc films. PbPc, ZnPc, and CuI are represented by angled purple rods, blue rods, and orange layers, respectively.

in Appendix A, and here we summarize the main conclusions. The weak and

diffusive signals of the non-templated PbPc (n-PbPc) thin film [Fig. 2.5(a)] indicate that this is a mixture of amorphous and crystalline domains, with no preferred molecular orientation [Fig. 2.5(d)]. The enhanced signal intensity of the CuI-templated PbPc (c-PbPc) thin film [Fig. 2.5(b)] is mostly attributed to the increased fraction of crystalline domains in triclinic phase preferentially composed of face-on oriented molecules [Fig. 2.5(e)]. Like the c-PbPc, the enhanced signal intensity of the bilayer-templated PbPc (bi-PbPc) thin film [Fig. 2.5(c)] is mainly due to the increased fraction of triclinic crystallites, but the broader signals of the bi-PbPc than the c-PbPc suggest that a smaller number of PbPc molecules in the former are, on average, in the face-on orientation, with a broader orientation distribution compared to the latter [Fig. 2.5(f)].

The complex refractive indices  $n + ik$  of the three films were determined by variable angle spectroscopic ellipsometry in a wavelength ( $\lambda$ ) range from 300 to 1100 nm. The absorption coefficient ( $\alpha$ ) spectra in Fig. 2.6 were obtained

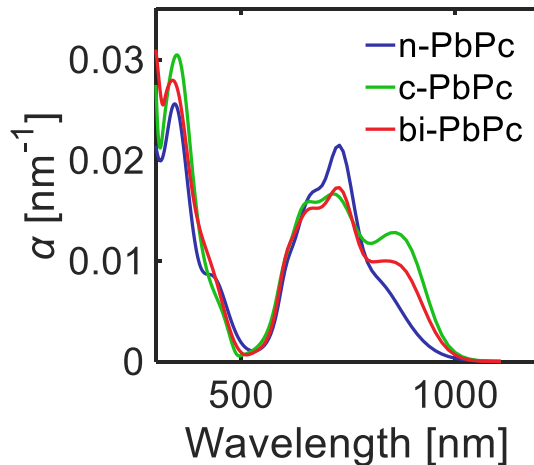


Figure 2.6 Absorption coefficient spectra of the three types of PbPc films.

using the relation:  $\alpha = 4\pi k/\lambda$ . The  $\alpha$  spectrum of the n-PbPc thin film shows

a strong peak at 740 nm, with a small shoulder around 900 nm. For PbPc crystals, the optical absorption near 740 and 900 nm is due to the monoclinic and triclinic phases, respectively [10, 11]. The characteristics of a PbPc film templated by a bilayer consisting of ZnPc deposited on CuI (bi-PbPc) are similar to the c-PbPc film: both films show increased optical absorption in the NIR region compared to the n-PbPc film deposited on ITO. The presence of the bi-layer template causes the triclinic PbPc crystallites to have a broader orientational distribution, which decreases the overall alignment between the directions of incident electric field and transition dipole moment of the PbPc molecules in triclinic phase, resulting into a smaller optical absorption of the bi-PbPc than the c-PbPc in the NIR region.

### 2.3.3 Solar Cell Performances

Figure 2.7 shows short-circuit current density ( $J_{sc}$ ) of OSCs, measured under 1-sun AM 1.5G illumination, having the following structure: glass / 160 nm indium tin oxide (ITO) / template layer /  $t_A$  nm PbPc / 35 nm C<sub>60</sub> / 8 nm bathocuproine (BCP) / 100 nm Ag, as a function of the thickness of the PbPc layer ( $t_A$ ). Between the ITO and PbPc layers, 1 nm copper iodide (CuI) or 6 nm zinc phthalocyanine (ZnPc) deposited on 1 nm CuI was employed as a template layer. In the following, the solar cell with the CuI or CuI/ZnPc template layer is referred to as the c-PbPc or bi-PbPc device, respectively. The  $J_{sc}$  data is normalized to the maximum value of each device. I have fitted the experimental data (symbols) to the simulation data (lines) and find the  $t_A$  values where  $J_{sc}$  maxima appears:  $t_A = 25$  nm and 30 nm for the bi-PbPc and c-PbPc, respectively. Here, combination of transfer matrix based optical modeling and exciton diffusion model was used for the simulation as in Appendix B. The presence of  $J_{sc}$  maxima is due to the tradeoff between the

light absorption and the exciton diffusion characteristics: as  $t_A$  increases, the optical absorption increases while the probability that the exciton generated in the PbPc layer reaches the donor–acceptor interface decreases. Note that considering both the fill factor (FF) and the open-circuit voltage ( $V_{oc}$ ), the c-PbPc device also has the maximum power conversion efficiency (PCE) at  $t_A \sim 25$  nm (data is not shown). Thus in the following discussions, the thickness of PbPc will be fixed to be 25 nm. Before discussing the solar cell performances in detail, the spatially and spectrally resolved optical density and absorption distributions are investigated. Figures 2.8(a–c) show that the antinodes of

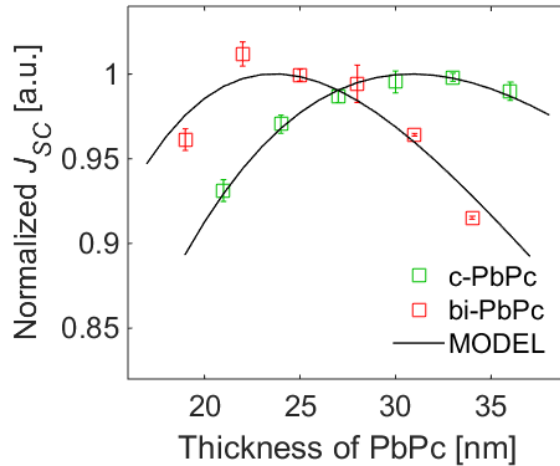


Figure 2.7 Dependence of short-circuit current density on the thickness of the PbPc layer. The symbols are experimental data and the lines are fits to them.

EM waves in the NIR region in the ITO layer. If the thickness of PbPc is increased, the antinodes will be located on the PbPc side, but in this case, the quantum efficiency decreases due to the decrease of the exciton diffusion efficiency. Compared to the absorption profiles of the n-PbPc [Fig. 2.7(d)], the absorption at around 900 nm of the c-PbPc device [Fig. 2.7(e)] was greatly

Table 2.1 Solar cell parameters (short-circuit current density  $J_{sc}$ , open-circuit voltage  $V_{oc}$ , fill factor FF, and power-conversion efficiency PCE) extracted from the current density–voltage characteristics measured under 1-sun AM 1.5G illumination. Also listed in the table are the optical band gaps  $E_{opt}$  of the PbPc films and a ZnPc film. Averages of the solar cell parameters were taken across 6–8 devices.

Device	$J_{sc}^a$ [mA cm <sup>-2</sup> ]	$V_{oc}$ [mV]	FF [%]	PCE <sup>a</sup> [%]	$E_{opt}$ [eV]
n-PbPc	6.55 ± 0.08	510 ± 5	54.3 ± 0.8	1.81 ± 0.03	1.29
c-PbPc	9.32 ± 0.12	475 ± 5	61.4 ± 0.2	2.72 ± 0.05	1.25
bi-PbPc	10.41 ± 0.14	489 ± 3	60.2 ± 0.3	3.06 ± 0.04	1.26
ZnPc					1.51

<sup>a</sup> corrected using the spectral mismatch factor.

increased due to the formation of triclinic crystallites composed of face-on oriented molecules. The bi-PbPc device [Fig. 2.7(f)], the PbPc molecules of which is less face-on, shows weaker absorption than the c-PbPc, indicating that the face-on orientation of the c-PbPc is desirable for absorption.

### 2.3.4 Analysis of the Enhanced Spectral Responsivity in the Near-Infrared Spectral Region

Figure 2.9 shows current density–voltage ( $J$ – $V$ ) characteristics of OSCs, measured under 1-sun AM 1.5G illumination. The values of  $J_{sc}$ ,  $V_{oc}$ , FF, and PCE are listed in Table 1, where  $J_{sc}$  and PCE were corrected using the spectral mismatch factor [20]. Compared to the n-PbPc device,  $J_{sc}$  and FF of the c-PbPc device are significantly increased, leading to the improvement of PCE from 1.8% to 2.7% despite the reduction of  $V_{oc}$ . The bi-PbPc device shows a further improved PCE of 3.1%, which is attributed to the larger values of both  $J_{sc}$  and  $V_{oc}$ , with an almost identical FF, compared to the c-PbPc device.

In Fig. 2.10(a), the external quantum efficiency (EQE) spectra of the de-

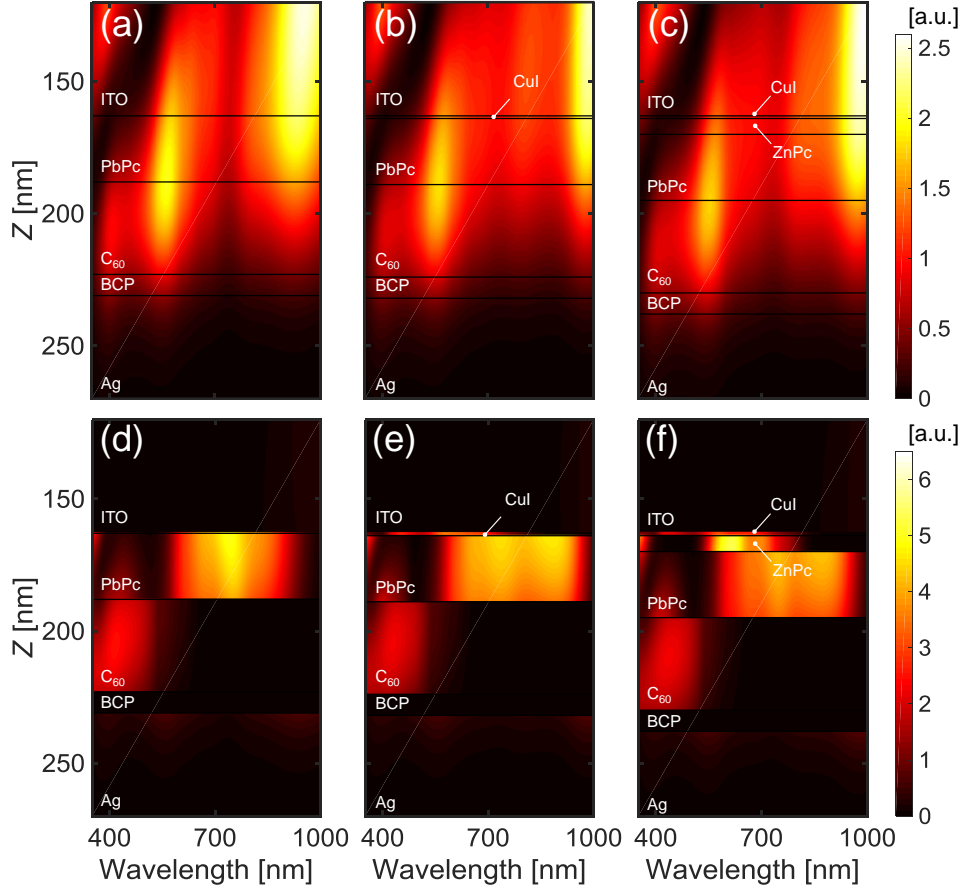


Figure 2.8 Normalized optical density  $|E(\lambda, z)|^2/|E_0|^2$  of the (a) n-PbPc, (b) c-PbPc, and (c) bi-PbPc devices, where the  $E$  and  $E_0$  are the complex electric field in each device and the amplitude of the incident electric field, respectively, and  $z$  is the distance from the glass-ITO interface. The time averaged absorbed power  $\Phi$  of the (d) n-PbPc, (e) c-PbPc, and (f) bi-PbPc devices, calculated using the relation:  $\Phi(\lambda, z) = \frac{1}{2}\omega\text{Im}(\epsilon)|E|^2$ , where  $\omega$  and  $\epsilon$  are the angular frequency of the incident light and the permittivity in each layer, respectively.

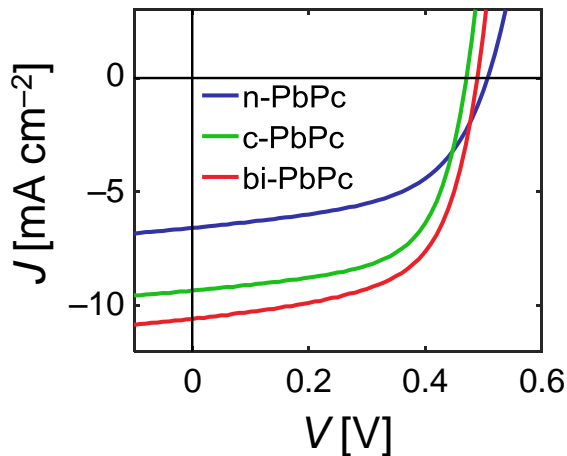


Figure 2.9 Current density–voltage characteristics ( $J$ – $V$ ) of the n-PbPc (blue), c-PbPc (green), and bi-PbPc (red) devices under 1-sun AM 1.5G illumination.

vices measured under zero bias are shown (solid lines), indicating that the increase in  $J_{sc}$  is mainly attributed to the increased response in the spectral region from 550 to 1000 nm. To better identify the origins of this feature, we first calculated the absorption efficiency  $\eta_{abs}$  of the  $C_{60}$  (or PbPc) layer in each device, defined as the number of photons absorbed in that layer per unit time divided by the number of incident photons per unit time. The calculation was based on the transfer matrix method [21], with the complex refractive indices of the constituent thin films obtained by spectroscopic ellipsometry, assuming that the films are homogeneous. The  $\eta_{abs}$  spectra of the PbPc and  $C_{60}$  layers in the three devices, shown in Fig. 2.10(b), indicate that although increased light absorption in the c- and bi-PbPc devices near 900 nm is consistent with their EQEs being larger than the EQE of the n-PbPc device in that spectral region, the change in light absorption cannot fully explain the EQE spectra. For example, the EQEs of the c- and bi-PbPc devices are larger than the n-PbPc device in the entire spectral region ranging from 550 to 1000 nm, while it is not the case for  $\eta_{abs}$ . Also,  $\eta_{abs}$  of the c-PbPc device is larger than the

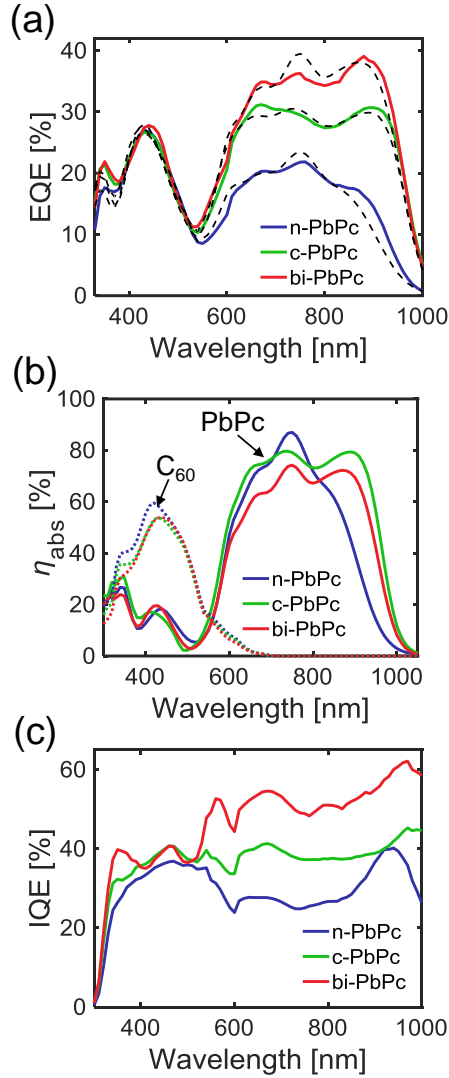


Figure 2.10 (a) External quantum efficiency of the n-PbPc (blue), c-PbPc (green), and bi-PbPc (red) devices. Solid and dashed lines indicate the measured and simulated data, respectively. (b) Absorption efficiency  $\eta_{abs}$  of the PbPc (solid lines) and C<sub>60</sub> (dashed lines) layers in each device. (c) Internal quantum efficiency of each device.

bi-PbPc device in that spectral region, but the bi-PbPc is larger in EQE. The IQE spectra, obtained by dividing the EQE spectra by the sum of  $\eta_{\text{abs}}$  of the PbPc and  $C_{60}$  layers, reveal that the change in IQE upon employing template layers is dominant in determining the EQE spectra [Fig. 2.10(c)]. Here, the IQE is defined as the number of electrons collected at the electrode per unit time divided by the number of photons absorbed in the active layer (the PbPc or  $C_{60}$ ) per unit time. To fully understand the effects of the morphological change on solar cell performances, the discussions of the IQE should be accompanied, which will be addressed in detail in Appendices B and B.2.

### 2.3.5 Experimental Details

*Sample Fabrication:* ITO-coated glass substrates ( $15 \Omega/\text{sq}$ ,  $25 \text{ mm} \times 25 \text{ mm}$ ) were cleaned in an ultrasonic bath with detergent, de-ionized water, acetone, and isopropyl alcohol, sequentially. After drying the substrates at  $200 \text{ }^\circ\text{C}$  in a vacuum oven, they were exposed to UV-ozone for 15 min. The materials—ZnPc (CreaPhys),  $\text{C}_{60}$  (CreaPhys), PbPc (Jilin OLED), BCP (EM index), CuI (Sigma Aldrich), and Ag—were deposited on the prepared substrates using a vacuum thermal evaporator with a base pressure of approximately  $3 \times 10^{-7} \text{ Torr}$  and a growth rate of  $0.1 \text{ nm s}^{-1}$ . The solar cell area of  $1 \text{ mm} \times 1 \text{ mm}$  is determined by the cross section between the pre-patterned ITO electrode and the Ag electrode deposited through a shadow mask.

*2D-GIWAXS measurement:* 2D-GIWAXS measurement was performed at the 3C beam line in Pohang Accelerator Laboratory, Korea. The wavelength of the incident X-ray was  $1.231 \text{ \AA}$  and the incident angle was chosen to be the critical angle of  $\sim 0.25^\circ$ . Diffracted X-ray signals were collected by a two-dimensional charge-coupled device (SX165, Rayonix) with a pixel size of  $79.01 \mu\text{m} \times 79.01 \mu\text{m}$ .

*Characterizations of Optical Properties:* The complex refractive indices  $n + ik$  of the organic thin films were determined using variable angle spectroscopic ellipsometry (VASE, Woollam) in a wavelength range  $\lambda$  from 300 to 1100 nm. The absorption coefficients  $\alpha$  were obtained using the relation:  $\alpha = 4\pi k/\lambda$ . The absorption efficiencies of the PbPc and  $\text{C}_{60}$  layers in each solar cell were calculated using the transfer matrix formalism [21].

*Current Density–Voltage Characteristics:*  $J$ – $V$  characteristics were measured under dark and AM 1.5G illumination using a solar simulator (L01, Peccell)

and a source meter (2400, Keithley). The light intensity (100 mW) was calibrated using a Si photodiode with a KG-5 filter (BS-520, Bunkoukeiki). The  $J_{sc}$  and PCE values obtained from the  $J$ - $V$  curves were corrected using the spectral mismatch factor [20]. The temperature-dependent  $J$ - $V$  characteristics were obtained in an open-cycle liquid nitrogen cryostat.

*EQE measurement:* The monochromatic light incident on the OSCs, obtained from a laser-driven Xe light source (EQ-99, Energetiq) coupled to a monochromator, was modulated by a chopper at a frequency of  $\sim 400$  Hz, and the photocurrent of the devices was measured using a current amplifier (SR570, Stanford Research) and a lock-in amplifier (SR830, Stanford Research).

*UPS measurement:* UPS experiments were carried out in a modified Kratos AXIS-165 system with a He I light-source, where the organic films were deposited in a vacuum thermal evaporator connected to the analysis chamber with a base pressure of  $\sim 10^{-9}$  Torr.

## 2.4 Circularly Polarized Light Emission from Multi-layer Organic Light Emitting Diodes

### 2.4.1 Electromagnetic Description of Circularly Polarized Light Emitters

In recent years, ultracompact circularly polarized light (CPL) emitting organic diodes (henceforth referred to as CP-OLED) have attracted much attention for various applications, such as quantum information systems and highly bright 2-D and 3-D OLED displays. CPL emitters are more desired than linearly polarized light (LPL) emitters for information transmission due to the longer time taken to be fully depolarized by unintentional scattering [22]. In addition, the external quantum efficiency ( $\eta_E$ ) of OLED displays, currently limited to 50% by the presence of antiglare filter [23], can be significantly improved by using CP-OLED because of the high transparency of the antiglare filter to one helicity of CPL. Unfortunately, the tradeoff between  $\eta_E$  and the dissymmetry factor of the luminous intensity ( $g_L$ ) has made it challenging to practical use of CP-OLEDs. In addition, even for a chiral emitter with a high  $g_L$  value intrinsically, when it is employed into a conventional OLED structure consisting of organic multilayers interposed by transparent top and optically thick bottom electrodes,  $g_L$  of the device has been very small due to the helicity-inversion of the backward emitted light at the bottom electrode [23, 22]. For an extreme case,  $g_L$  is zero if the forward emission property of an emitter in an OLED is identical to its backward emission property.

The analytic model based on Dyadic Green's functions [24], widely used to maximize  $\eta_E$  of one dimensional multilayer OLED, suggests that the forward and backward emission properties are identical only when the structure is symmetric with respect to the emission layer. This model, more importantly,

implies that by adjusting the optical parameters, such as the thicknesses and refractive indices of the constituent layers, more asymmetric behavior between the forward and backward emissions can be obtained, which is desirable for increasing  $g_L$  of OLEDs. Thus, to rationally optimize CP-OLED in terms of  $g_L$  as well as  $\eta_E$ , comprehensive understandings of its optical characteristics based on a device model is necessary. Zinna *et al.* suggested a simple mathematical model for CP-OLEDs based on the Beer–Lambert law, concluding that  $g_L$  increases with the emitter-to-cathode separation [22]. However, their model does not properly deal with nanophotonic phenomena, such as interference, waveguide, and Purcell effect, important for analyzing OLED characteristics [25]. Lee *et al.* demonstrated another model for CPL emission from cholesteric stacking of conjugated polymers. The CPL emission described by the model, in which CPL originates from the phase modification of LPL by the compact waveplate consisting of the polymers that also functions as the LPL emitter, has a different physical origin to the typical CP-OLEDs based on chiral molecules. Therefore, this model is not generally applicable to other studies for CP-OLEDs.

Here, I demonstrate numerical simulations of multilayer CP-OLEDs based on chiral molecular emitters for understandings of their optical and chiroptical characteristics comprehensively. CPL emitters are described electromagnetically in two ways: (i) two oscillating electric point-dipoles (ED) with a mutual phase difference of  $\pi/2$  (henceforth referred to as ED $\perp$ ED), and (ii) ED and a magnetic point dipole (MD) oscillating in-phase (henceforth referred to as ED $\parallel$ MD). The constituting dipoles of ED $\perp$ ED (or ED $\parallel$ MD) are at a point. The types (i) and (ii) mimic CPL emitters described by the asymmetric excitonic coupling and the magnetically allowed transition, respectively, in the chemistry and biochemistry communities [26, 27]. For all calculations, COM-

SOL Multiphysics software, a finite element modeling tool, is used.

### 2.4.2 Circularly Polarized Light Emitters in Vacuum

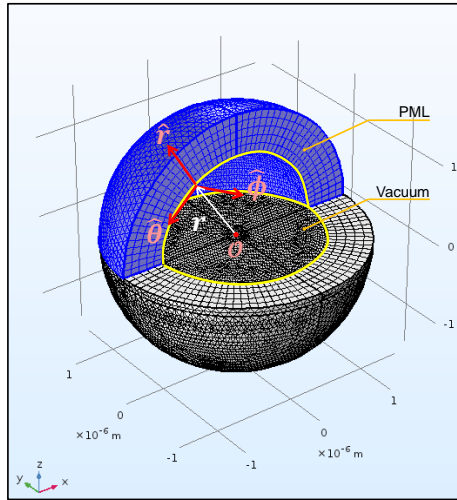


Figure 2.11 Schematic illustration of the simulation geometry of a CPL emitter in vacuum. The yellow lines denote the monitoring surface of  $r = 1.5 \mu\text{m}$ .

I first investigated the radiation characteristics of CPL emitters in vacuum. Figure 2.11 is a schematic illustration of the simulation geometry, where the spherical vacuum domain with radius  $r = 1.5 \mu\text{m}$  is enclosed by the shell serving a perfectly matched layer (PML). This is an artificial absorbing layer introduced to prevent scattering at the outermost surface of the simulation domain of interest, and thus enabling the simulation of an infinite vacuum space. A CPL emitter is located at the origin ( $\mathcal{O}$ ) marked with the red dot. The monitoring surface denoted by yellow lines is at  $r = 1.5 \mu\text{m}$  for quantifying the radiation characteristics. The radiation power per unit area from a CPL emitter is calculated at the monitoring surface using the following equation:

$$\langle S(\theta, \phi) \rangle = \frac{\text{Re}(\tilde{\mathbf{E}} \times \tilde{\mathbf{H}}^*)}{2}, \quad (2.2)$$

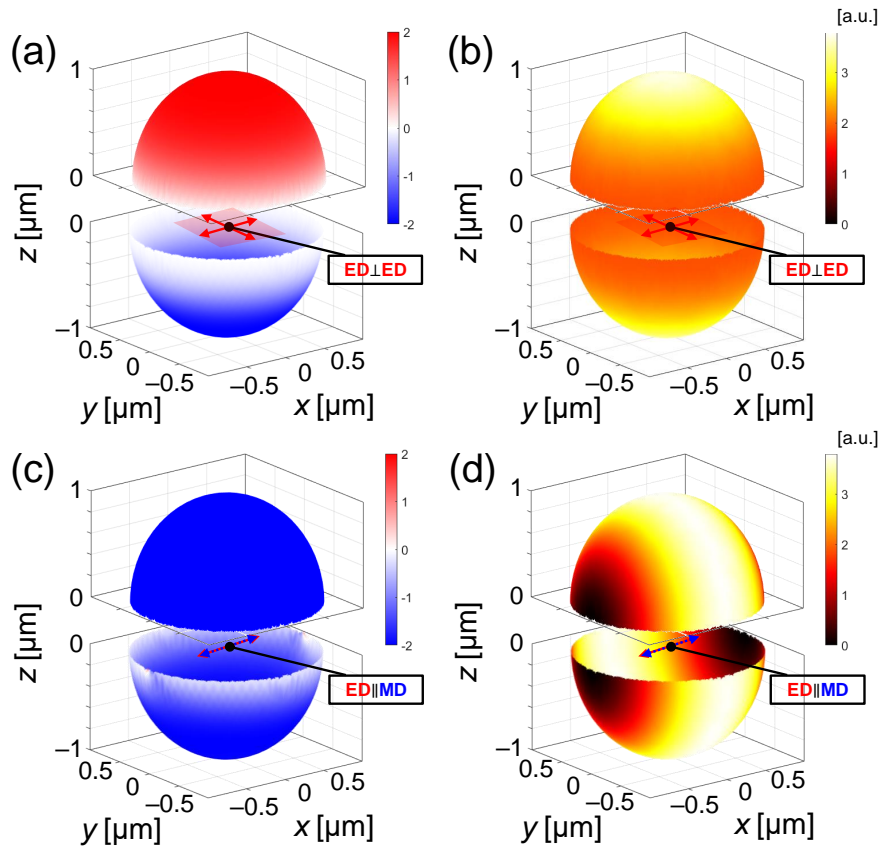


Figure 2.12 (a) The dissymmetry factor and (b) the radiation power per unit area from  $ED \perp ED$ . (c) The dissymmetry factor and (d) the radiation power per unit area from  $ED \parallel MD$ . They are calculated at the monitoring surface of  $r = 1.5 \mu\text{m}$ .

where  $\mathbf{E}$  is the electric fields and  $\mathbf{H}$  is the magnetic field divided by the permeability in vacuum. Next, the distribution of  $g_L$  at the monitoring surface is calculated from:

$$g_L = 2 \frac{|\mathbf{E}^l|^2 - |\mathbf{E}^r|^2}{|\mathbf{E}^l|^2 + |\mathbf{E}^r|^2}, \quad (2.3)$$

where the superscripts  $l$  and  $r$  denote the left and right handed circularly polarized light, respectively.  $\mathbf{E}^{l/r}$  is  $\mathbf{E}_\phi \mp i\mathbf{E}_\theta$ , where  $E_i$  is the  $i$  component of  $\mathbf{E}$  in the spherical coordinate, and  $\theta$  and  $\phi$  are the polar and the azimuthal angles, respectively. Figures 2.12(a) and 2.12(b) show the distributions of  $g_L$  and  $\langle S(\theta, \phi) \rangle$  for ED $\perp$ ED with the wavelength ( $\lambda$ ) of 535 nm, and Figs. 2.12(c) and 2.12(d) show those for ED $\parallel$ MD with  $\lambda = 535$  nm. The  $g_L$  distribution of ED $\perp$ ED in the upper hemisphere (i.e.,  $k_z > 0$ ) has opposite sign compared to that in the lower hemisphere (i.e.,  $k_z < 0$ ), while the  $g_L$  of ED $\parallel$ MD has identical sign for all wavevectors  $\mathbf{k}$ , where  $k_i$  is the  $i$  component of  $\mathbf{k}$ . For ED $\perp$ ED, the radiation power distribution features a cylindrical rotation-symmetry with respect to the  $z$  axis and power maxima in  $\pm k_z$  directions [Fig. 2.12(b)]. This is in contrast to the ED $\parallel$ MD case [Fig. 2.12(d)], featuring a rotation-symmetry with respect to the  $y$  axis and no emission in the  $\pm k_y$  direction with which the dipoles aligned.

### 2.4.3 Circularly Polarized Light Emitters in a Multilayer Structure

To simulate CP-OLEDs, the CPL emitters are embedded in the organic layer of the following multilayer structure [Fig. 2.13(a)]: glass /160 nm indium tin oxide (ITO)/  $h + 50$  nm organic layer / 400 nm aluminum (Al). The refractive indices of the glass and organic layers were assumed to be 1.5 and 1.8, respectively, and the complex refractive indices of ITO and Al at  $\lambda = 535$  nm were taken from the literature [24, 28]. A CPL emitter with  $\lambda = 535$  nm in

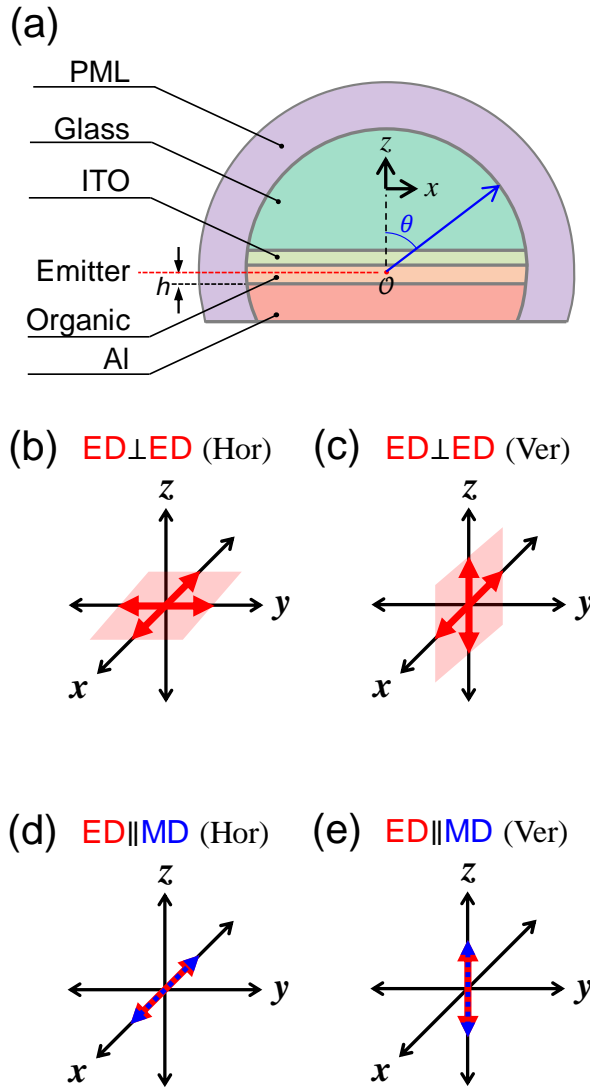


Figure 2.13 (a) Schematic illustration of the simulation geometry of a CP-OLED. (b) Horizontally- and (c) vertically-oriented  $ED \perp ED$ s. (d) Horizontally- and (e) vertically-oriented  $ED \parallel MD$ s.

vacuum is positioned at the origin denoted by the red dot, and the emitter-to-ITO separation is 50 nm. The entire simulation geometry is chosen to be the shape of a truncated sphere enveloped by a PML layer to effectively prevent the scattering at the PML–multilayer interface. Although the local refractive index of the PML is depending on that of the adjacent material, PML is illustrated as a single domain for simplicity. The orientation of ED||MD is parallel to the constituent dipoles [Figs. 2.13(d) and 2.13(e)], and that of ED⊥ED is somewhat complex: it is horizontally-(or vertically-) oriented when a normal of the plane including the constituent dipoles is parallel to the  $z$  (or  $x$ ) axis as shown in Fig. 2.13(b) [or Fig. 2.13(c)]. All physics arising from an arbitrarily-oriented CPL emitter can be described using one horizontally- and one vertically-oriented CPL emitters due to a cylindrical rotation-symmetry of the multilayer structure with respect to the  $z$  axis. In Fig. 2.13(a),  $\theta$  is illustrated while  $\phi$  is omitted for simplicity.

Figure 2.14 shows the radiation-power-weighted average of the dissymmetry factor in the luminous intensity ( $g_M$ ) calculated using the following equation:

$$g_M = \frac{\int_0^{2\pi} \int_0^{\theta_C} g_L(\theta, \phi) \langle S(\theta, \phi) \rangle R^2 \sin(\theta) d\theta d\phi}{\int_0^{2\pi} \int_0^{\theta_C} \langle S(\theta, \phi) \rangle R^2 \sin(\theta) d\theta d\phi} \quad (2.4)$$

where  $\theta_C$  is the critical angle at the glass–air interface and  $R$  is 1.5  $\mu\text{m}$  being the distance from the origin to the monitoring surface. Notably,  $g_M$  of ED⊥ED less depends on  $h$  but dramatically changes with the orientation:  $g_M$  for the horizontally-oriented ED⊥ED ( $g_M^H$ ) is close to 2 [gray line in Fig. 2.14(a)], whereas  $g_M$  for the vertically-oriented ED⊥ED ( $g_M^V$ ) is almost 0 for the vertical orientation [gray line in Fig. 2.14(b)]. For the horizontally-oriented case, the emitted CPL propagating toward the region with  $z > 0$  has an opposite helicity to that propagating toward the region with  $z < 0$  [Fig. 2.12(a)]. Since the

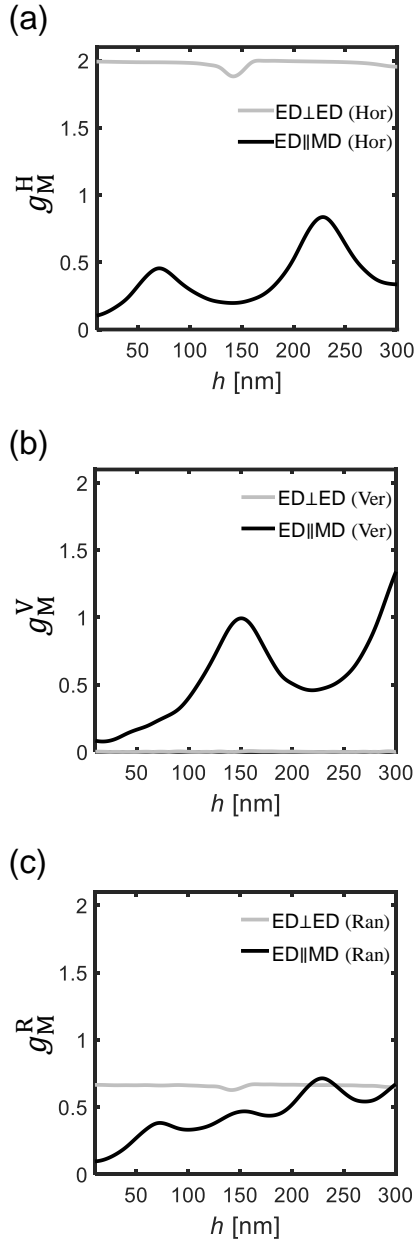


Figure 2.14 Radiation-power-weighted averages of the dissymmetry factor in luminous intensity for the (a) horizontally-, (b) vertically-, and (c) randomly-oriented CPL emitters.

former must undergoes internal reflection once more than the latter before being outcoupled to the air, the helicity of CPL emitted into the air is always identical regardless of the initial  $k_z$  value, thus less depending on  $h$ . The  $g_M^V$  value calculated at the monitoring surface with  $z > 0$  is always zero due to the vertical orientation together with the antisymmetric  $g_L$  distribution with respect to the plane parallel to the constituent dipoles [Fig. 2.12(a)]. For ED||MD [black lines in Figs. 2.14(a) and 2.14(b)],  $g_M^H$  and  $g_M^V$  oscillates with  $h$ , and the  $h$  values where local extrema occur change depending on the orientation: the local  $g_M^H$  maxima are observed at  $h = 69$  and  $229$  nm, while the local  $g_M^V$  maxima is observed at  $h = 150$  nm. Such oscillating feature suggests that there is  $h$ -dependency on the ratio between the power of the forward emission and that of the backward emission from ED||MD before undergoing the internal reflections. Figure 2.14(c) shows  $g_M$  for the randomly-oriented case ( $g_M^R$ ) calculated from:

$$g_M^R = \frac{1}{3}g_M^H + \frac{2}{3}g_M^V \quad (\text{for ED}\perp\text{ED}), \quad (2.5)$$

and

$$g_M^R = \frac{2}{3}g_M^H + \frac{1}{3}g_M^V \quad (\text{for ED}\parallel\text{MD}). \quad (2.6)$$

Note that the prefactors in Eq. (2.5) are different to those in Eq. (2.6). The  $g_M^R$  value of ED $\perp$ ED is  $\sim 0.67$  for most  $h$  [gray line in Fig. 2.14(c)], whereas that of ED||MD is very small at  $h = 0$ , which tends to increase with  $h$  despite a little fluctuation [black line in Fig. 2.14(c)]. These results suggest that despite the previous pessimistic projections on CP-OLEDs due to the helicity inversion, the moderate  $g_M$  values can be achieved through optimization of the device structure even without the orientation control: the  $g_M^R$  value of ED $\perp$ ED for most  $h$  is 33.5 % of the ideal value, i.e., 2, and that of ED||MD at  $h = 229$  nm

is 35.5 % of the ideal value. If the orientation can be controlled,  $g_M$  will be closer to the ideal value [Figs. 2.14(a) and 2.14(b)].

Figure 2.15 shows the energy transfer efficiency ( $\eta_T$ ), quantifying how much the energy of a CPL emitter is transferred into each layer, calculated from:

$$\eta_{T,\mathcal{L}} = \frac{\int_0^{2\pi} \int_{\theta_i}^{\theta_f} \langle S(\theta, \phi) \rangle R^2 \sin(\theta) d\theta d\phi + \int_{\mathcal{V}} \mathbf{J} \cdot \mathbf{E} dV}{P_0}. \quad (2.7)$$

Here,  $\mathcal{L}$  is the layer index ( $\mathcal{L} = M, O, I,$  and  $G$  for the aluminum, organic, ITO, and glass layers, respectively), and  $\mathcal{V}$  is the volume of each layer.  $\theta_i$  and  $\theta_f$  are the initial and final values of the radial angle range for the integral, varying with  $\mathcal{L}$ . In Fig. 2.15, also shown is the energy transfer efficiency into the air ( $\mathcal{L} = A$ ) calculated from:

$$\eta_{T,A} = \frac{\int_0^{2\pi} \int_0^{\theta_C} \langle S(\theta, \phi) \rangle R^2 \sin(\theta) d\theta d\phi}{P_0}, \quad (2.8)$$

where  $P_0$  is the radiation power of a CPL emitter calculated at the spherical monitoring surface with the radius ( $R_d$ ) of 7.5 nm centered at the origin using the following equation:

$$\mathbf{P}_0 = \int_0^{2\pi} \int_0^{\theta_C} \langle S(\theta, \phi) \rangle R_d^2 \sin(\theta) d\theta d\phi \quad (2.9)$$

Figure 2.15(a) is  $\eta_T$  of the horizontally-oriented ED||ED, which is similar with that of the conventional OLED based on a single horizontally-oriented ED source [29]: (i) when  $h$  is close to zero, the energy dissipation in the bottom metal predominates over the other processes attributed to the efficient near-field coupling in a non-radiative manner, which decreases with  $h$ , (ii)  $\eta_{T,A}$  oscillates with  $h$ , due to the change in the coupling between the Fabry-Pérot resonance and the excitation dipole source. Figure 2.15(b) shows the increased

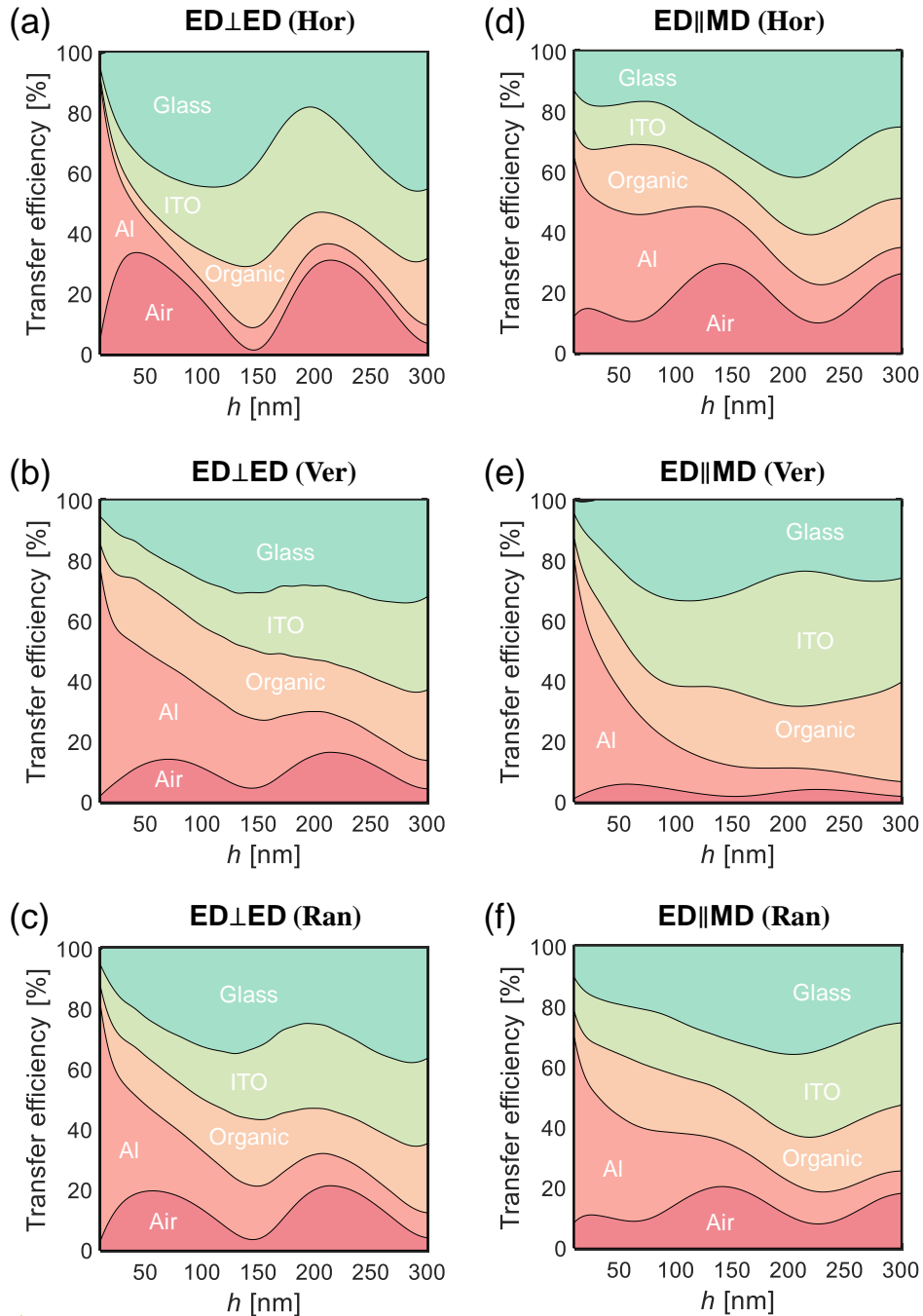


Figure 2.15 The dipole energy transfer efficiencies from ED $\perp$ LED (a–c) and ED $\parallel$ MD (d–f) whose orientations are denoted in top of each figure.

$\eta_{T,M}$  of the vertically-oriented ED||ED compared to the horizontally-oriented case, originating from the presence of the vertical ED component, constituting the vertically-oriented ED $\perp$ ED [Fig. 2.13(c)], matched to the  $E_z$  component of the surface plasmon polariton (SPP) bounded at the Al-organic interface. It is worthwhile to note that the vertically-oriented ED $\perp$ ED excites SPP and waveguide modes propagating unidirectionally, discussed elsewhere [30]. Figure 2.15(d) shows that  $\eta_{T,A}$  of the horizontally-oriented ED||MD at  $h = 0$  is much larger than any other cases. This is attributed to the inefficient energy transfer between a single MD source and a metal layer: the non-radiative quenching rate of MD is proportional to  $a^{-0.8}$ , while that of ED is proportional to  $a^{-3}$ , where  $a$  is the dipole-to-metal separation [31]. In Fig. 2.15(e),  $\eta_{T,A}$  of the vertically-oriented ED||MD is the smallest due to the absence of a horizontal component among the constituent dipoles. Figures 2.15(c) and 2.15(f) are  $\eta_T$  of the randomly-oriented CPL emitters calculated from Figures 2.15(a,b) and 2.15(d,e) using the prefactors with the similar manner in Eqs. 2.5 and 2.6. Since  $g_M^R$  of ED $\perp$ ED is almost constant to  $h$  [Fig. 2.14(c)],  $(h, g_M^R, \eta_{T,A}) = (214 \text{ nm}, 0.67, 21.4 \%)$  corresponding to the second order cavity with the highest  $\eta_{T,A}$  is desirable for CP-OLEDs [Fig. 2.15(c)]. The ED||MD case, on the other hand, tends to have a larger  $g_M^R$  as  $h$  increases [Fig. 2.14(c)], so that  $(h, g_M^R, \eta_{T,A}) = (300 \text{ nm}, 0.67, 18.1 \%)$  corresponding to the third order cavity mode is likely better than  $(h, g_M^R, \eta_{T,A}) = (139 \text{ nm}, 0.4, 20.4 \%)$  corresponding to the second order cavity mode [Fig. 2.14(f)] because of the much larger  $g_M^R$ .

To summarize, I have demonstrated for the first time that the chiroptical and nanophotonic properties of CP-OLED are greatly influenced by the origin of the CPL emitter as well as the structure of the device. The helicity-inversion caused by the optically-thick metal layer existing in conventional OLEDs seemed very pessimistic for developing CP-OLEDs, but it has been

found to be sufficiently overcome by the control of molecular orientation and the optimization of the device structure. In this study, although ideal CPL emitters were assumed, the results are applicable to typical CP-OLEDs, and thus expected to help their rational design.

## 2.5 Bibliography

- [1] J. Zhao, Y. Li, G. Yang, K. Jiang, H. Lin, H. Ade, W. Ma, and H. Yan, “Efficient organic solar cells processed from hydrocarbon solvents,” *Nat. Energy*, vol. 1, no. 2, a. 15027, 2016.
- [2] V. Vohra, K. Kawashima, T. Kakara, T. Koganezawa, I. Osaka, K. Takimiya, and H. Murata, “Efficient inverted polymer solar cells employing favourable molecular orientation,” *Nat. Photonics*, vol. 9, no. 6, pp. 403–408, 2015.
- [3] Y. Liu, J. Zhao, Z. Li, C. Mu, W. Ma, H. Hu, K. Jiang, H. Lin, H. Ade, and H. Yan, “Aggregation and morphology control enables multiple cases of high-efficiency polymer solar cells,” *Nat. Commun.*, vol. 5, a. 5293, 2014.
- [4] R. A. J. Janssen and J. Nelson, “Factors limiting device efficiency in organic photovoltaics,” *Adv. Mater.*, vol. 25, no. 13, pp. 1847–1858, 2013.
- [5] H. Tan, A. Furlan, W. Li, K. Arapov, R. Santbergen, M. M. Wienk, M. Zeman, A. H. Smets, and R. A. Janssen, “Highly efficient hybrid polymer and amorphous silicon multijunction solar cells with effective optical management,” *Adv. Mater.*, vol. 28, no. 11, pp. 2170–2177, 2016.
- [6] A. Miyamoto, K. Nichogi, A. Taomoto, T. Nambu, and M. Murakami, “Structural control of evaporated lead-phthalocyanine films,” *Thin Solid Films*, vol. 256, no. 1, pp. 64–67, 1995.
- [7] D. Campbell and R. A. Collins, “Spectral response of monoclinic and triclinic lead phthalocyanine to nitrogen-dioxide,” *Thin Solid Films*, vol. 261, no. 1, pp. 311–316, 1995.

- [8] M. Hiramoto, K. Kitada, K. Iketaki, and T. Kaji, “Near infrared light driven organic p-i-n solar cells incorporating phthalocyanine j-aggregate,” *Appl. Phys. Lett.*, vol. 98, no. 2, a. 023302, 2011.
- [9] W. Zhao, J. P. Mudrick, Y. Zheng, W. T. Hammond, Y. Yang, and J. Xue, “Enhancing photovoltaic response of organic solar cells using a crystalline molecular template,” *Org. Electron.*, vol. 13, no. 1, pp. 129–135, 2012.
- [10] H. S. Shim, H. J. Kim, J. W. Kim, S. Y. Kim, W. I. Jeong, T. M. Kim, and J.- J. Kim, “Enhancement of near-infrared absorption with high fill factor in lead phthalocyanine-based organic solar cells,” *J. Mater. Chem.*, vol. 22, no. 18, pp. 9077–9081, 2012.
- [11] K. Vasseur, K. Broch, A. L. Ayzner, B. P. Rand, D. Cheyng, C. Frank, F. Schreiber, M. F. Toney, L. Froyen, and P. Heremans, “Controlling the texture and crystallinity of evaporated lead phthalocyanine thin films for near-infrared sensitive solar cells,” *ACS Appl. Mater. Interfaces*, vol. 5, no. 17, pp. 8505–8515, 2013.
- [12] T. Sakurai, T. Ohashi, H. Kitazume, M. Kubota, T. Suemasu, and K. Akimoto, “Structural control of organic solar cells based on nonplanar metallophthalocyanine/C<sub>60</sub> heterojunctions using organic buffer layers,” *Org. Electron.*, vol. 12, no. 6, pp. 966–973, 2011.
- [13] J. Dai, X. Jiang, H. Wang, and D. Yan, “Organic photovoltaic cells with near infrared absorption spectrum,” *Appl. Phys. Lett.*, vol. 91, no. 25, a. 253503, 2007.
- [14] T. M. Kim, H. S. Shim, M. S. Choi, H. J. Kim, and J.- J. Kim, “Multilayer epitaxial growth of lead phthalocyanine and C<sub>70</sub> using CuBr as

- a templating layer for enhancing the efficiency of organic photovoltaic cells,” *ACS Appl. Mater. Interfaces*, vol. 6, no. 6, pp. 4286–4291, 2014.
- [15] K. Vasseur, B. P. Rand, D. Cheyons, L. Froyen, and P. Heremans, “Structural evolution of evaporated lead phthalocyanine thin films for near-infrared sensitive solar cells,” *Chem. Mater.*, vol. 23, no. 3, pp. 886–895, 2011.
- [16] B. Bernardo, D. Cheyons, B. Verreet, R. D. Schaller, B. P. Rand, and N. C. Giebink, “Delocalization and dielectric screening of charge transfer states in organic photovoltaic cells,” *Nat. Commun.*, vol. 5, a. 3245, 2014.
- [17] K. Vandewal, K. Tvingstedt, A. Gadisa, O. Ingänas, and J. V. Manca, “On the origin of the open-circuit voltage of polymer-fullerene solar cells,” *Nat. Mater.*, vol. 8, no. 11, pp. 904–909, 2009.
- [18] S. Gélinas, A. Rao, A. Kumar, S. L. Smith, A. W. Chin, J. Clark, T. S. van der Poll, G. C. Bazan, and R. H. Friend, “Ultrafast long-range charge separation in organic semiconductor photovoltaic diodes,” *Science*, vol. 343, no. 6170, pp. 512–516, 2014.
- [19] D. Veldman, S. C. J. Meskers, and R. A. J. Janssen, “The energy of charge-transfer states in electron donor-acceptor blends: Insight into the energy losses in organic solar cells,” *Adv. Funct. Mater.*, vol. 19, no. 12, pp. 1939–1948, 2009.
- [20] V. Shrotriya, G. Li, Y. Yao, T. Moriarty, K. Emery, and Y. Yang, “Accurate measurement and characterization of organic solar cells,” *Adv. Funct. Mater.*, vol. 16, no. 15, pp. 2016–2023, 2006.

- [21] P. Peumans, A. Yakimov, and S. R. Forrest, "Small molecular weight organic thin-film photodetectors and solar cells," *J. Appl. Phys.*, vol. 93, no. 7, pp. 3693–3723, 2003.
- [22] F. Zinna, M. Pasini, F. Galeotti, C. Botta, L. Di Bari, and U. Giovannela, "Design of lanthanide-based OLEDs with remarkable circularly polarized electroluminescence," *Adv. Funct. Mater.*, vol. 27, no. 1, a. 1603719, 2017.
- [23] R. Singh, K. N. N. Unni, A. Solanki, and Deepak, "Improving the contrast ratio of OLED displays: an analysis of various techniques," *Opt Mater*, vol. 34, no. 4, pp. 716–723, 2012.
- [24] K. Celebi, T. D. Heidel, and M. A. Baldo, "Simplified calculation of dipole energy transport in a multilayer stack using dyadic Green's functions," *Opt. Express*, vol. 15, no. 4, pp. 1762–1772, 2007.
- [25] R. Meerheim, M. Furno, S. Hofmann, B. Lussem, and K. Leo, "Quantification of energy loss mechanisms in organic light-emitting diodes," *Appl. Phys. Lett.*, vol. 97, no. 25, a. 253305, 2010.
- [26] X. Yin, M. Schäferling, B. Metzger, and H. Giessen, "Interpreting chiral nanophotonic spectra: the plasmonic Born–Kuhn model," *Nano Lett.*, vol. 13, no. 12, pp. 6238–6243, 2013.
- [27] N. Berova, L. D. Bari, and G. Pescitelli, "Application of electronic circular dichroism in configurational and conformational analysis of organic compounds," *Chem. Soc. Rev.*, vol. 36, no. 6, pp. 914–931, 2007.
- [28] A. D. Rakic, "Algorithm for the determination of intrinsic optical constants of metal-films - application to aluminum," *Appl Optics*, vol. 34, no. 22, pp. 4755–4767, 1995.

- [29] K. Kang, Y. Lee, J. Kim, H. Lee, and B. Yang, “A generalized Fabry–Pérot formulation for optical modeling of organic light-emitting diodes considering the dipole orientation and light polarization,” *IEEE Photonics Journal*, vol. 8, no. 2, a. 1600519, 2016.
- [30] F. J. Rodriguez-Fortuno, G. Marino, P. Ginzburg, D. O’Connor, A. Martinez, G. A. Wurtz, and A. V. Zayats, “Near-field interference for the unidirectional excitation of electromagnetic guided modes,” *Science*, vol. 340, no. 6130, pp. 328–330, 2013.
- [31] R. Hussain, D. Keene, N. Noginova, and M. Durach, “Spontaneous emission of electric and magnetic dipoles in the vicinity of thin and thick metal,” *Opt. Express*, vol. 22, no. 7, pp. 7744–7755, 2014.

## Chapter 3

# Three Dimensional Nanophotonic Engineering for Organic Optoelectronics

### 3.1 Introduction

In this chapter, I demonstrate a promising nanophotonic platform consisting of a dielectric sandwiched between a chirally patterned metal layer and a flat metal layer (chiral MDM), where a plasmonic hotspot with very high photonic density of states is formed in the dielectric region. A key advantage of this is the independent engineering of the photoactive layer mainly determining the external quantum efficiency and of the agent of inducing the circular dichroic response, which leads to overcoming the tradeoff between the external quantum efficiency and the dissymmetry factor. This is in contrast to chiral molecules generally suffered from the tradeoff, limiting their practicality. First, I investigate the electromagnetic features and the origin of the circular dichroic plasmon modes of the chiral MDM structure. Next, I apply the chiral

MDM structure as a nanophotonic platform for circular-polarization-sensitive organic photodetectors (CP-OPD) and then I establish their design principles.

## 3.2 Chiral Cavity Structure for Inducing Circular Dichroic Plasmons

### 3.2.1 Limits of Chiral Molecular Optoelectronics

Chiroptical effects, including circular dichroism [1], circular birefringence [1], or circular conversion dichroism [2], originate from dissymmetric electromagnetic responses of chiral objects to the polarization state of circularly polarized light (CPL). Various applications of the chiroptical effects, such as chiral molecular sensing [3], holography [4], nanorobotics [5], and detectors [6] and emitters[7] of CPL, have attracted increasing attention. To further increase the practicality of the chiroptical applications, it is essential to rationally control the shape and configuration of the chiral objects, such as chiral molecules, helically aggregated molecules, and chiral plasmonic structures [8, 9, 10]. For example, chiral objects configured to possess mutually parallel electric and magnetic dipole moments oscillating in-phase can resonantly absorb or emit CPL [9, 11].

Chiroptical effects arising from chiral molecules are often limited by a mismatch between the molecular size and the wavelength ( $\lambda$ ) of CPL [10]. One way to overcome this is to use a superchiral field that appears at the node of a standing wave [10]. This greatly improves the CPL dissymmetry factor ( $g_A$ ) defined as

$$g_A = 2 \frac{\eta_A^l - \eta_A^r}{\eta_A^l + \eta_A^r}, \quad (3.1)$$

where  $\eta_A$  is the absorption efficiency of molecules and the  $l$  and  $r$  superscripts

correspond to the illumination of left- and right-handed circularly polarized light (*l*-CPL and *r*-CPL), respectively. However, because the field intensity is very weak at the node, this method is not suitable for applications where high  $\eta_A$  is desired. Alternatively, one can utilize a chiral supramolecular assembly of chiral molecules [12] or achiral molecules with chirality-inducing additives [13]. This approach can increase  $g_A$  without necessarily decreasing  $\eta_A$ , but is difficult to apply to thin-film chiral optoelectronic devices whose thicknesses are comparable to or even smaller than the wavelength.

Chiral plasmonic nanostructures can amplify the chiroptical effects of chiral molecules, or even induce those effects from achiral molecules [14], which can be tuned by controlling their geometries. Because they can also function as electrodes [8, 15], they are promising platforms for chiral optoelectronic devices. In particular, a chiral MDM structure is known to selectively excite a plasmonic hotspot, where the electromagnetic field is strongly localized, depending on the helicity of CPL [15, 16, 17]. A previous study of the chiral MDM structure has demonstrated circular dichroism originating from plasmonic loss, which has been utilized for a chiral photodetector based on a metal–semiconductor junction [15]. However, this type of photodetector operating via inefficient thermionic emission is inherently inferior compared to a device based on a semiconductor–semiconductor junction.

Here, I numerically analyze photonic properties of the chiral MDM structure with the feature that plasmonic hotspots are selectively excited by CPL incidence, and explore its possibility as nanophotonic platforms to improve circular dichroism as well as optical density. I design a chiral MDM structure, the top electrode of which has windmill (or gammadion)-shaped nanopattern. For a circular polarization, the helicity of which is matched with the twisted direction of the chiral nanopattern, the EM energy of the incident wave is

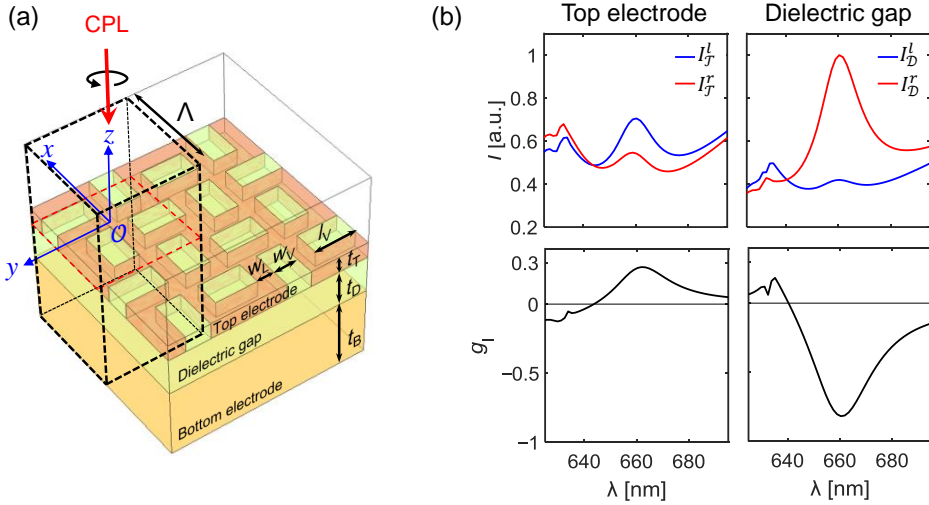


Figure 3.1 (a) Schematic of the simulation geometry of the chiral MDM structure investigated in this study. (b) The volume average of  $|\tilde{\mathbf{E}}|^2$  in the top electrode (top left) and the dielectric gap (top right) under  $r$ -CPL (red) and  $l$ -CPL (blue) illumination. Also shown are the associated dissymmetry factors in the top electrode (bottom left) and the dielectric gap (bottom right).

effectively transferred to plasmonic hotspot arising in the gap region whereas for the opposite circular polarization the energy is dissipated to heat in the top electrode. The excitation of plasmonic hotspots is interpreted from the view point of mode hybridization between SPP waves at the top and bottom electrodes under the condition that the momentum matching is satisfied.

### 3.2.2 Simulation Geometry

Figure 3.1(a) shows a chiral MDM structure consisting of a subwavelength-thick dielectric layer sandwiched between top and bottom electrodes, where the top electrode is perforated in a shape of periodically arranged windmills. The region enclosed by the black dashed lines represents a unit cell, with width  $\Lambda$  in the  $x$  and  $y$  directions, possessing a four-fold rotational symmetry, and

the origin ( $\mathcal{O}$ ) of the coordinate system is at the center of the square indicated by the red dashed lines. The thicknesses of the top electrode, the bottom electrode, and the dielectric gap are denoted by  $t_T$ ,  $t_B$ , and  $t_D$ , respectively. The length and the width of the voids are denoted by  $l_V$  and  $w_V$ , respectively, and the line width of the metal pattern is indicated by  $w_L$ . Because the thickness of the transparent uppermost layer representing a glass substrate is typically much larger than the wavelength of CPL propagating in the  $-\hat{z}$  direction [Fig. 3.1(a), red arrow], it is set to be infinite. Organic molecules are chosen as the dielectric material because of the following reasons: large absorption coefficient ( $\alpha$ ) allows for sufficient light absorption in the subwavelength-thick layer; the direction of the transition dipole moment of molecules can be controlled [18, 10], which is advantageous to fully optimize the chiral light–matter interactions [10]. In Section 3.1, where chiral plasmonic resonances of the chiral MDM structure are investigated, the relative permittivity ( $\varepsilon_r$ ) of the dielectric layer is assumed to be 3.24, a typical value for organic semiconductors [19]. In Section 3.2, the dielectric layer is described by the complex relative permittivity tensor ( $\bar{\bar{\varepsilon}}_r$ ) to reflect the anisotropic and absorptive characteristics of the constituent molecules. The top and bottom electrodes are composed of silver because it is known to form efficient charge injection and extraction electrodes upon employing appropriate interfacial layers [20] and to have low optical loss [21]. The wavelength-dependent  $\varepsilon_r$  values of silver are taken from the literature [22], and the  $\varepsilon_r$  values of the voids and the glass substrate are assumed to be 3.24 and 2.25, respectively, at all wavelengths. All materials are assumed to be nonmagnetic and homogeneous. For all calculations, COMSOL Multiphysics software, a finite element modeling tool, is used.

### 3.2.3 Circular Dichroic Plasmons in the Chiral Cavity Structure

Figure 3.1(b) shows the volume average of  $|\tilde{\mathbf{E}}|^2$  calculated using the following equation:

$$I_{\mathcal{V}}^{\sigma} = \frac{\int_{\mathcal{V}} |\tilde{\mathbf{E}}|^2 dV}{\int_{\mathcal{V}} dV}, \quad (3.2)$$

for CPL impinging upon the chiral MDM structure with  $t_{\text{D}} = 80$  nm,  $t_{\text{T}} = 50$  nm,  $t_{\text{B}} = 200$  nm,  $\Lambda = 423$  nm,  $w_{\text{L}} = 73$  nm,  $w_{\text{V}} = 104$  nm, and  $l_{\text{V}} = 175$  nm. Here,  $\tilde{\mathbf{E}}$  is the complex amplitude of the electric field ( $\mathbf{E}$ ),  $\mathcal{V}$  is either the top electrode ( $\mathcal{T}$ ) or the dielectric layer ( $\mathcal{D}$ ) in a unit cell, and  $\sigma$  is the helicity of the CPL, where  $\sigma = r$  (or  $l$ ) corresponds to  $r$ -CPL (or  $l$ -CPL) whose  $\mathbf{E}$  in the  $xy$  plane rotates in the counterclockwise (or clockwise) direction when viewed from above. Notable is that the resonant feature at  $\lambda = 660$  nm strongly depends on  $\sigma$  and  $\mathcal{V}$ :  $I_{\mathcal{T}}^l$  is larger than  $I_{\mathcal{T}}^r$  (left panel), whereas  $I_{\mathcal{D}}^r$  is larger than  $I_{\mathcal{D}}^l$  (right panel). The dissymmetric optical response is quantified by the dissymmetry factor of  $I_{\mathcal{V}}$ , defined as

$$g_{\text{I}} = 2 \frac{I_{\mathcal{V}}^l - I_{\mathcal{V}}^r}{I_{\mathcal{V}}^l + I_{\mathcal{V}}^r}. \quad (3.3)$$

The highest value of  $|g_{\text{I}}|$  is found to be 0.8 at  $\lambda = 660$  nm when  $\mathcal{V} = \mathcal{D}$  [Fig. 3.1(b), bottom right], indicating that this type of chiral MDM structure with photoactive molecules positioned in the dielectric gap is a promising architecture for CP-OPDs.

To understand the characteristics of the electromagnetic resonance arising at  $\lambda = 660$  nm, I investigate the electromagnetic field distributions in the chiral MDM structure. Figures 3.2(a) and 3.2(b) are the  $|\tilde{E}_z|^2$  and  $|\tilde{E}_{xy}|^2$  ( $= |\tilde{E}_x|^2 + |\tilde{E}_y|^2$ ) profiles in the  $yz$ -plane at  $x = \Lambda/2$ , and Figs. 3.2(c) and 3.2(d) are the  $|\tilde{E}_z|^2$  and  $|\tilde{H}_{xy}|^2$  ( $= |\tilde{H}_x|^2 + |\tilde{H}_y|^2$ ) profiles in the  $xy$ -plane at  $z =$

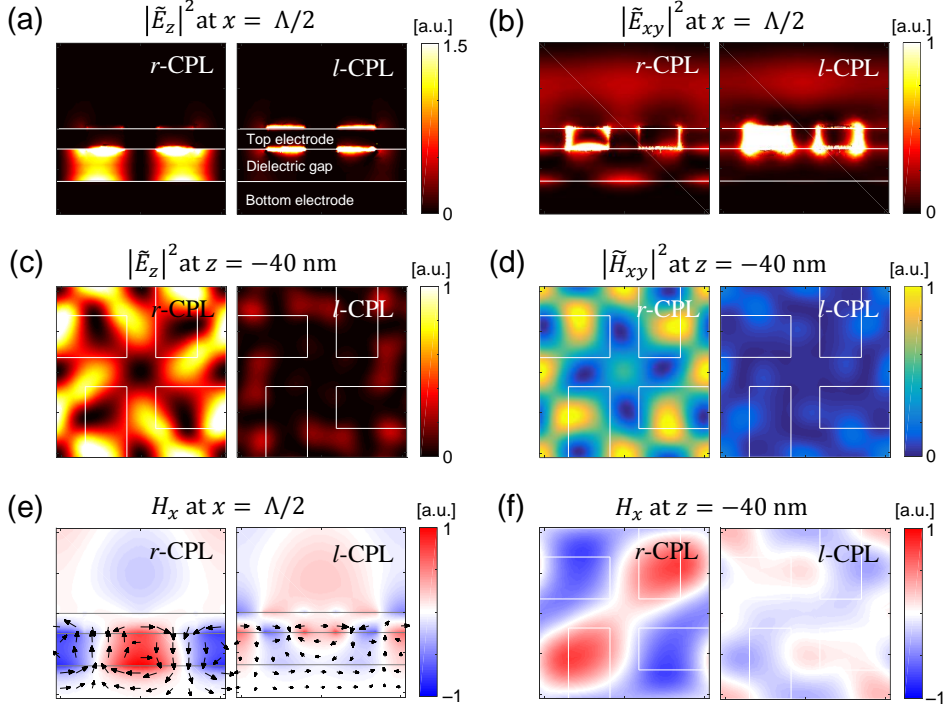


Figure 3.2 (a)  $|\tilde{E}_z|^2$  profiles at  $x = \Lambda/2$ . (b)  $|\tilde{E}_{xy}|^2$  profiles at  $x = \Lambda/2$ . (c)  $|\tilde{E}_z|^2$  profiles at  $z = -40$  nm (the midpoint on the  $z$ -axis in the dielectric layer). (d)  $|\tilde{H}_{xy}|^2$  profiles at  $z = -40$  nm. (e)  $H_x$  profiles at  $x = \Lambda/2$ . (f)  $H_x$  profiles at  $z = -40$  nm. The arrows in (e) represent the induced current density. The left and right panels in (a)–(f) correspond to the cases of *r*-CPL and *l*-CPL illumination, respectively.

$-40$  nm (the midpoint on the  $z$ -axis in the dielectric gap), respectively.  $\tilde{E}_i$  (or  $\tilde{H}_i$ ) is the complex amplitude of the  $i$  component of the  $\mathbf{E}$  [or magnetic ( $\mathbf{H}$ )] field. In each figure, the left and right profiles correspond to the cases of  $r$ -CPL and  $l$ -CPL illumination, respectively. In the case of  $r$ -CPL the electromagnetic field is localized in the dielectric gap, whereas in the case of  $l$ -CPL it is localized around the top electrode.  $H_x(\Lambda/2, y, z)$  and the induced current density ( $J$ , arrows) at time  $\tau_H$  when  $|H_x|$  is maximized are plotted in Fig. 3.2(e), where the length of the arrows is proportional to  $\log J$ . For the  $r$ -CPL, current loops are observed across the top and bottom electrodes, indicating that the plasmonic hotspots formed in the dielectric gap are attributed to a magnetic resonance. When the  $\mathbf{k}$  vector of the incident CPL is tilted in the  $yz$  plane, the resonance frequency varies linearly with the angle of incidence (Fig. 3.3), implying that the resonance is excited by grating-coupled SPPs with the aid of the reciprocal lattice vector of the periodic chiral grating ( $\mathbf{k} = \frac{2m\pi}{\Lambda}\hat{\mathbf{x}} + \frac{2n\pi}{\Lambda}\hat{\mathbf{y}}$ , where  $m$  and  $n$  are integers) [23, 24]. In addition, the  $H_x$  profiles at  $z = -40$  nm [Fig. 3.2(f)], where four anti-nodes are observed in the case of  $r$ -CPL, indicate that  $m = n = 1$  [24].

### 3.2.4 Hybridization of Surface Plasmon Polaritons

To further investigate the grating-coupled SPPs,  $|\tilde{\mathbf{E}}|^2$  averaged over a plane normal to the  $z$ -axis within a unit cell is plotted as a function of  $t_D$  and  $\lambda$  (Fig. 3.4). The  $z$ -position of the plane is chosen to be at the interface between the dielectric and the bottom electrode ( $z = -t_D$ ) to better identify the wavelengths of the magnetic resonance by reducing the background originating from the non-resonantly coupled electromagnetic field localized around the top electrode. In the case of  $r$ -CPL [Fig. 3.4(a)], when  $t_D > 200$  nm the branch denoted by  $\text{SPP}_D$  is observed at  $\lambda \approx 610$  nm, which, as  $t_D$  decreases below

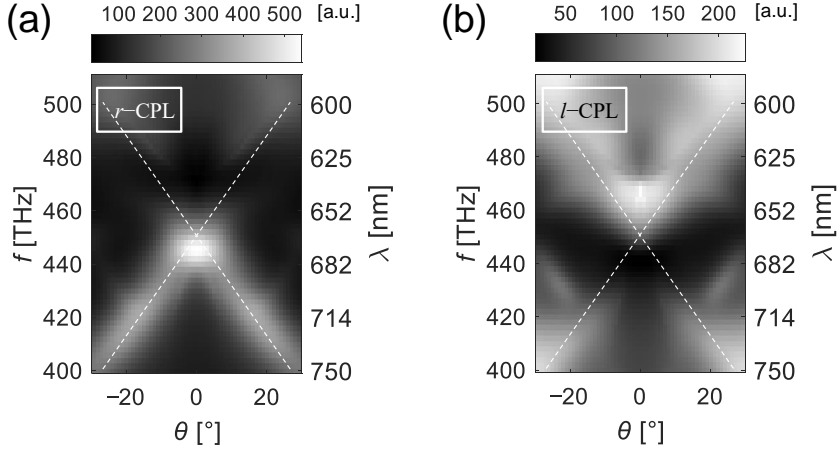


Figure 3.3 Optical power absorbed in the bottom electrode as a function of the frequency  $f$  (or wavelength  $\lambda$ ) and the incident angle  $\theta$  under (a)  $r$ -CPL and (b)  $l$ -CPL illumination. The  $\mathbf{k}$  vector is in the  $yz$ -plane and  $\theta$  is the angle between  $\mathbf{k}$  and  $-\hat{\mathbf{z}}$ . The linear dependence of the resonance frequency on  $\theta$  (dashed lines) indicates that the resonance features originate from the grating-coupled SPPs.

200 nm, splits into the red- and blue-shifted branches, indicated by  $\text{SPP}_R$  and  $\text{SPP}_B$ , respectively. In the  $l$ -CPL case [Fig. 3.3(b)], the resonance features in the region with  $t_D > 200$  nm are almost identical to those in the  $r$ -CPL case in the same region, but the  $\text{SPP}_R$  branch is absent. Next, I investigate the  $E_z$  profile corresponding to a representative point on each branch: point A ( $\lambda = 612$  nm,  $t_D = 240$  nm) where the  $\text{SPP}_D$  branch begins to separate, point B ( $\lambda = 660$  nm,  $t_D = 80$  nm) on the  $\text{SPP}_R$  branch where the maximum  $|g_I|$  (Fig. 3.1) is observed, and point C ( $\lambda = 570$  nm,  $t_D = 140$  nm) on the  $\text{SPP}_B$  branch. Figures 3.5(a) and 3.5(b) show the  $E_z(\Lambda/2, y, z)$  profiles at point A, captured at time  $\tau_E$  when  $|E_z|$  is maximized and at  $\tau_E + T/4$ , where  $T$  is the period of the electromagnetic wave, respectively. These two profiles exhibit the characteristics of bonding and antibonding modes, respectively, suggesting that they result from the hybridization of the SPPs propagating along the

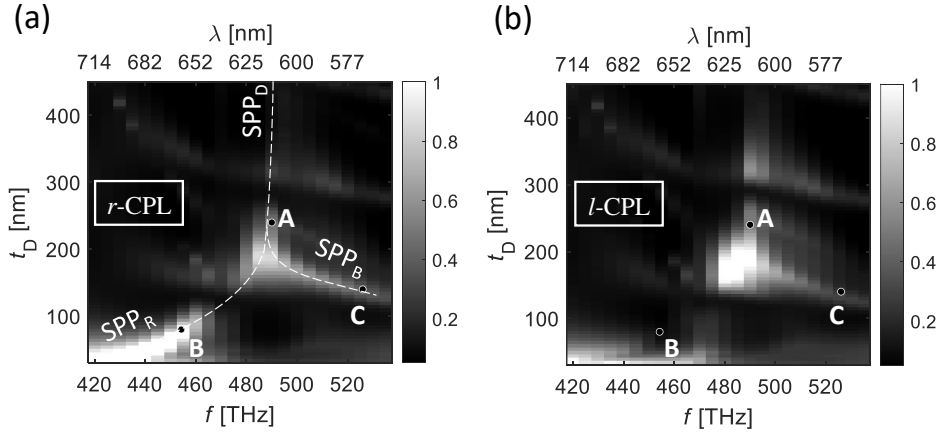


Figure 3.4 Surface average of  $|\tilde{\mathbf{E}}|^2$  at the dielectric–bottom metal interface ( $z = -t_D$ ) as a function of the thickness of the dielectric layer  $t_D$  and the wavelength  $\lambda$  (or frequency  $f$ ) of the incident  $r$ -CPL (a) and  $l$ -CPL (b). The dotted lines in (a) are a guide to the eye, drawn to better identify the resonance conditions.

metal–dielectric interfaces at  $z = 0$  nm and  $-t_D$  [25]. For the bonding case, the polarity of  $E_z$  is maintained along the  $z$ -axis in the dielectric region, whereas for the antibonding case, there exists a horizontal plane with  $E_z = 0$  at which the polarity is reversed [25]. Furthermore, when  $t_D$  is large ( $> 200$  nm), these two modes are degenerate. When  $t_D$  decreases below 200 nm, the features of the antibonding (or bonding) mode are observed only in the  $SPP_B$  (or  $SPP_R$ ) branch, as shown in Figs. 3.5(c) and 3.5(d). Interestingly, unlike in the case of the  $SPP_B$  branch [Fig. 3.5(d)], the field distribution of the  $SPP_R$  branch [Fig. 3.5(c)] strongly depends on the helicity of CPL, resulting in large  $|g_I|$  in the dielectric gap [Fig. 3.1(b)]. It is this characteristic of the chiral MDM structure that I exploit in the design of CP-OPDs having both high  $g_A$  and  $\eta_A$ . The two slightly tilted horizontal features with low intensities in Fig. 3.4 originate from Fabry–Perot resonances, where the total reflection from the chiral MDM structure significantly increases (data not shown).

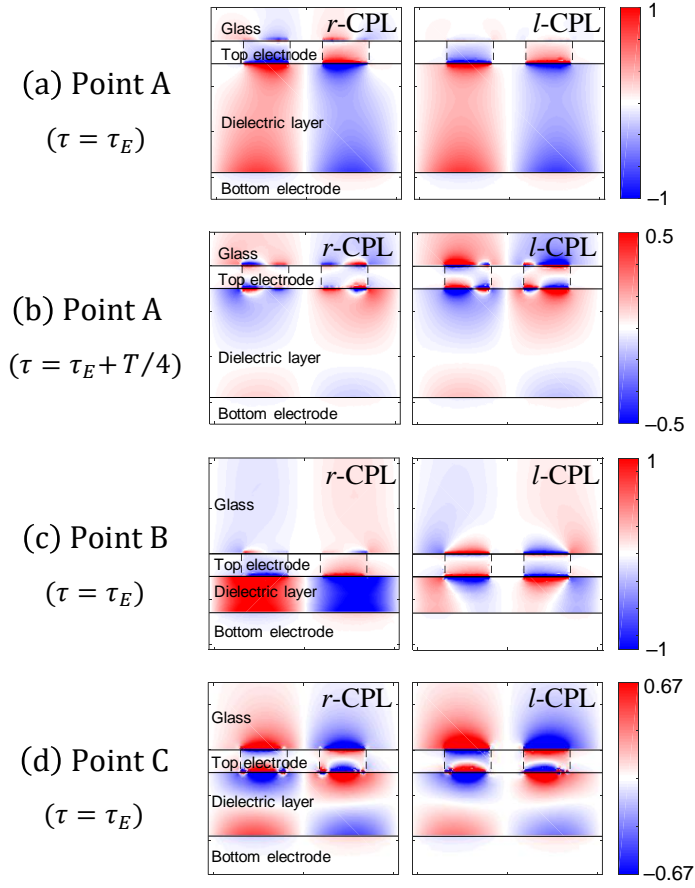


Figure 3.5  $E_z$  profiles in the  $yz$  plane at  $x = \Lambda/2$  corresponding to point A (a,b), point B (c), and point C (d). The profiles in (a, c, d) are captured when  $|E_z|$  is maximized ( $\tau = \tau_E$ ), while the profile in (b) is captured at  $\tau = \tau_E + T/4$ . The left and right plots in each figure correspond to the cases of  $r$ -CPL and  $l$ -CPL illumination, respectively.

### 3.2.5 Light–Matter Interactions in the Chiral Cavity

In this section, the effects of inherent molecular chirality ( $g_0$ ) in vacuum on  $\eta_A$  and  $g_A$  will be discussed for the case that chiral molecules with  $|g_0| > 0$  are located at  $z = -40$  nm (the midpoint on the  $z$ -axis in the dielectric layer). It is assumed that the dielectric is homogeneous, isotropic, nonmagnetic, and lossless, and that its electromagnetic response is perturbed by a very thin molecular layer. First, the value of  $\eta_A$  at  $z = -40$  nm is calculated using eq 1.8, and then the dissymmetry factor ( $g_{CC}$ ) is obtained using the following equation:

$$g_{CC} = 2 \frac{\eta_{A,CC}^l - \eta_{A,CC}^r}{\eta_{A,CC}^l + \eta_{A,CC}^r}, \quad (3.4)$$

where the subscript CC means that chiral molecules are located inside the cavity. Equation 3.4 can be expressed as a function of  $g_0 (= -\frac{4G''}{c\alpha''})$  as follows:

$$g_{CC}(g_0) = 2 \frac{\omega(|\mathbf{E}^l|^2 - |\mathbf{E}^r|^2) + \frac{cg_0}{\varepsilon_0}(C^l - C^r)}{\omega(|\mathbf{E}^l|^2 + |\mathbf{E}^r|^2) + \frac{cg_0}{\varepsilon_0}(C^l + C^r)}, \quad (3.5)$$

where  $\alpha''$  and  $G''$  are the imaginary parts of the electric polarizability and electro-magnetic dipole polarizability, respectively, and  $C$  is the optical chirality, discussed in the *Sec.* 1.1.3. Figure 3.6(a) shows  $\Delta g_{CC0} (= |g_{CC}(g_0)| - |g_0|)$ , which quantifies how much the use of the chiral cavity leads to the increase in the dissymmetry factor of absorption by chiral molecules. Figure 3.6(b) shows  $\Delta g_{CCA} (= |g_{CC}(g_0)| - |g_{CA}|)$ , which quantifies how much the use of the chiral molecules in the chiral cavity leads to the gain of the dissymmetry factor as compared to the case using achiral molecules, where the subscript CA indicates that achiral molecules are located inside the chiral cavity, i.e.,  $g_{CA} = g_{CC}(g_0 = 0)$ . In Fig 3.6(a) [or Fig. 3.6(b)], the positive value indicates that the use of the chiral cavity (or the use of chiral molecules) leads to the gain of

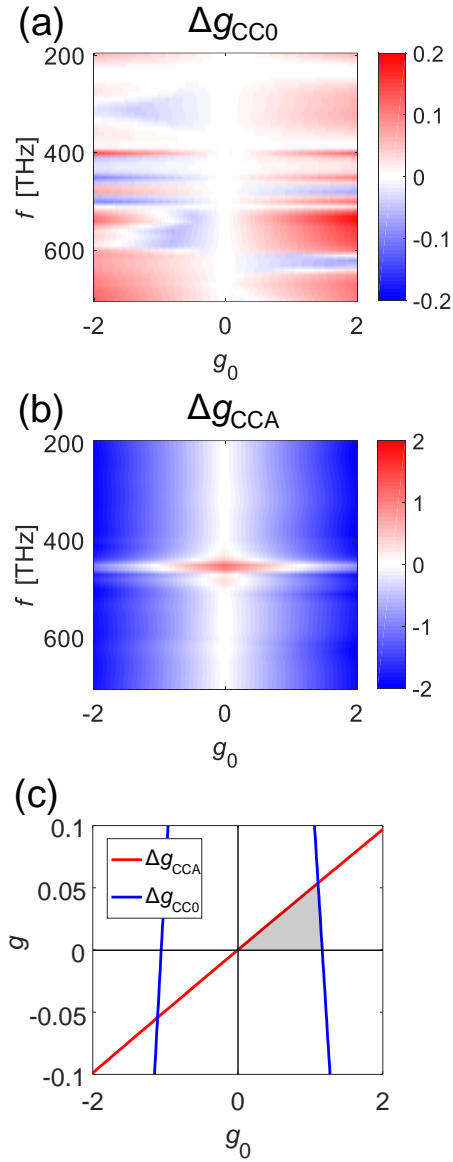


Figure 3.6 (a) Difference in the dissymmetry factor between the chiral molecules in the chiral cavity and the chiral molecules in the vacuum ( $\Delta g_{CC0}$ ). (b) Difference in the dissymmetry factor between the chiral molecules in the chiral cavity and the achiral molecules in the chiral cavity ( $\Delta g_{CCA}$ ). (c) Line cuts of the  $\Delta g_{CC0}$  (blue) and  $\Delta g_{CCA}$  (red) spectra along  $f = 454$  THz, respectively.

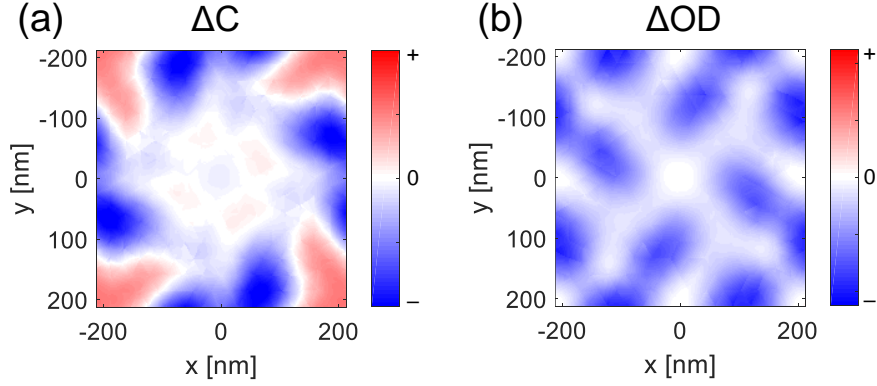


Figure 3.7 (a) Difference in the optical chirality ( $\Delta C = C^l - C^r$ ) at  $z = -t_D/2$ . (b) Difference in the square of the electric field intensity ( $\Delta |\mathbf{E}|^2 = |\mathbf{E}^l|^2 - |\mathbf{E}^r|^2$ ) at  $z = -t_D/2$ .

the dissymmetry factor. The red and blue lines in Fig. 3.6(c) are the linecuts at  $f = 454$  THz in Figs. 3.6(a) and 3.6(b), respectively. The shaded region in Fig. 3.6(c), where both  $\Delta g_{CCA}$  and  $\Delta g_{CC0}$  are larger than zero, corresponds to the desirable values of  $g_0$  in terms of the dissymmetry factor of absorption in the chiral cavity.

Next, I investigated which of the increase in  $g_0$  and the control of the dipole orientation increases the dissymmetry factor more effectively. Substituting Eq. (1.1) and the following relative permittivity tensor ( $\bar{\bar{\epsilon}}_r$ ),

$$\bar{\bar{\epsilon}}_r = \begin{bmatrix} \tilde{\epsilon}_x & 0 & 0 \\ 0 & \tilde{\epsilon}_y & 0 \\ 0 & 0 & \tilde{\epsilon}_z \end{bmatrix}, \quad (3.6)$$

into Eq. (1.3) yields

$$\eta_{CA}^{l/r} = \frac{\omega}{2} (\alpha_x'' |\tilde{\mathbf{E}}_x^{l/r}|^2 + \alpha_y'' |\tilde{\mathbf{E}}_y^{l/r}|^2 + \alpha_z'' |\tilde{\mathbf{E}}_z^{l/r}|^2). \quad (3.7)$$

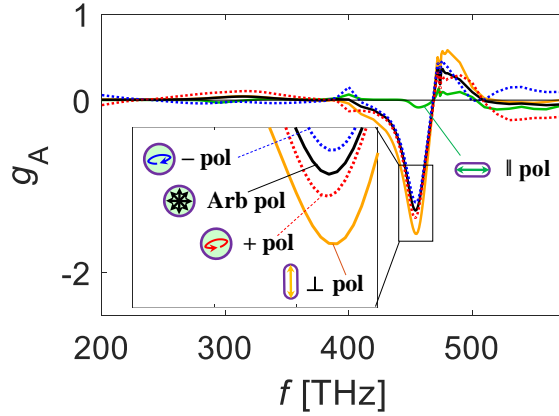


Figure 3.8 Dissymmetry factor of absorption by molecules in the chiral cavity with different molecular orientation and chirality. The black, orange, and green solid lines correspond to randomly-, vertically-, and horizontally-oriented anisotropic molecules, respectively. The blue and red dashed lines correspond to the isotropic chiral molecules with  $g_0 = 1.23$  and those with  $g_0 = -1.23$ , respectively.

Figure 3.8 shows the dissymmetry factor of absorption by the absorber located at  $z = -40$  nm (the midpoint on the  $z$  axis in the dielectric layer) for different molecular polarizability under CPL illumination with  $\lambda = 660$  nm. It is notable that the vertically oriented achiral molecules (orange) show larger value of  $g_A$  than the randomly (black) and horizontally (green) oriented achiral molecules and even than the chiral molecules (red and blue):  $|g_A|$  of the vertically oriented molecules is 1.55, which is larger than  $|g_A|$  of the chiral molecules with  $g_0 = 1.23$  by 14%. This is because the localized plasmon in the dielectric gap is mainly composed of the  $z$  component, that matches the vertical orientation of molecules as shown in Eq. (1.3). In addition, this chiral cavity structure is not desirable to maximize the difference in the optical chirality:  $\Delta C (= C^l - C^r)$  distribution is not spatially uniform [Fig. 3.7(a)], indicating that the  $g_0\Delta C$  in Eq. (3.5) will be cancelled out by spatial averaging in unit cell.

### 3.3 Circular-Polarization-Sensitive Organic Photodetectors using the Chiral Cavity

#### 3.3.1 Circularly Polarized Light Detectors

In recent years, photodetectors generating contrasting photocurrents in response to circularly polarized light (CPL) with opposite helicity have attracted attention [6, 26, 27, 28, 29, 15] due to their potential applications in spin information processing [30], quantum teleportation [31] and computation [32], and circular dichroism spectroscopy [33]. One rational approach to realizing a compact circular-polarization-sensitive photodetector that uses no bulky optical components is to replace the material constituting the photoactive layer in a conventional photodetector with chiral molecules possessing dissymmetric absorption depending on the helicity of the incident CPL. In this case, the dissymmetric photocurrent is determined by the dissymmetry in absorption quantified either by the circular dichroism value [11]:

$$\text{CD} = \eta_{\text{A}}^l - \eta_{\text{A}}^r, \quad (3.8)$$

or by the dissymmetry factor of absorption [11]:

$$g_{\text{A}} = 2 \frac{\eta_{\text{A}}^l - \eta_{\text{A}}^r}{\eta_{\text{A}}^l + \eta_{\text{A}}^r}, \quad (3.9)$$

where  $\eta_{\text{A}}$  is the absorption efficiency and the superscripts  $l$  and  $r$  denote the illumination of left- and right-handed circularly polarized light ( $l$ -CPL and  $r$ -CPL), respectively. Because the value of CD or  $g_{\text{A}}$  of chiral molecules is limited by the mismatch between the molecular size and the wavelength ( $\lambda$ ) of CPL [10], a supramolecular assembly of chiral molecules or that of achiral molecules with chirality-inducing additives [13] is often utilized to

amplify CD or  $g_A$ . For example, a photodetector based on supramolecular squaraine derivative–fullerene donor–acceptor heterojunction attained a peak  $|g_A|$  of 0.1 at  $\lambda = 545$  nm [26], which is relatively large compared to other circular-polarization-sensitive organic or organic–inorganic hybrid photodetectors [28, 29, 27]. However, this value is much smaller than that of the ideal case corresponding to the complete dissymmetry in absorption, i.e.,  $|g_A| = 2$ . Interestingly, a circular-polarization-sensitive phototransistor based on a helicene thin film demonstrated a much higher photocurrent dissymmetry factor of 1.6–1.8 than is expected from its CD value [6]. Its applicability, however, is limited by a low external quantum efficiency ( $\eta_E$ ) of 0.1 % and a slow response time of 6.2 ms attributed to the lateral thin-film transistor geometry.

Alternatively, one can modify a local electromagnetic environment in the photoactive region so that the dissymmetry in photocurrent is amplified beyond what is expected from the CD value or is induced even with a photoactive layer having no intrinsic chirality [14]. For example, a previous study demonstrated that depending on the helicity of incident CPL, the electromagnetic field intensity can be selectively enhanced near Z-shaped plasmonic structures, generating hot electrons injected into Si over a Schottky barrier [15]. A circular-polarization-sensitive photodetector based on this mechanism yielded a high  $g_A$  of 1.1 and a near-unity  $\eta_A$  at  $\lambda = 1340$  nm [15]. Although inherently very fast [34], hot electron injection has a disadvantage that a significant number of hot electrons are thermally relaxed before being injected [35, 36], resulting in a low  $\eta_E$  of 0.2 %. In addition, the dissymmetry factor of photocurrent is only  $\sim 70$  % of  $g_A$ , meaning that the device architecture was not fully optimized. To realize a high-performance circular-polarization-sensitive-photodetector, it is essential to develop a new optoelectronic platform that can induce high  $g_A$  while being compatible with photoactive materials suitable for high  $\eta_E$ .

Here, I numerically demonstrate that a circular-polarization-sensitive organic photodetector (CP-OPD) based on a chiral plasmonic nanostructure can achieve both high  $g_A$  and  $\eta_E$ . The chiral MDM structure, as discussed in the previous chapter, a plasmon mode featuring a high photonic density of states in the dielectric region is excited only for incident CPL with its helicity matched to the twisted direction of the chiral nanopattern. A key feature of my CP-OPD is that the circular dichroic response is almost decoupled with the engineering of the organic donor–acceptor photoactive layer required for a high internal quantum efficiency ( $\eta_I$ ). This is in contrast to previously demonstrated CPL detectors, in which chiral molecules function as both the absorber and the agent that distinguishes the helicity of CPL [6, 26, 28, 27].

### 3.3.2 Investigation of the Dependence of Chiroptical Responses on the Position and Orientation of Absorbers

When the dielectric gap is composed of an optical absorption layer sandwiched between two nonabsorbing layers facilitating charge transport and extraction, the chiral MDM structure can generate charge carriers in response to incident CPL. When a conventional organic photodetector having a planar multilayer structure is illuminated with a planewave with  $\mathbf{k} \parallel \hat{\mathbf{z}}$  (normal incidence), the  $\mathbf{E}$  profile, composed entirely of the  $xy$  component, has a local maximum at a distance of about a quarter wavelength from the back metal electrode [37, 38]. In contrast, in the case of the chiral MDM structure,  $\mathbf{E}$  inside the dielectric region is primarily composed of the  $z$  component, which is strongly concentrated at the metal–dielectric interfaces as shown in Fig. 3.2(a). Because of these different electromagnetic properties of the two types of structures, it is not appropriate to apply to the plasmonic CP-OPDs the approaches typically used for conventional OPDs to maximize the optical absorption, i.e., the

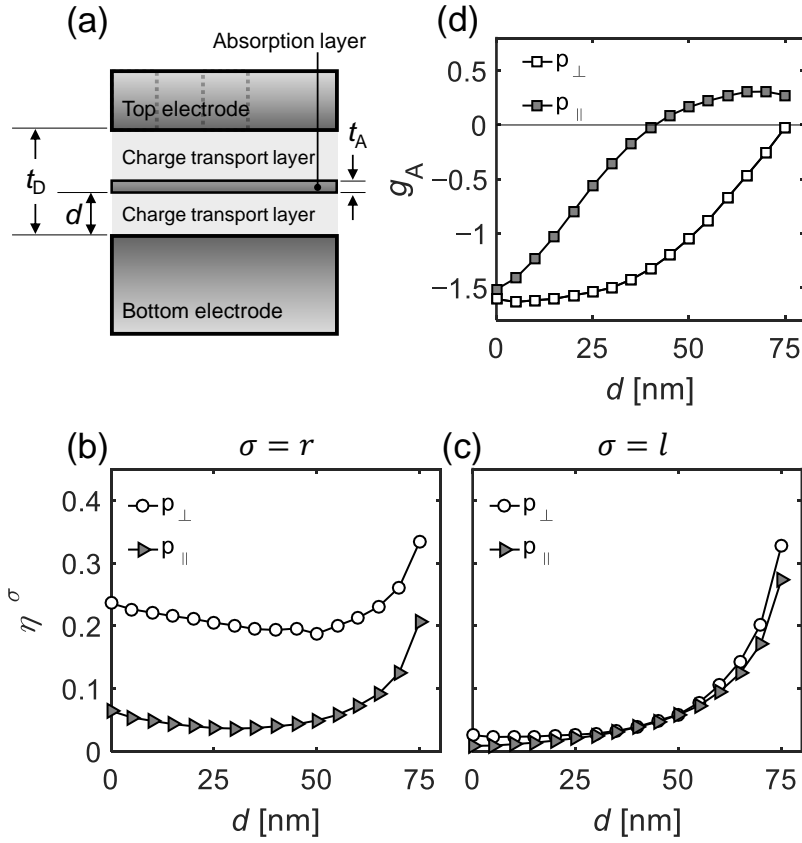


Figure 3.9 (a) Layer structure of the plasmonic CP-OPD. The absorption efficiencies of the CP-OPD with  $t_A = 5$  nm and  $\alpha = 1 \times 10^5$  cm $^{-1}$  as a function of  $d$  and the orientation of  $\mathbf{p}$  under  $r$ -CPL (b) and  $l$ -CPL (c) illumination. (d) The dissymmetry factor of absorption calculated from (b,c).

uses of an optical spacer [38] and molecules lying flat to the substrate [18]. Thus, to realize plasmonic CP-OPDs based on the chiral MDM structure that have both high  $\eta_A$  and  $g_A$ , a new design principle is needed. The structure of the plasmonic CP-OPD with  $t_D = 80$  nm is schematically illustrated in Fig. 3.9(a), where the thicknesses of the optical absorption layer and the lower charge transport layer are denoted by  $t_A$  and  $d$ , respectively. The anisotropic characteristic of the absorption layer is described by the complex permittivity tensor

$$\bar{\bar{\epsilon}}_r = \begin{bmatrix} \tilde{\epsilon}_x & 0 & 0 \\ 0 & \tilde{\epsilon}_y & 0 \\ 0 & 0 & \tilde{\epsilon}_z \end{bmatrix}, \quad (3.10)$$

where the diagonal components are set to make  $\alpha$  equal to  $1 \times 10^5$  cm<sup>-1</sup>—a value typical for organic films at absorption maxima—for an incident planewave with  $\mathbf{E}$  parallel to the transition dipole moment ( $\mathbf{p}$ ) of the absorbing molecule. For example, for a planewave with  $\lambda$ , the diagonal components are set as follows: (i) for  $\mathbf{p}$  perpendicular to the substrate (case  $p_\perp$ ),  $\text{Im}(\tilde{\epsilon}_x) = \text{Im}(\tilde{\epsilon}_y) = 0$  and  $\text{Im}(\tilde{\epsilon}_z) = -2n'n''$  ( $= -1.972$  when  $\lambda = 660$  nm), (ii) for  $\mathbf{p}$  parallel to the substrate (case  $p_\parallel$ ),  $\text{Im}(\tilde{\epsilon}_z) = 0$  and  $\text{Im}(\tilde{\epsilon}_x) = \text{Im}(\tilde{\epsilon}_y) = -\sqrt{2}n'n''$  ( $= -1.394$  when  $\lambda = 660$  nm), where  $n' \left( = \sqrt{3.24 + \left(\frac{\alpha\lambda}{4\pi}\right)^2} \right)$  and  $-n'' \left( = -\frac{\alpha\lambda}{4\pi} \right)$  are the real and imaginary parts of the complex refractive index ( $\tilde{n} = n' - in''$ ), respectively. The real part of  $\bar{\bar{\epsilon}}_r$  is assumed to be independent of  $\lambda$  and the orientation of  $\mathbf{p}$ :  $\text{Re}(\tilde{\epsilon}_x) = \text{Re}(\tilde{\epsilon}_y) = \text{Re}(\tilde{\epsilon}_z) = 3.24$ . To quantify the chiroptical performance of the plasmonic CP-OPD, I first calculate  $\eta_A^\sigma$ , the number of photons absorbed in the absorption layer divided by the number of incident

photons, as follows:

$$\eta_{\text{A}}^{\sigma} = -\frac{\omega\varepsilon_0}{2P_0} \int_{\mathcal{V}} \left\{ \text{Im}(\tilde{\varepsilon}_x)|\tilde{E}_x|^2 + \text{Im}(\tilde{\varepsilon}_y)|\tilde{E}_y|^2 + \text{Im}(\tilde{\varepsilon}_z)|\tilde{E}_z|^2 \right\} dV, \quad (3.11)$$

where  $P_0$  is the power of CPL incident on a unit cell,  $\varepsilon_0$  is the permittivity in vacuum,  $\omega$  is the angular frequency, and  $\mathcal{V}$  is the absorption layer in a unit cell. The value of  $g_{\text{A}}$  is then obtained from  $\eta_{\text{A}}^{\sigma}$  using Eq. (3.9).

The values of  $\eta_{\text{A}}^{\sigma}$  and  $g_{\text{A}}$  are calculated as functions of  $d$  and the orientation of  $\mathbf{p}$  for the CP-OPD with  $t_{\text{A}} = 5$  nm under  $r$ -CPL and  $l$ -CPL illumination at  $\lambda = 660$  nm [Figs. 3.9(b–d)]. For all values of  $d$ ,  $\eta_{\text{A}}^r$  is found to be larger in case  $p_{\perp}$  than in case  $p_{\parallel}$  [Fig. 3.9(b)]. The  $r$ -CPL illumination excites the plasmonic mode belonging to the  $\text{SPP}_{\text{R}}$  branch with  $\mathbf{E}$  composed primarily of  $E_z$  [Fig. 3.2(a)], and thus the molecules with  $\mathbf{p} \parallel \hat{\mathbf{z}}$  absorb more strongly than the molecules with  $\mathbf{p} \perp \hat{\mathbf{z}}$ . For both orientations,  $\eta_{\text{A}}^r$  has local maxima at  $d = 0$  and 75 nm because  $|\tilde{E}_z|^2$  (or  $|\tilde{E}_{xy}|^2$ ) in case  $p_{\perp}$  (or  $p_{\parallel}$ ) is concentrated at the top and bottom metal–dielectric interfaces as shown in Figs. 3.2(a) and 3.2(b). Unlike  $\eta_{\text{A}}^r$ ,  $\eta_{\text{A}}^l$  is almost identical for both orientations [Fig. 3.9(c)], where  $\eta_{\text{A}}^l$  is close to zero at  $d = 0$  and monotonically increases with  $d$ , except for an initial slight decrease for  $p_{\perp}$  case. This result is a direct consequence of the field profile,  $|\tilde{E}_z|^2$  for case  $p_{\perp}$  and  $|\tilde{E}_{xy}|^2$  for case  $p_{\parallel}$ , which concentrates at the top metal–dielectric interface and rapidly decreases away from it, as shown in the right panels of Figs. 3.2(a) and 3.2(b). The highest  $|g_{\text{A}}|$  is found to be 1.51 at  $d = 0$  nm for case  $p_{\parallel}$  and 1.63 at  $d = 5$  nm for case  $p_{\perp}$  [Fig. 3.9(d)]. Although these two values are comparable,  $\eta_{\text{A}}^r$ , which is the relevant absorption efficiency in this study because the twisted direction of the chiral MDM structure [Fig. 3.1(a)] is designed to resonantly match  $r$ -CPL, is much higher in case  $p_{\perp}$  than in case  $p_{\parallel}$ . Therefore, to achieve both high  $|g_{\text{A}}|$  and  $\eta_{\text{A}}$ , the absorption layer must be composed of molecules with  $\mathbf{p} \parallel \hat{\mathbf{z}}$  and be positioned

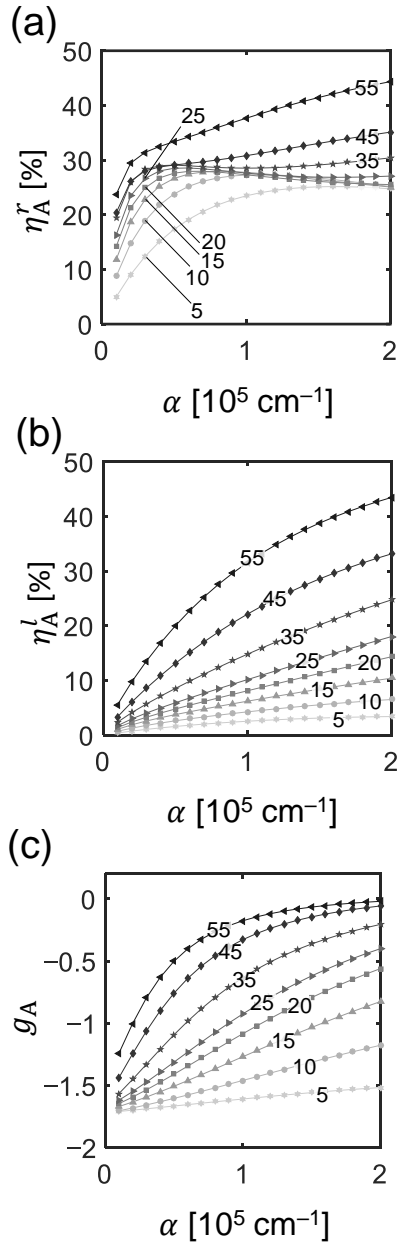


Figure 3.10 The absorption efficiencies for case  $p_{\perp}$  as a function of  $\alpha$  and  $t_A$  under  $r$ -CPL (a) and  $l$ -CPL (b) illumination. (c) The dissymmetry factor calculated from (e,f). The value of  $t_A$  (in nm) is shown for each line.

close to the bottom electrode.

### 3.3.3 Optimization of Circularly Polarized Light Dissymmetry Value

To further optimize the performance of the CP-OPD, I investigate the dependence of  $\eta_A$  and  $g_A$  on  $\alpha$  and  $t_A$  for case  $p_{\perp}$ . The thickness of the lower charge transport layer ( $d = 10$  nm) is chosen to be as small as possible to maximize  $g_A$  [Fig. 3.9(d)], and at the same time to be large enough to prevent exciton quenching by the bottom electrode [38, 39]. Figures 3.10(a) and 3.10(b) show  $\eta_A^r(\alpha)$  and  $\eta_A^l(\alpha)$ , respectively, calculated for different  $t_A$ , from which  $g_A(\alpha)$ , shown in Fig. 3.10(c), is calculated using Eq. (3.9). The dependence of  $\eta_A^r$  on  $\alpha$  and  $t_A$  is somewhat complex: an increase of  $\alpha$  (or  $t_A$ ) does not always result in a gain in  $\eta_A^r$ , and for  $t_A \leq 40$  nm, local maxima ranging from 25.2 to 29.4 % exist.  $\eta_A^l$ , on the other hand, increases monotonically with  $\alpha$  for all  $t_A$ . In the case of  $\eta_A^r$ , the increase in  $\alpha$  of the absorbing molecules, which are located in the high-field region, decreases the volume average of  $|\tilde{E}_z|^2$  in the absorption layer, as shown in Figs. 3.11(a) and 3.11(c). This tradeoff between  $|\tilde{E}_z|^2$  and  $\alpha$  leads to the presence of local maxima of  $\eta_A^r$ . In the case of  $\eta_A^l$ , on the other hand, the absorbers are excited by the tail of the SPP wave localized at the top metal–dielectric interface. As a result, the effect of  $\alpha$  on  $|\tilde{E}_z|^2$  is much weaker compared to the case of  $\eta_A^r$  [Figs. 3.11(b) and 3.11(d)], and hence  $\eta_A^l$  increases monotonically with  $\alpha$ .

As the values of  $\alpha$  and  $t_A$  change,  $g_A$  may vary significantly while  $\eta_A^r$  remains nearly constant. For example, compared to the CP-OPD with  $\alpha = 8.5 \times 10^4 \text{ cm}^{-1}$  and  $t_A = 35$  nm,  $g_A$  of the CP-OPD with  $\alpha = 4.5 \times 10^4 \text{ cm}^{-1}$  and  $t_A = 20$  nm doubles from 0.7 to 1.4, while  $\eta_A^r$  is  $\sim 28\%$  for both devices. The values of  $\alpha$  and  $t_A$  can be chosen depending on the application. For appli-

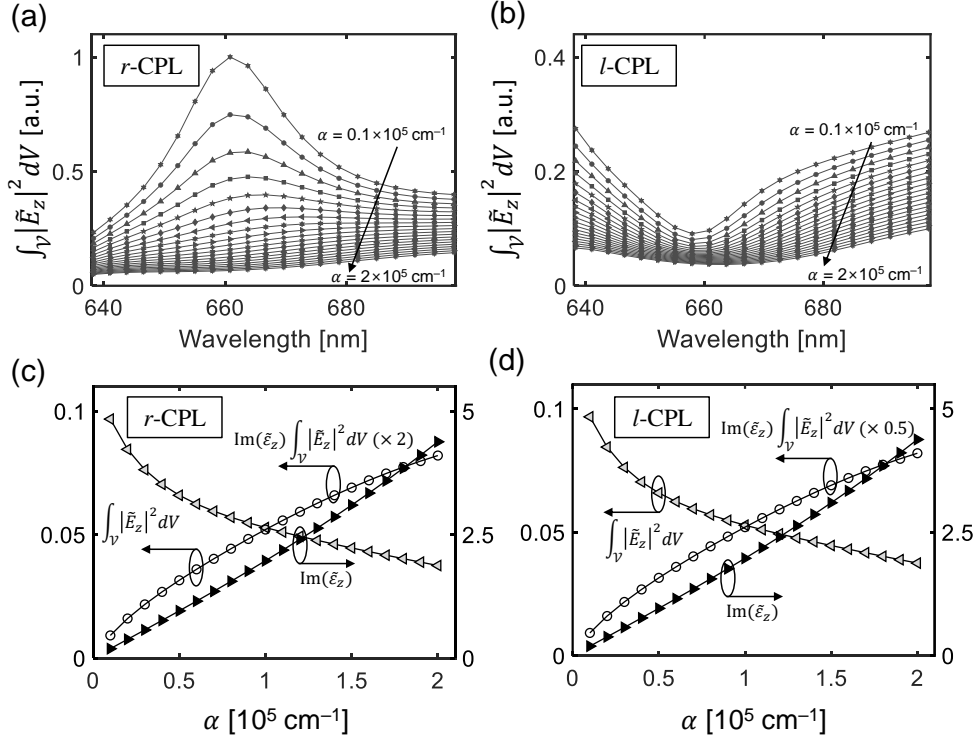


Figure 3.11 Volume integral of  $|\tilde{E}_z(\lambda, \alpha)|^2$  in the absorption layer with  $t_A = 20 \text{ nm}$  under  $r$ -CPL (a) and  $l$ -CPL (b) illumination, calculated with  $\alpha$  varying from  $1 \times 10^4$  to  $2 \times 10^5 \text{ cm}^{-1}$  in  $1 \times 10^4 \text{ cm}^{-1}$  increments. (c) The volume integral of  $|\tilde{E}_z(\lambda, \alpha)|^2$  in the absorption layer (blue), the imaginary part of the  $z$ -component of the relative permittivity ( $\text{Im}(\tilde{\epsilon}_z)$ , orange) of the absorption layer, and their product (red), which is proportional to  $\eta_A$ , under  $r$ -CPL (c) and  $l$ -CPL (d) illumination with  $\lambda = 660 \text{ nm}$ . In the case of  $r$ -CPL, the tradeoff between the volume integral of  $|\tilde{E}_z|^2$  and  $\text{Im}(\tilde{\epsilon}_z)$  is clearly shown, resulting in a maximum of  $\eta_A$  at  $\alpha = 6 \times 10^4 \text{ cm}^{-1}$ . In the case of  $l$ -CPL, on the other hand,  $\eta_A$  increases monotonically with  $\alpha$  because the  $|\tilde{E}_z(\lambda)|^2$  integral decreases much more slowly compared to the  $r$ -CPL case.

ocations requiring high  $g_A$ , the CP-OPD with  $\alpha = 1 \times 10^4 \text{ cm}^{-1}$  and  $t_A = 10 \text{ nm}$  is desirable, yielding  $|g_A| = 1.7$  and  $\eta_A^r = 8.8\%$ . On the other hand, for applications whose primary figure of merit is  $\eta_A^r$ , the device with  $\alpha = 5 \times 10^4 \text{ cm}^{-1}$  and  $t_A = 10 \text{ nm}$ , with the corresponding values of  $|g_A|$  and  $\eta_A^r$  being 1.6 and

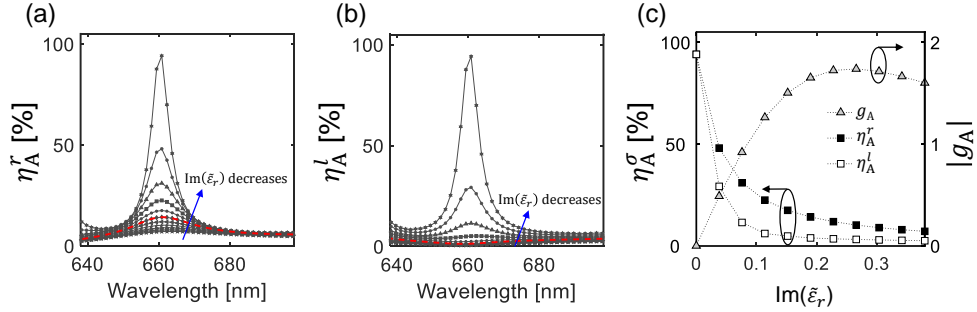


Figure 3.12 Absorption efficiencies of the CP-OPD with  $t_A = 20$  nm and  $\alpha = 1 \times 10^4$  cm $^{-1}$  under  $r$ -CPL (a) and  $l$ -CPL (b) illumination, calculated with  $\text{Im}(\tilde{\epsilon}_r)$  of the top and bottom electrodes varying from 0 to 0.38 in 0.038 increments. The data denoted by red dashed lines correspond to the  $\text{Im}(\tilde{\epsilon}_r)$  value of a silver film ( $= 0.19$ ) taken from the literature [22]. (c) Dissymmetry factor of absorption at  $\lambda = 660$  nm (gray triangles) calculated from (a,b) and absorption efficiencies at  $\lambda = 660$  nm under  $r$ -CPL (filled squares) and  $l$ -CPL (open squares) illumination.

23.8% respectively, is preferred despite slightly lowered  $g_A$ . I note that the values of  $\eta_A^\sigma$  shown in Figs. 3.9 and 3.10, calculated for CPL incident from the semi-infinite glass substrate, are a good approximation to the external quantum efficiency ( $\eta_E^\sigma$ , the number of electrons collected at the electrode divided by the number of incident photons) because (i) a near-unity internal quantum efficiency ( $\eta_I$ , the number of electrons collected at the electrode divided by the number of incident photons) is commonly achieved in the visible spectrum for single donor–acceptor heterojunction OPDs [40, 41, 20], ensuring  $\eta_E^\sigma = \eta_A^\sigma \eta_I^\sigma \simeq \eta_I^\sigma$  and (ii) reflection at the glass–air interface can easily be minimized at the operational wavelength by application of an anti-reflection coating.

Finally, I investigated the effects of the metallic loss of the chiral plasmonic nanocavity on  $\eta_A^\sigma$  and  $g_A$ . Figures 3.12(a) and 3.12(b) show the  $\eta_A^r$  and  $\eta_A^l$  spectra, respectively, for the CP-OPD with  $t_A = 20$  nm and  $\alpha =$

$1 \times 10^4 \text{ cm}^{-1}$ , calculated by varying the  $\text{Im}(\tilde{\epsilon}_r)$  value of silver composing the top and bottom electrodes while fixing the  $\text{Re}(\tilde{\epsilon}_r)$  value. As a reference, the data calculated using  $\text{Im}(\tilde{\epsilon}_r) = 0.19$ , which corresponds to the value of a silver film taken from the literature [22], are denoted by the red dashed lines in Figs. 3.12(a) and 3.12(b). As  $\text{Im}(\tilde{\epsilon}_r)$  decreases, both  $\eta_A^r$  and  $\eta_A^l$  peak with increasingly higher intensities, due to the reduction of the metallic loss competing for absorption with the absorption layer and the concomitant increase in the quality factor of the cavity resonance. Figure 3.12(c) shows the values of  $\eta_A^r$  (filled squares),  $\eta_A^l$  (open squares), and  $|g_A|$  (gray triangles) at  $\lambda = 660 \text{ nm}$ , as a function of  $\text{Im}(\tilde{\epsilon}_r)$ . Except in the highly lossy region where  $\text{Im}(\tilde{\epsilon}_r) > 0.27$ , an increase in  $\text{Im}(\tilde{\epsilon}_r)$ , which is required to increase  $|g_A|$ , necessarily decreases  $\eta_A^r$ , presenting a tradeoff between  $|g_A|$  and  $\eta_A^r$ . In addition,  $|g_A|$  approaches zero as  $\text{Im}(\tilde{\epsilon}_r)$  decreases, consistent with a previous study showing that asymmetric transmission of CPL depending on the helicity occurs only for a lossy planar metamaterial possessing two dimensional chirality [42].

By studying the electromagnetic properties of the CP-OPD, I established a design principle for the maximization of  $\eta_E$  and  $g_A$ . The resulting CP-OPD attains  $\eta_E = 23.8\%$  and  $|g_A| = 1.6$ , representing significant improvements compared to previously demonstrated circular-polarization-sensitive photodetectors (Table 1). I also note that owing to the the vertical geometry and the ultrathin device thickness, the response time of my plasmonic CP-OPD is likely to be significantly shorter than that of chiral photodetectors with the lateral thin-film transistor geometry [6, 29]. According to the reciprocity principle [43, 7], the proposed chiral MDM structure is also expected to be utilized as an optoelectronic platform for organic circularly polarized light emitting diodes.

Table 3.1 Dissymmetry factor of photocurrent ( $g_{\text{Ph}}$ ) and external quantum efficiency ( $\eta_{\text{E}}$ ) of previously demonstrated circular-polarization-sensitive photodetectors compared with those of my photodetector.

Reference	Origin of chirality	$\lambda_{\text{max}}^c$ [nm]	$g_{\text{Ph}}$	$\eta_{\text{E}}$ [%]
[6]	(-)-1-aza[6]helicene	365	1.8	0.1
[26]	( <i>S,S</i> )-prolinol-derived squaraines	545	0.1	50
[27]	( <i>S</i> )-1,1'-binaphthyl derivatives	375	0.1	0.14
[28]	Poly(fluorene- <i>alt</i> -dithienylbenzothiadiazole)	543	0.017	–
[29]	<i>S</i> - $\alpha$ -phenylethylamine lead halide perovskite	395	0.1	253
[15]	Plasmonic nanostructure	1340	1.1	0.2
This work	Plasmonic nanostructure	660	1.6 <sup>b</sup>	23.8 <sup>c</sup>

<sup>a</sup>  $\lambda_{\text{max}}$  is the wavelength at which  $g_{\text{Ph}}$  is maximized.

<sup>b</sup> Dissymmetry factor of absorption ( $g_{\text{A}}$ ).

<sup>c</sup> Absorption efficiency ( $\eta_{\text{A}}$ ).

### 3.4 Bibliography

- [1] J. T. Collins, C. Kuppe, D. C. Hooper, C. Sibia, M. Centini, and V. K. Valev, “Chirality and chiroptical effects in metal nanostructures: fundamentals and current trends,” *Adv. Opt. Mater.*, vol. 5, no. 16, a. 1700182, 2017.
- [2] E. Plum, V. A. Fedotov, and N. I. Zheludev, “Planar metamaterial with transmission and reflection that depend on the direction of incidence,” *Appl. Phys. Lett.*, vol. 94, no. 13, a. 131901, 2009.
- [3] E. Hendry, T. Carpy, J. Johnston, M. Popland, R. V. Mikhaylovskiy, A. J. Laphorn, S. M. Kelly, L. D. Barron, N. Gadegaard, and M. Kadodwala, “Ultrasensitive detection and characterization of biomolecules using superchiral fields,” *Nat. Nanotechnol.*, vol. 5, no. 11, pp. 783–787, 2010.
- [4] W. M. Ye, F. Zeuner, X. Li, B. Reineke, S. He, C.-W. Qiu, J. Liu, Y. Wang, S. Zhang, and T. Zentgraf, “Spin and wavelength multiplexed nonlinear metasurface holography,” *Nat. Commun.*, vol. 7, a. 11930, 2016.
- [5] M. J. Urban, C. Zhou, X. Duan, and N. Liu, “Optically resolving the dynamic walking of a plasmonic walker couple,” *Nano Lett.*, vol. 15, no. 12, pp. 8392–8396, 2015.
- [6] Y. Yang, R. C. Da Costa, M. J. Fuchter, and A. J. Campbell, “Circularly polarized light detection by a chiral organic semiconductor transistor,” *Nat. Photonics*, vol. 7, no. 8, pp. 634–638, 2013.
- [7] K. Konishi, M. Nomura, N. Kumagai, S. Iwamoto, Y. Arakawa, and M. Kuwata-Gonokami, “Circularly polarized light emission from semiconductor planar chiral nanostructures,” *Phys. Rev. Lett.*, vol. 106, no. 5, a. 057402, 2011.

- [8] M. Schäferling, D. Dregely, M. Hentschel, and H. Giessen, “Tailoring enhanced optical chirality: design principles for chiral plasmonic nanostructures,” *Phys. Rev. X*, vol. 2, no. 3, a. 031010, 2012.
- [9] X. Yin, M. Schäferling, B. Metzger, and H. Giessen, “Interpreting chiral nanophotonic spectra: the plasmonic Born–Kuhn model,” *Nano Lett.*, vol. 13, no. 12, pp. 6238–6243, 2013.
- [10] Y. Tang and A. E. Cohen, “Optical chirality and its interaction with matter,” *Phys. Rev. Lett.*, vol. 104, no. 16, a. 163901, 2010.
- [11] N. Berova, L. D. Bari, and G. Pescitelli, “Application of electronic circular dichroism in configurational and conformational analysis of organic compounds,” *Chem. Soc. Rev.*, vol. 36, no. 6, pp. 914–931, 2007.
- [12] X. Shang, I. Song, H. Ohtsu, Y. H. Lee, T. Zhao, T. Kojima, J. H. Jung, M. Kawano, and J. H. Oh, “Supramolecular nanostructures of chiral perylene diimides with amplified chirality for high-performance chiroptical sensing,” *Adv. Mater.*, vol. 29, no. 21, a. 1605828, 2017.
- [13] G. Park, H. Kim, H. Yang, K. R. Park, I. Song, J. H. Oh, C. Kim, and Y. You, “Amplified circularly polarized phosphorescence from co-assemblies of platinum(II) complexes,” *Chem. Sci.*, vol. 10, no. 5, pp. 1294–1301, 2018.
- [14] Y. Luo, C. Chi, M. Jiang, R. Li, S. Zu, Y. Li, and Z. Fang, “Plasmonic chiral nanostructures: Chiroptical effects and applications,” *Adv. Opt. Mater.*, vol. 5, no. 16, a. 1700040, 2017.
- [15] W. Li, Z. J. Coppens, L. V. Besteiro, W. Wang, A. O. Govorov, and J. Valentine, “Circularly polarized light detection with hot electrons in chiral plasmonic metamaterials,” *Nat. Commun.*, vol. 6, a. 8379, 2015.

- [16] M. Pan, Q. Li, Y. Hong, L. Cai, J. Lu, and M. Qiu, “Circular-polarization-sensitive absorption in refractory metamaterials composed of molybdenum zigzag arrays,” *Opt. Express*, vol. 26, no. 14, pp. 17772–17780, 2018.
- [17] X.-T. Kong, L. k. Khorashad, Z. Wang, and A. O. Govorov, “Photothermal circular dichroism induced by plasmon resonances in chiral metamaterial absorbers and bolometers,” *Nano Lett.*, vol. 18, no. 3, pp. 2001–2008, 2018.
- [18] B. P. Rand, D. Cheyns, K. Vasseur, N. C. Giebink, S. Mothy, Y. P. Yi, V. Coropceanu, D. Beljonne, J. Cornil, J.-L. Brédas, and J. Genoe, “The impact of molecular orientation on the photovoltaic properties of a phthalocyanine/fullerene heterojunction,” *Adv. Funct. Mater.*, vol. 22, no. 14, pp. 2987–2995, 2012.
- [19] D. Yokoyama, “Molecular orientation in small-molecule organic light-emitting diodes,” *J. Mater. Chem.*, vol. 21, no. 48, pp. 19187–19202, 2011.
- [20] X. Xiao, K. J. Bergemann, J. D. Zimmerman, K. Lee, and S. R. Forrest, “Small-molecule planar-mixed heterojunction photovoltaic cells with fullerene-based electron filtering buffers,” *Adv. Energy Mater.*, vol. 4, no. 7, a. 1301557, 2014.
- [21] A. S. Baburin, A. M. Merzlikin, A. V. Baryshev, I. A. Ryzhikov, Y. V. Panfilov, and I. A. Rodionov, “Silver-based plasmonics: golden material platform and application challenges [invited],” *Opt. Mater. Express*, vol. 9, no. 2, pp. 611–642, 2019.
- [22] P. Winsemius, F. F. Van Kampen, H. P. Lengkeek, and C. G. Van Went, “Temperature dependence of the optical properties of Au, Ag and Cu,” *J. Phys. F: Met. Phys.*, vol. 6, no. 8, pp. 0305–4608, 1976.

- [23] J. Hao, L. Zhou, and M. Qiu, “Nearly total absorption of light and heat generation by plasmonic metamaterials,” *Phys. Rev. B*, vol. 83, no. 16, a. 165107, 2011.
- [24] A. Pors and S. I. Bozhevolnyi, “Efficient and broadband quarter-wave plates by gap-plasmon resonators,” *Opt. Express*, vol. 21, no. 3, pp. 2942–2952, 2013.
- [25] A. Yanai and U. Levy, “Tunability of reflection and transmission spectra of two periodically corrugated metallic plates, obtained by control of the interactions between plasmonic and photonic modes,” *J. Opt. Soc. Am. B*, vol. 27, no. 8, pp. 1523–1529, 2010.
- [26] M. Schulz, F. Balzer, D. Scheunemann, O. Arteaga, A. Lützen, S. C. J. Meskers, and M. Schiek, “Chiral excitonic organic photodiodes for direct detection of circular polarized light,” *Adv. Funct. Mater.*, vol. 29, no. 16, a. 1900684, 2019.
- [27] N. Y. Kim, J. Kyhm, H. Han, S. J. Kim, J. Ahn, D. K. Hwang, H. W. Jang, B.-K. Ju, and J. A. Lim, “Chiroptical-conjugated polymer/chiral small molecule hybrid thin films for circularly polarized light-detecting heterojunction devices,” *Adv. Funct. Mater.*, vol. 29, no. 11, a. 1808668, 2019.
- [28] J. Gilot, R. Abbel, G. Lakhwani, E. W. Meijer, A. P. H. J. Schenning, and S. C. J. Meskers, “Polymer photovoltaic cells sensitive to the circular polarization of light,” *Adv. Mater.*, vol. 22, no. 20, pp. E131–E134, 2010.
- [29] C. Chen, L. Gao, W. R. Gao, C. Y. Ge, X. Du, Z. Li, Y. Yang, G. D. Niu, and J. Tang, “Circularly polarized light detection using chiral hybrid perovskite,” *Nat. Commun.*, vol. 10, a. 1927, 2019.

- [30] R. Farshchi, M. Ramsteiner, J. Herfort, A. Tahraoui, and H. T. Grahn, “Optical communication of spin information between light emitting diodes,” *Appl. Phys. Lett.*, vol. 98, no. 16, a. 162508, 2011.
- [31] J. F. Sherson, H. Krauter, R. K. Olsson, B. Julsgaard, K. Hammerer, I. Cirac, and E. S. Polzik, “Quantum teleportation between light and matter,” *Nature*, vol. 443, no. 7111, pp. 557–560, 2006.
- [32] C. Wagenknecht, C.-M. Li, A. Reingruber, X.-H. Bao, A. Goebel, Y.-A. Chen, Q. A. Zhang, K. Chen, and J.-W. Pan, “Experimental demonstration of a heralded entanglement source,” *Nat. Photonics*, vol. 4, no. 8, pp. 549–552, 2010.
- [33] B. Ranjbar and P. Gill, “Circular dichroism techniques: biomolecular and nanostructural analyses- a review,” *Chem Biol Drug Des*, vol. 74, no. 2, pp. 101–120, 2009.
- [34] M. L. Brongersma, N. J. Halas, and P. Nordlander, “Plasmon-induced hot carrier science and technology,” *Nat. Nanotechnol.*, vol. 10, no. 1, pp. 25–34, 2015.
- [35] T. P. White and K. R. Catchpole, “Plasmon-enhanced internal photoemission for photovoltaics: theoretical efficiency limits,” *Appl. Phys. Lett.*, vol. 101, no. 7, a. 073905, 2012.
- [36] C. Clavero, “Plasmon-induced hot-electron generation at nanoparticle/metal-oxide interfaces for photovoltaic and photocatalytic devices,” *Nat. Photonics*, vol. 8, no. 2, pp. 95–103, 2014.
- [37] S. E. Burns, N. Pfeffer, J. Grüner, M. Remmers, T. Javoreck, D. Neher, and R. H. Friend, “Measurements of optical electric field intensities in

- microcavities using thin emissive polymer films,” *Adv. Mater.*, vol. 9, no. 5, pp. 395–398, 1997.
- [38] P. Peumans, V. Bulović, and S. R. Forrest, “Efficient photon harvesting at high optical intensities in ultrathin organic double-heterostructure photovoltaic diodes,” *Appl. Phys. Lett.*, vol. 76, no. 19, pp. 2650–2652, 2000.
- [39] H. Gommans, B. Verreet, B. P. Rand, R. Muller, J. Poortmans, P. Heremans, and J. Genoe, “On the role of bathocuproine in organic photovoltaic cells,” *Adv. Funct. Mater.*, vol. 18, no. 22, pp. 3686–3691, 2008.
- [40] J. Zhao, Y. Li, G. Yang, K. Jiang, H. Lin, H. Ade, W. Ma, and H. Yan, “Efficient organic solar cells processed from hydrocarbon solvents,” *Nat. Energy*, vol. 1, no. 2, a. 15027, 2016.
- [41] V. Vohra, K. Kawashima, T. Kakara, T. Koganezawa, I. Osaka, K. Takimiya, and H. Murata, “Efficient inverted polymer solar cells employing favourable molecular orientation,” *Nat. Photonics*, vol. 9, no. 6, pp. 403–408, 2015.
- [42] E. Plum and N. I. Zheludev, “Chiral mirrors,” *Appl. Phys. Lett.*, vol. 106, no. 22, a. 221901, 2015.
- [43] A. A. Maksimov, I. I. Tartakovskii, E. V. Filatov, S. V. Lobanov, N. A. Gippius, S. G. Tikhodeev, C. Schneider, M. Kamp, S. Maier, S. Höfling, and V. D. Kulakovskii, “Circularly polarized light emission from chiral spatially-structured planar semiconductor microcavities,” *Phys. Rev. B*, vol. 89, no. 4, a. 045316, 2014.

## Chapter 4

# Conclusions

I have demonstrated promising nanophotonic approaches to improve the light-matter interactions in the 1-D planar multilayer structures and the 3-D periodic nanophotonic structures, and applied them to organic and hybrid solar cells and CPL emitting organic diodes and CPL detecting organic photodiodes. Together with the nanophotonic engineering, organic material systems employed as the photoactive materials are shown to be advantageous to fully explore the potential performances of optoelectronic devices due to the controllable polarizability. The chiral optoelectronics attracting much interest has been limited in practicality due to the fundamental tradeoff between the quantum efficiency and the dissymmetry factor. I have proposed a chiral cavity structure to overcome this tradeoff, which can be used as a plasmonic platform for high-performance CPL emitters and detectors. In the future, CPL emitting devices will be a solution to overcome the efficiency limits of the current OLED display due to the presence of the anti-glare filter that reduces 50 % of luminescence efficiency. They also can be applied to virtual reality and

augmented reality displays eliminating the CPL filter used in those devices, thus increasing their luminance. Furthermore, the chiral plasmonic emitter and absorber may be employed as building blocks of quantum information systems.

The limitations of this study are probably in fabrication and lack of useful plasmonic materials. Silver used as a plasmonic material may have a little optical loss in visible frequency depending on deposition methods. The development of materials that can minimize plasmonic losses in the optical frequency domain is urgent and desirable. In addition, electron beam lithography, which is often used to fabricate nanostructures, is very inefficient in terms of cost and time. Development of a bottom-up process based on nanochemistry instead of top-down lithography may increase the practicality of nanophotonic approaches.

# Appendix A

## Morphology of Lead Phthalocyanine Thin Films

### A.1 Analysis of Grazing Incidence Wide Angle X-ray Scattering Spectra

Figure A.1 shows 2D-GIWAXS spectra of the three types of PbPc films, where  $q_z$  and  $q_{xy}$  are, respectively, the out-of-plane and in-plane components of the scattering vector  $\mathbf{q}$ , defined as the change in wave vector between the incident and diffracted beams. I note that, instead of Si (or SiO<sub>2</sub>) substrates preferred for increased signal-to-noise ratios, ITO substrates were used because of the following reason: crystallinity and spread of crystal-plane orientations of PbPc films deposited on Si (or SiO<sub>2</sub>) varies significantly from those of PbPc films on ITO, on which the three types of PbPc-C<sub>60</sub> solar cells were fabricated. Since the inevitable use of the ITO-coated substrates makes it difficult to clearly distinguish Bragg signals of PbPc from the background signal in the  $q_{xy}$ - $q_z$  plane where  $q > 1 \text{ \AA}^{-1}$  (Fig. A.1), my discussions are focused on Bragg signals

occurring in three regions—Region 1, 2, and 3 with  $q \leq 1 \text{ \AA}^{-1}$  enclosed by dashed boundaries in Fig. A.1(a).

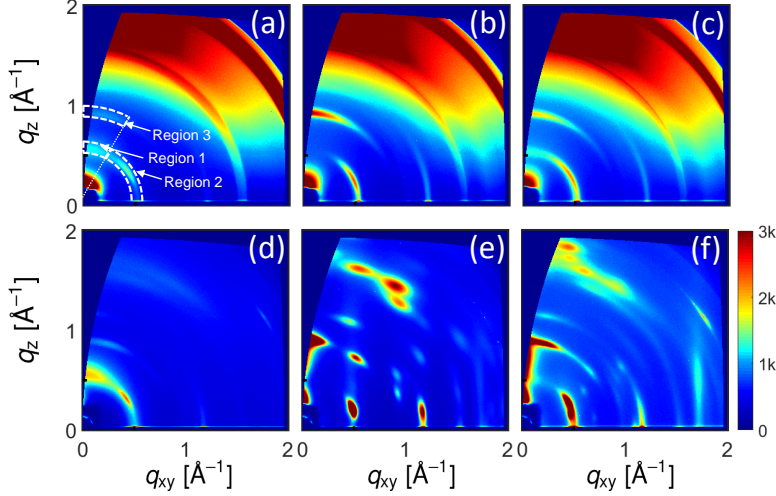


Figure A.1 2D-GIWAXS spectra of the (a) n-PbPc, (b) c-PbPc, and (c) bi-PbPc films prepared on glass / ITO substrates, and those of the (d) n-PbPc, (e) c-PbPc, and (f) bi-PbPc films on Si substrates, in the  $q_{xy}$ - $q_z$  plane with  $q < 2 \text{ \AA}^{-1}$ .

Figure A.1(a) shows the GIWAXS spectrum of a non-templated PbPc (n-PbPc) thin film, where the weak and broad signals in Regions 1 to 3 are attributed to orientational disorder of crystalline domains, and the particularly diffusive background in Region 1 also indicates the existence of amorphous domains. For CuI- and CuI/ZnPc bilayer-templated (c-PbPc and bi-PbPc, respectively) films, the GIWAXS spectra in Figs. A.1(b) and A.1(c) show significant increases in signal intensity in Regions 2 and 3, indicative of increased crystallinity. At the same time, their optical absorption coefficients  $\alpha$  shown in Fig. A.2(a) increase and decrease around 900 nm and 740 nm, respectively, compared to the corresponding value of the n-PbPc film. Since it is well established for PbPc crystals that the monoclinic (or amorphous)-to-triclinic

phase transition gives rise to an abrupt shift of the absorption peak from near 740 nm to near 900 nm [1, 2, 3], the  $\alpha$  spectra shown in Fig. A.2(a) indicate that volume fractions occupied by triclinic crystallites in the c- and bi-PbPc films are significantly increased, and that their increased intensities in Regions 2 and 3 are likely due to diffraction from the triclinic crystallites. Considering the previous study by Vasseur *et al.* based on complementary GIWAXS and X-ray reflectivity measurements on PbPc films with varying thicknesses deposited on substrates with different surface energies [3], the majority of triclinic crystallites in the c-PbPc film likely adopts an almost face-on orientation. Furthermore, since  $\alpha$  of the bi-PbPc differs appreciably from that of the c-PbPc only in the NIR region, the differences in Bragg signals of the bi-PbPc compared to the c-PbPc, i.e., the presence of the Bragg signals in Region 1 and the broader signals in Region 2, mean that morphological characteristics of triclinic crystalline domains in these two films are different.

From the GIWAXS signals along the arc defined by  $q = 0.54 \text{ \AA}^{-1}$  as a function of  $\chi$ , the angle between  $\mathbf{q}$  and the  $q_z$ -axis (Fig. A.2b), the full widths at half maximum (FWHMs) of the Bragg peaks in Region 2 extracted from the Gaussian fits are determined to be  $51.1^\circ$  and  $67.2^\circ$  for the c- and bi-PbPc films, respectively. Also, the signal in a broad range of  $\chi$  from  $0^\circ$  to  $57^\circ$  is larger for the bi-PbPc than the c-PbPc. These results indicate that the degree of face-on orientation is smaller for the bi-PbPc than the c-PbPc: a smaller number of PbPc molecules in the bi-PbPc are, on average, in the face-on orientation, with a broader orientation distribution compared to the c-PbPc [3]. This change in molecular orientation of the bi-PbPc is expected to decrease the alignment between the directions of the polarization of incident light and the transition dipole moment of the molecules, consistent with its  $\alpha$  smaller than that of the c-PbPc in the NIR region, as shown in Fig. A.2(a).

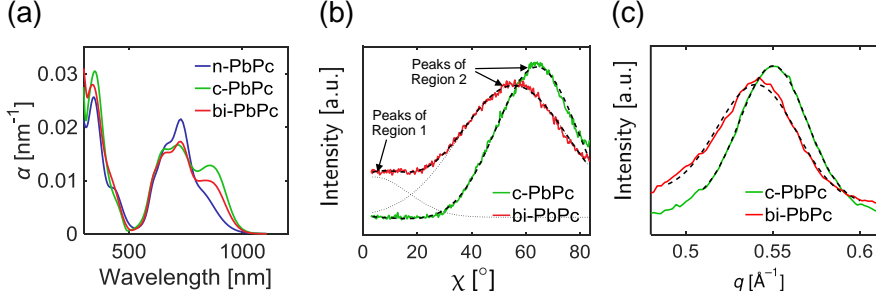


Figure A.2 (a) Absorption coefficient  $\alpha$  spectra of the three types of PbPc films. Line cuts (b) along the arc defined by  $q = 0.54 \text{ \AA}^{-1}$ , and (c) along the directions of  $\chi \simeq 60^\circ$  of the GIWAXS spectra of the c-PbPc (green) and bi-PbPc (red) films. The dashed lines in (b,c) are the Gaussian fits to the line cuts. The fit for the bi-PbPc in (b) can be decomposed into the two dotted lines that represent Bragg peaks in Regions 1 and 2.

In Figure A.2(c), I draw line cuts of the Bragg spectra along the directions defined by  $\chi = 57^\circ$  and  $62^\circ$  corresponding to the locations of the peaks shown in Fig. A.2(b) for the bi- and c-PbPc, respectively, showing that the FWHM for the bi-PbPc ( $=0.076 \text{ \AA}^{-1}$ ) is larger than that for the c-PbPc ( $=0.064 \text{ \AA}^{-1}$ ). The approximate sizes  $L$  of the crystallites in this direction ( $\chi \simeq 60^\circ$ ), calculated by Scherrer's equation,  $L = 0.9 \times 2\pi/\text{FWHM}$ , [4] are 75 and 88  $\text{\AA}$  for the bi-PbPc and c-PbPc, respectively. The morphological features of the bi-PbPc that are different from those of the c-PbPc—less face-on orientation with a broader orientation distribution and the decrease in crystallite size, as schematically described in Figs. 3(e) and 3(f) in the main text—are induced by randomly oriented ZnPc molecules in the bi-layer template, as is confirmed in the following paragraph.

The GIWAXS spectrum of a 6-nm-thick ZnPc layer deposited on 1-nm-thick CuI layer shows a ring-shaped pattern in Regions 1 and 2, and a diffusive background in Region 1 [Fig. A.3(a)]. This indicates that ZnPc molecules in this sample are mostly disordered and that a small number of ordered

molecules that form crystallites are randomly oriented as depicted in Fig. A.3(b). As a result, compared to the *c*-PbPc film, the PbPc film deposited on the CuI/ZnPc bilayer consists of smaller crystallites with a broader orientation distribution. In addition, the CuI/ZnPc bilayer has much weaker Bragg signals than the bi-PbPc film [Fig. A.1(c)], suggesting that it is fair to ignore the diffractions due to the CuI/ZnPc bilayer when analyzing the GIWAXS spectrum of the bi-PbPc film. When the thickness of the ZnPc layer is increased to 20 nm, a notable Bragg peak appears in Region 2 [(Fig. A.3(c)], indicating that an upper portion of this film consists predominantly of well-ordered ZnPc molecules with a face-on orientation [5, 6], as schematically depicted in Fig. A.3(d). This is consistent with previous studies reporting that a CuI template induces face-on oriented phthalocyanines [5, 7].

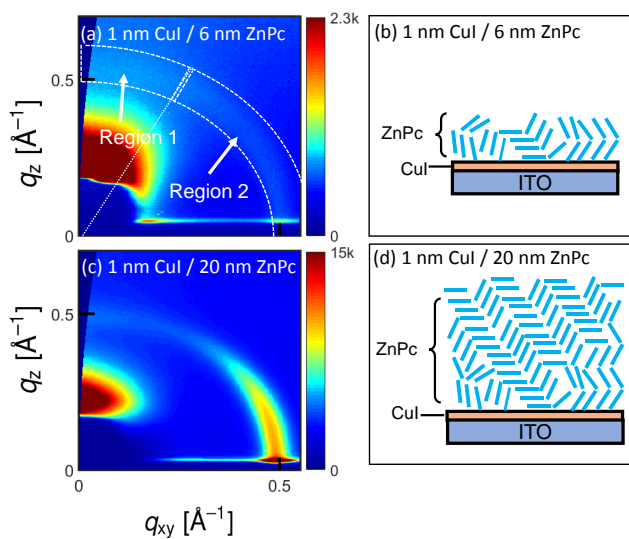


Figure A.3 (a) A GIWAXS spectrum and (b) a schematic of the crystalline structure of a 6-nm-thick ZnPc layer. (c) A GIWAXS spectrum and (d) a schematic of the crystalline structure of a 20-nm-thick ZnPc layer. In both cases, the ZnPc films were deposited on a 1-nm-thick CuI layer deposited on a glass substrate pre-coated with an ITO layer.

## A.2 Bibliography

- [1] A. Miyamoto, K. Nichogi, A. Taomoto, T. Nambu, and M. Murakami, “Structural control of evaporated lead-phthalocyanine films,” *Thin Solid Films*, vol. 256, no. 1-2, pp. 64–67, 1995.
- [2] D. Campbell and R. A. Collins, “Spectral response of monoclinic and triclinic lead phthalocyanine to nitrogen-dioxide,” *Thin Solid Films*, vol. 261, no. 1-2, pp. 311–316, 1995.
- [3] K. Vasseur, K. Broch, A. L. Ayzner, B. P. Rand, D. Cheyons, C. Frank, F. Schreiber, M. F. Toney, L. Froyen, and P. Heremans, “Controlling the texture and crystallinity of evaporated lead phthalocyanine thin films for near-infrared sensitive solar cells,” *ACS Appl. Mater. Interfaces*, vol. 5, no. 17, pp. 8505–8515, 2013.
- [4] A. Salleo, R. J. Kline, D. M. DeLongchamp, and M. L. Chabinyc, “Microstructural characterization and charge transport in thin films of conjugated polymers,” *Adv. Mater.*, vol. 22, no. 34, pp. 3812–3838, 2010.
- [5] J. W. Kim, H. J. Kim, T.-M. Kim, T. G. Kim, J.-H. Lee, J. W. Kim, and J.-J. Kim, “High performance organic planar heterojunction solar cells by controlling the molecular orientation,” *Curr. Appl. Phys.*, vol. 13, no. 1, pp. 7–11, 2013.
- [6] H. Jung Kim, H.-S. Shim, J. Whan Kim, H. Hwi Lee, and J.-J. Kim, “Cui interlayers in lead phthalocyanine thin films enhance near-infrared light absorption,” *Appl. Phys. Lett.*, vol. 100, no. 26, p. a. 263303, 2012.
- [7] B. P. Rand, D. Cheyons, K. Vasseur, N. C. Giebink, S. Mothy, Y. P. Yi, V. Coropceanu, D. Beljonne, J. Cornil, J.-L. Brédas, and J. Genoe, “The

impact of molecular orientation on the photovoltaic properties of a phthalocyanine/fullerene heterojunction,” *Adv. Funct. Mater.*, vol. 22, no. 14, pp. 2987–2995, 2012.

## Appendix B

# Analysis of the Internal Quantum Efficiency of Lead Phthalocyanine–C<sub>60</sub> Heterojunction Based Solar Sells

### B.1 Coupled Optical and Exciton Diffusion Analyses

The morphological changes upon employing the template layers are expected to affect the  $J$ – $V$  characteristics by altering the exciton diffusion length  $L_d$  of PbPc and the CT-dissociation efficiency  $\eta_{cs}$ , which are sensitive to the bulk and the D–A interfacial morphology, respectively. In addition, the insertion of the template layers between the ITO and PbPc layers modifies the exciton quenching rates  $k_q$  at the PbPc interfaces facing the ITO, thus determining, together with  $L_d$ , the exciton diffusion efficiency  $\eta_{ed}$ . Here,  $\eta_{ed}$  is defined as the probability that a photogenerated exciton in the active layer reaches the D–A interface, and  $\eta_{cs}$  as the probability that an exciton reaching the D–A interface is converted into charge separated species. For the three types of

PbPc-based bilayer solar cells studied here, a precise quantification of  $L_d$ ,  $\eta_{ed}$ , and  $\eta_{cs}$  is difficult for the following reasons. Because of the extremely weak fluorescence from PbPc [1], the commonly employed method for determining  $L_d$  using fluorescence quenching is not applicable [2, 3]. A simple method to determine  $\eta_{cs}$  is to assume it to be equal to the ratio of the photocurrent at zero bias to the saturated photocurrent under a sufficiently large reverse bias [4, 5]. However, this cannot be used in my case since the implicit assumption that  $\eta_{ed} = 1$  is not appropriate. Transient absorption spectroscopy has often been used to investigate CT-related dynamics of the bulk heterojunction OSCs [6, 7]. For my planar heterojunction devices, however, the signal due to CT excitons resulting from charge transfer that is preceded by exciton diffusion may cause inaccuracy in determining  $\eta_{cs}$ .

Therefore, I instead estimated possible ranges of  $\eta_{ed}$  and  $\eta_{cs}$  as functions of  $L_d$  by assuming for each device an appropriate range of  $k_q$  at the PbPc interface facing the ITO:  $\eta_{ed}$  at each wavelength  $\lambda$  was first determined by solving the exciton diffusion equation with different  $L_d$  using the absorption profile [8]; next, wavelength-independent  $\eta_{cs}$  was determined as the value that best matches the simulated and measured EQE( $\lambda$ ) [ $=\eta_{abs}(\lambda)\times\eta_{ed}(\lambda)\times\eta_{cs}$ ] (dashed and solid lines in Fig. 2.10(a), respectively). In obtaining  $\eta_{cs}$ , I assumed that all CS species are collected at the respective electrode. The range of  $k_q$  specifying the boundary condition of the exciton diffusion equation was determined for each device as follows. At the ITO–PbPc and CuI–PbPc interfaces, since the PbPc excitons are very close to the conductor (i.e., ITO), with an exciton-to-conductor separation  $d < 1$  nm for the ITO–PbPc and  $d < 2$  nm for the CuI–PbPc, they are expected to be quenched through non-radiative energy transfer. Following a model based on dipole–dipole couplings, where the rate of energy transfer from an exciton in a dielectric to an adjacent conductor

is  $10^{-9}d^{-3} \text{ cm}^3 \text{ s}^{-1}$  [9], it is estimated that  $k_q > 10^{12} \text{ s}^{-1}$  for the ITO–PbPc and  $k_q > 10^{11} \text{ s}^{-1}$  for the CuI–PbPc. At the ZnPc–PbPc interface, on the other hand, exciton quenching due to energy transfer is negligible since (i) the presence of the 6-nm-thick ZnPc layer significantly lowers the rate of energy transfer from PbPc to ITO [9], making the lifetime ( $1/k_q$ ) comparable to the intrinsic lifetime of singlet excitons commonly known to be  $\sim 1 \text{ ns}$  [10, 11, 12], and (ii) the fact that  $E_{\text{opt}}$  of the PbPc is smaller than that of the ZnPc (Table 1) implies that Förster energy transfer from PbPc to ZnPc is mostly forbidden [13]. Exciton quenching due to charge transfer from PbPc to ZnPc cannot be ruled out, but it is likely inefficient since the highest occupied molecular orbital (HOMO) level of PbPc is slightly below that of ZnPc: for PbPc deposited on ZnPc, the difference between the HOMO levels was found to be  $\sim 0.16 \text{ eV}$  by ultraviolet photoelectron spectroscopy (UPS), which is notably lower than that in typical OSCs where the HOMO (or the lowest unoccupied molecular orbital, LUMO) level differences are chosen to be larger than  $0.3 \text{ eV}$  for efficient charge transfer [14]. Regarding the APFO3–PCBM interface having the LUMO level difference of  $0.3 - 0.4 \text{ eV}$  and  $k_q$  of  $5 \times 10^{12} \text{ s}^{-1}$  as a reference point [15, 16, 17, 18], I estimated using the Marcus theory that the small HOMO level difference of  $\sim 0.16 \text{ eV}$  at the ZnPc–PbPc interface translates into  $k_q$  of  $5 \times 10^{10} \text{ s}^{-1} - 5 \times 10^{11} \text{ s}^{-1}$  [10], smaller by a factor of  $10 - 100$  than that of the APFO3–PCBM case. This  $k_q$  value is possibly overestimated because of errors in determining the free energy term in the exponent in the Marcus theory, but its influence on my conclusion of the analysis in this section is insignificant. The range of  $k_q$  is then narrowed to  $5 \times 10^{10} \text{ s}^{-1} \leq k_q \leq 2 \times 10^{11} \text{ s}^{-1}$ , noting that the EQE fit with  $k_q > 2 \times 10^{11} \text{ s}^{-1}$  at  $L_d = 30 \text{ nm}$ , the largest  $L_d$  previously reported for phthalocyanine films [12], yields  $\eta_{\text{cs}} > 1$ . At D–A interfaces in all devices,  $k_q$  is assumed to be infinite since the singlet exciton

life time is in general several thousand time larger than the CT state formation time [19, 20].

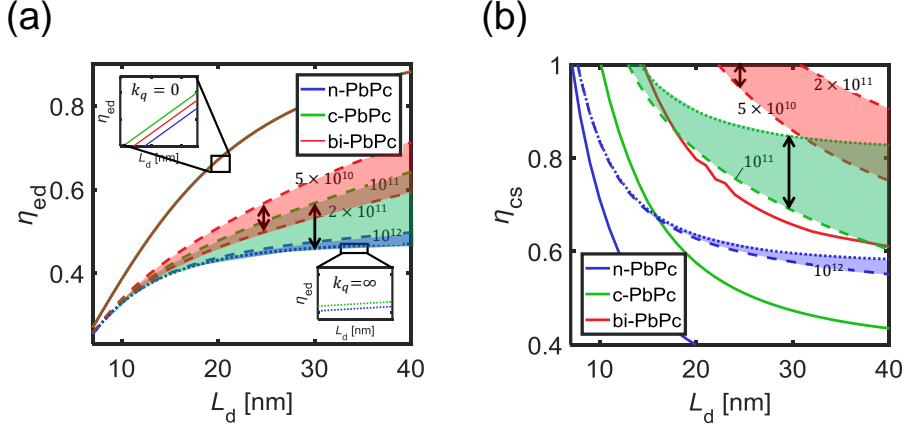


Figure B.1 Calculated (a) exciton diffusion efficiency  $\eta_{ed}$  and (b) CT-dissociation efficiency  $\eta_{cs}$  of the n-PbPc (blue), c-PbPc (green), and bi-PbPc (red) devices. Solid, dotted, and dashed lines are the data calculated with the non-quenching ( $k_q = 0$ ), perfect-quenching ( $k_q = \infty$ ), and partial-quenching ( $k_q$  [s $^{-1}$ ] shown near each dashed line) boundary conditions, respectively. Note that the solid (and dotted) lines in (a) are very closely located.

Figure B.1 shows the calculated  $\eta_{ed}$  and  $\eta_{cs}$  as functions of  $L_d$ , where solid, dashed, and dotted lines correspond, respectively, to the data obtained with non-, partial-, and perfect-quenching boundary conditions at the template- and the ITO-PbPc interfaces. The values of  $\eta_{ed}$  plotted in Fig. B.1 are the solar-spectrum-weighted averages of  $\eta_{ed}(\lambda)$  over spectral regions where PbPc is absorptive. As  $L_d$  increases or  $k_q$  decreases, the contribution of  $\eta_{ed}$  to the IQE increases, while that of  $\eta_{cs}$  decreases. The shaded regions, bounded by the data calculated under the boundary conditions specified by the  $k_q$  values determined above, are where the actual parameters of  $L_d$ ,  $\eta_{ed}$ , and  $\eta_{cs}$  are located. Most of the red region, corresponding to the bi-PbPc device, is located above the others, suggesting that  $\eta_{ed}$  and  $\eta_{cs}$  of the bi-PbPc device are larger

than those of the other devices. The validity of this claim obviously depends on the actual values of  $L_d$  and therefore the estimates of  $L_d$  are necessary: the claim does not hold when  $L_d$  of c-PbPc is much larger than that of bi-PbPc, which may not seem unlikely considering the morphological characteristics of the PbPc films discussed in the section of Thin Film Morphology.  $L_d$  can be estimated to be equal to the thickness of the PbPc layer in each device that maximizes  $J_{sc}$ , which is 24 and 30 nm for the bi- and c-PbPc devices, respectively (data not shown). The ranges of  $\eta_{ed}$  and  $\eta_{cs}$  of the bi- and c-PbPc devices at the estimated values of  $L_d$  are marked by double-headed arrows in Fig. B.1, showing the increased likelihood that the bi-PbPc has larger  $\eta_{ed}$  than the c-PbPc, and, perhaps more interestingly, that larger  $\eta_{cs}$  of the bi-PbPc than that of the c-PbPc has contributed to the increased IQE of the former device.

## B.2 Charge Transferred- and Charge Separated-State Energetics

The differences in  $\eta_{cs}$  among the three types of PbPc devices inferred from the analysis in the previous section are likely to be due to changes in CT and CS state energetics arising from the morphological changes in the PbPc films. In this section, using the entropy- and disorder-driven charge separation model [10, 21], I present another argument suggesting that  $\eta_{cs}$  of the bi-PbPc device is increased relative to the other two devices. According to this model, the height of the free energy barrier  $\Delta G$  that CT excitons should overcome to be separated into free carriers can be estimated as the difference between the free energy of the CS state  $G_{cs}$  and that of the CT state  $G_{ct}$ ,

$$\Delta G = G_{cs} - G_{ct} = \Delta H - T\Delta S, \quad (\text{B.1})$$

where  $\Delta H$  (or  $\Delta S$ ) is the change in enthalpy (or entropy) associated with the CT-dissociation process, and  $T$  is the temperature. Although it has been discussed that  $\Delta H$  is equal to the change in the Coulombic potential energy [10, 22, 23], it is difficult to either directly measure the Coulombic potential energy ( $U = e^2/4\pi\epsilon r$ ) or calculating it without accurately knowing the electron-hole separation  $r$  (i.e., the spatial extent of CT exciton) and the permittivity  $\epsilon$  of the surrounding medium. Therefore, similar to the previous studies [24, 25], I assume that  $\Delta H$  is equal to the difference between the lowest CS state energy  $E_{cs}$  and the average CT state energy  $E_{ct}$ :

$$\Delta H = E_{cs} - E_{ct}. \quad (\text{B.2})$$

From the difference between the HOMO of PbPc and the LUMO of C<sub>60</sub>, the  $E_{cs}$  values of the n-, c-, and bi-PbPc devices were obtained to be 1.07, 0.99, and 1.04 eV, respectively, where the HOMO levels (5.07, 4.99, and 5.04 eV below the vacuum level for the n-, c-, and bi-PbPc, respectively) were determined by UPS and the LUMO of C<sub>60</sub> (4 eV below the vacuum level) was taken from the literature [26]. The  $E_{ct}$  values were extracted by fitting the measured temperature-dependence of  $V_{oc}$  to the following model derived by Burke *et al.* based on equilibrium between CT states and free carriers [25],

$$V_{oc} = \frac{E_{ct}}{e} - \frac{\sigma_{ct}^2}{2ekT} - \frac{kT}{e} \log\left(\frac{J_{s0}}{J_{sc}}\right). \quad (\text{B.3})$$

Here,  $\sigma_{ct}$  is the standard deviation of CT state energy distribution,  $e$  is the elementary charge,  $k$  is Boltzmann's constant,  $J_{s0}$  is a variable proportional to the recombination current of CT excitons. The fitting parameters were  $E_{ct}$ ,  $\sigma_{ct}$ , and  $J_{s0}$ , and their extracted values are expected to be reliable, since the three terms in Eq. (B.3) have very different temperature dependencies.

Figure B.2 shows  $V_{oc}$  measured in a temperature range from 100 to 297K (open

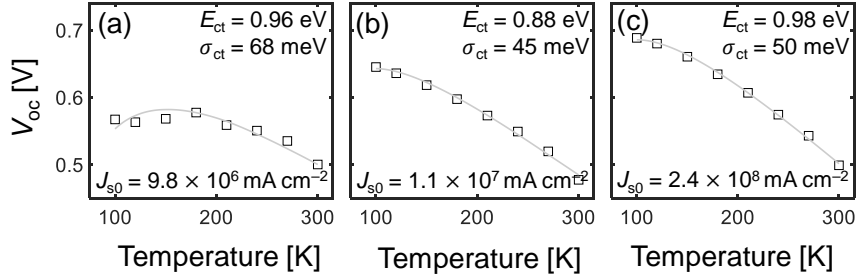


Figure B.2 Temperature-dependence of open-circuit voltages  $V_{oc}$  of the (a) n-PbPc, (b) c-PbPc, and (c) bi-PbPc devices. Symbols and dashed lines indicate the measured data and the fits, respectively. The extracted parameters (average energy of charge-transfer (CT) states  $E_{ct}$ , standard deviation of CT state energy distribution  $\sigma_{ct}$ , and a variable proportional to the recombination current of CT excitons  $J_{s0}$ ) are listed inside the figures.

symbols), fits to the model described by Eq. (B.3) (lines), and extracted fitting parameters. The values of  $\Delta H$ , determined from the extracted  $E_{ct}$  and  $E_{cs}$ , are shown in Fig. B.3(a) (red symbols), where I find that the bi-PbPc device has much smaller  $\Delta H$  compared to the other devices. The more generally used method for extracting  $E_{ct}$  based on measurements of the sub- $E_{opt}$  absorption spectrum and the electroluminescence from CT states could not be used in this case, since fluorescence from the PbPc- $C_{60}$  CT states was not observed.

Next, I calculated  $H$  and  $G$  for the three types of devices using the following equations [27, 21]:

$$H(r) = \left\langle \frac{1}{Z(r)} \sum_{\alpha=1}^{\Omega(r)} E_{\alpha} \exp\left(-\frac{E_{\alpha}}{k_b T}\right) \right\rangle \quad (\text{B.4})$$

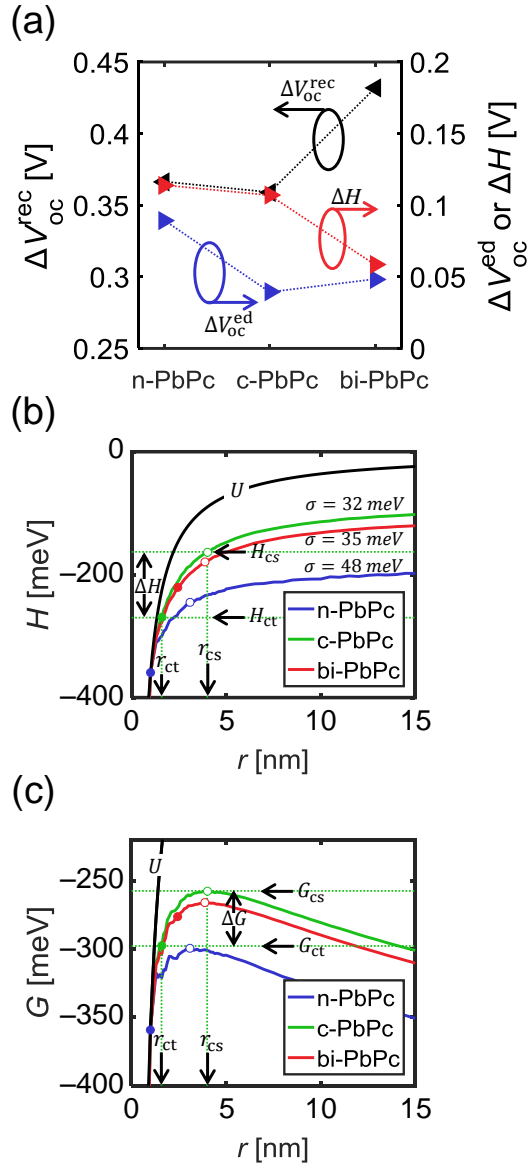


Figure B.3 (a) Origins of open-circuit voltage  $V_{oc}$  loss. (b) Enthalpy  $H$  and (c) free energy  $G$  of an electron-hole pair as functions of their separation  $r$ . Open circles in (b) and (c) denote the enthalpy  $H_{cs}$  and the free energy  $G_{cs}$  of the CS state, respectively, while filled circles in (b) and (c) denote the enthalpy  $H_{ct}$  and the free energy  $G_{ct}$  of the CT state, respectively.

and

$$G(r) = -\langle kT \log Z(r) \rangle, \quad (\text{B.5})$$

where

$$Z(r) = \sum_{\alpha=1}^{\Omega(r)} \exp\left(-\frac{E_{\alpha}}{k_{\text{b}}T}\right) \quad (\text{B.6})$$

and

$$E_{\alpha} = U(r) + E_{\alpha}^{\text{e}} + E_{\alpha}^{\text{h}}. \quad (\text{B.7})$$

Here,  $Z$  is the canonical partition function,  $\Omega$  is the total number of available states for electrons and holes,  $E_{\alpha}^{\text{e}}$  (or  $E_{\alpha}^{\text{h}}$ ) is a normal distribution with a standard deviation  $\sigma$ , describing the broadening of energy distribution of electrons (or holes), and  $\langle \cdot \rangle$  denotes an ensemble average. All parameters used to calculate Eq. (B.4) – (B.7) except for  $\sigma$  were the same as those in the study by Hood *et al.* representing the typical values for OSCs [21]. The  $\sigma$  values for the n-, c-, and bi-PbPc devices were estimated to be 48, 32, and 35 meV, respectively, from the relation  $\sigma_{\text{ct}} = \sqrt{2}\sigma$  derived from an assumption that the CT state is a product of a molecular orbital accommodating a hole and that accommodating an electron. Colored solid lines in Fig. B.3(b) and Fig. B.3(c) are the calculated  $H$  and  $G$ , respectively, and the black solid lines in both figures represent  $U$ . In Fig. B.3(b),  $H$  is noticeably smaller than  $U$  for most  $r$  because of the influence of energetic disorder, where  $H$  decreases with increasing  $\sigma$ . This tendency is attributed to the fact that as the energy distribution of CS states broadens (i.e., as  $\sigma$  increases), the average energy of CS states that CT excitons are converted into decreases [21]. The entropic contribution implicitly

introduced in Eq. (B.5) [21] makes  $G$  [Fig. B.3(c)] smaller than  $H$  [Fig. B.3(b)] for most  $r$  and results in maxima of  $G$  [indicated by open circles in Fig. B.3(c)] occurring at  $r = 3.4, 4.1,$  and  $4$  nm for the n-, c-, and bi-PbPc devices, respectively. Since each of these  $r$  values represents the minimum electron-to-hole distance at which the electron and hole can spontaneously dissociate, which is denoted by  $r_{cs}$ , I regard the maximum of  $G$  as the free energy of the CS state: i.e.,  $G(r_{cs}) = G_{cs}$ . From  $r_{cs}$ , I then determined  $H_{cs}[= H(r_{cs})]$ , the enthalpy of the CS state, denoted by open circles in Fig. B.3(b). Next,  $H_{ct}$ , the enthalpy of the CT state, was determined using the relation  $H_{ct} = H_{cs} - \Delta H$ , with  $\Delta H$  calculated above [those plotted in Fig. B.3(a)], from which  $r_{ct}$ , representing the electron-to-hole separation immediately after charge transfer, was calculated by requiring that  $H(r_{ct}) = H_{ct}$ . Points  $(r_{ct}, H_{ct})$  are marked by filled circles in Fig. B.3(b), and the  $r_{ct}$  values are 1, 1.6, and 2.5 nm for the n-, c-, and bi-PbPc devices, respectively. Finally, from  $G_{ct}[= G(r_{ct})]$ , the free energy of the CT state marked by filled circles in Fig. B.3(c), I obtained  $\Delta G(= G_{cs} - G_{ct})$ , which are 57, 39, and 9 meV for the n-, c-, and bi-PbPc devices, respectively. The fact that  $\Delta G$  of the bi-PbPc device is smaller compared to the other devices indicates that the CT dissociation process in this device is thermodynamically more favored than that in the other devices, which is consistent with my expectation in the section of Exciton Diffusion Analysis that  $\eta_{cs}$  of the bi-PbPc is the highest. Note that what I intend in this section is to semi-quantitatively characterize the influences of the energetic terms such as  $\sigma$ ,  $E_{ct}$ , and the PbPc HOMO level on the CT-dissociation process, rather than rigorously calculating  $\Delta G$ . Although the accuracies of the LUMO level used in calculating Eq. (B.2) and the parameters assumed in calculating Eq. (B.4) – (B.7) such as the lattice constant, molecular density, and permittivity may have caused errors in the resulting values of  $\Delta G$ , the LUMO levels and the

parameters are not expected to be significantly different among the devices, and thus the trend of  $\Delta G$  are likely to remain valid.

From the  $\sigma_{ct}$  and  $J_{s0}$  values extracted from the fits to the temperature-dependent  $V_{oc}$ , I also determined, respectively, voltage losses due to energetic disorder at the D–A interface ( $\Delta V_{oc}^{ed} = \sigma_{ct}^2/2ekT$ ) and due to recombination of CT states [ $\Delta V_{oc}^{rec} = (kT/e) \log(J_{s0}/J_{sc})$ ], the second and third terms in Eq. (B.3), respectively. For  $\Delta V_{oc}^{rec}$  [black symbol, Fig. B.3(a)], it is noticeable that the bi-PbPc device shows a significant increase, which is due to its  $J_{s0}$  that is approximately one order of magnitude larger compared to the other devices. This increase in  $\Delta V_{oc}^{rec}$  causes  $V_{oc}$  of the bi-PbPc device to be smaller, compared to the n-PbPc device. The  $J_{s0}$  values were compared to the prefactor  $J'_{s0}$  of the energetic term in the dark saturation current density  $J_s$  in the ideal diode equation for organic heterojunctions, described by  $J_s = J'_{s0} \exp(-E_{cs}/kT)$  [28, 29].  $J_{s0}$  and  $J'_{s0}$ , which have the same physical origin but were derived using different methods, show a very similar trend. The change in the D–A interfacial area upon employing the template layers may cause the variation in  $J_{s0}$  [25]. To confirm this possibility, I performed atomic force microscope measurements on the surfaces of the three types of PbPc films. The results show that the root-mean-square roughness and the folding ratio (the ratio of the surface area of the topographical image to the scanning area of the image [30]) do not change significantly as the template layer is varied, meaning that the differences in D–A interfacial area cannot be the primary reason for the significant increase in  $J_{s0}$  and thus for the change in IQE and  $V_{oc}$ . I note that the increased  $J_{s0}$  of the bi-PbPc device does not necessarily conflict with the conclusion that the bi-PbPc has a larger  $\eta_{cs}$  than the c-PbPc. Rather, it suggests that enhanced intermolecular orbital coupling in this device also increases the rate of dissociation of CT excitons, the amount

of which is sufficiently large to increase IQE. Moreover, the fact that  $r_{ct}$  of the bi-PbPc is the largest indicates that CT states between non-adjacent PbPc and C<sub>60</sub> molecules are more likely to be present in the bi-PbPc device than in the other devices, leading to the increase in the total number of CT states, which in turn increases  $J_{s0}$ . Since the CT recombination rate and the number of CT states are strongly affected by intermolecular orbital coupling between donor and acceptor molecules [25], it is highly likely that the PbPc molecules in the bi-PbPc device, adopting the less face-on orientation, have enhanced intermolecular orbital coupling with C<sub>60</sub> molecules, thus giving rise to the increased  $J_{s0}$ . A similar conclusion, that upright and flat-lying ZnPc molecules have much weaker intermolecular orbital coupling with C<sub>60</sub> than those with intermediate (i.e., less face-on) orientations, was previously made based on quantum chemical calculations [30]. Figure B.3a also shows that  $\Delta V_{oc}^{ed}$  (blue symbols) of the n-PbPc device is the largest, while that of the c-PbPc device is the smallest. The degree of energetic disorder determined from this result is consistent with the degree of crystalline disorder inferred from my morphological study.

## B.3 Bibliography

- [1] T. K. Mullenbach, I. J. Curtin, T. Zhang, and R. J. Holmes, “Probing dark exciton diffusion using photovoltage,” *Nat. Commun.*, vol. 8, a. 14215, 2017.
- [2] R. R. Lunt, N. C. Giebink, A. A. Belak, J. B. Benziger, and S. R. Forrest, “Exciton diffusion lengths of organic semiconductor thin films measured by spectrally resolved photoluminescence quenching,” *J. Appl. Phys.*, vol. 105, no. 5, a. 053711, 2009.
- [3] H. Becker, S. E. Burns, and R. H. Friend, “Effect of metal films on the photoluminescence and electroluminescence of conjugated polymers,” *Phys. Rev. B*, vol. 56, no. 4, pp. 1893–1905, 1997.
- [4] C. Schwarz, S. Tscheuschner, J. Frisch, S. Winkler, N. Koch, H. Bässler, and A. Köhler, “Role of the effective mass and interfacial dipoles on exciton dissociation in organic donor-acceptor solar cells,” *Phys. Rev. B*, vol. 87, no. 15, a. 155205, 2013.
- [5] A. Ojala, A. Petersen, A. Fuchs, R. Lovrincic, C. Pölking, J. Trollmann, J. Hwang, C. Lennartz, H. Reichelt, H. W. Höffken, A. Pucci, P. Erk, T. Kirchartz, and F. Würthner, “Merocyanine/c60 planar heterojunction solar cells: Effect of dye orientation on exciton dissociation and solar cell performance,” *Adv. Funct. Mater.*, vol. 22, no. 1, pp. 86–96, 2012.
- [6] S. Gélinas, A. Rao, A. Kumar, S. L. Smith, A. W. Chin, J. Clark, T. S. van der Poll, G. C. Bazan, and R. H. Friend, “Ultrafast long-range charge separation in organic semiconductor photovoltaic diodes,” *Science*, vol. 343, no. 6170, pp. 512–516, 2014.

- [7] A. A. Bakulin, A. Rao, V. G. Pavelyev, P. H. M. van Loosdrecht, M. S. Pshenichnikov, D. Niedzialek, J. Cornil, D. Beljonne, and R. H. Friend, “The role of driving energy and delocalized states for charge separation in organic semiconductors,” *Science*, vol. 335, no. 6074, pp. 1340–1344, 2012.
- [8] P. Peumans, A. Yakimov, and S. R. Forrest, “Small molecular weight organic thin-film photodetectors and solar cells,” *J. Appl. Phys.*, vol. 93, no. 7, pp. 3693–3723, 2003.
- [9] G. Vaubel, H. Baessler, and D. Mobius, “Reaction of singlet excitons at an anthracene/metal interface: Energy transfer,” *Chem. Phys. Lett.*, vol. 10, no. 3, pp. 334–336, 1971.
- [10] T. M. Clarke and J. R. Durrant, “Charge photogeneration in organic solar cells,” *Chem. Rev.*, vol. 110, no. 11, pp. 6736–6767, 2010.
- [11] S. M. Menke and R. J. Holmes, “Exciton diffusion in organic photovoltaic cells,” *Energy Environ. Sci.*, vol. 7, no. 2, pp. 499–512, 2014.
- [12] O. V. Mikhnenko, P. W. M. Blom, and T. Q. Nguyen, “Exciton diffusion in organic semiconductors,” *Energy Environ. Sci.*, vol. 8, no. 7, pp. 1867–1888, 2015.
- [13] T. Forster, “Transfer mechanisms of electronic excitation,” *Radiation Res. Suppl.*, vol. 2, pp. 326–339, 1960.
- [14] B. P. Rand, D. P. Burk, and S. R. Forrest, “Offset energies at organic semiconductor heterojunctions and their influence on the open-circuit voltage of thin-film solar cells,” *Phys. Rev. B*, vol. 75, no. 11, a. 115327, 2007.

- [15] S. De, T. Pascher, M. Maiti, K. G. Jespersen, T. Kesti, F. L. Zhang, O. Inganäs, A. Yartsev, and V. Sundstrom, “Geminate charge recombination in alternating polyfluorene copolymer/fullerene blends,” *J. Am. Chem. Soc.*, vol. 129, no. 27, pp. 8466–8472, 2007.
- [16] J. B. W. H. J. C. F. D. A. L. Y.-L. K. A. Guan, Ze-Lei; Kim, “Direct determination of the electronic structure of the poly(3-hexylthiophene):phenyl-[6,6]-c61 butyric acid methyl ester blend,” *Org. Electron.*, vol. 11, no. 11, pp. 1779–1785, 2010.
- [17] A. J. Moule, M. C. Jung, C. W. Rochester, W. Tress, D. LaGrange, I. E. Jacobs, J. Li, S. A. Mauger, M. D. Rail, O. Lin, D. J. Bilsky, Y. B. Qi, P. Stroeve, L. A. Berben, and M. Riede, “Mixed interlayers at the interface between pedot:pss and conjugated polymers provide charge transport control,” *J. Mater. Chem. C*, vol. 3, no. 11, pp. 2664–2676, 2015.
- [18] K. Vandewal, K. Tvingstedt, A. Gadisa, O. Inganäs, and J. V. Manca, “Relating the open-circuit voltage to interface molecular properties of donor:acceptor bulk heterojunction solar cells,” *Phys. Rev. B*, vol. 81, no. 12, a. 125204, 2010.
- [19] J. C. J. L. Brédas, J. E. Norton and V. Coropceanu, “Molecular understanding of organic solar cells: The challenges,” *Acc. Chem. Res.*, vol. 42, no. 11, pp. 1691–1699, 2009.
- [20] I. W. Hwang, Q. H. Xu, C. Soci, B. Q. Chen, A. K. Y. Jen, D. Moses, and A. J. Heeger, “Ultrafast spectroscopic study of photoinduced electron transfer in an oligo(thienylenevinylene):fullerene composite,” *Adv. Funct. Mater.*, vol. 17, no. 4, pp. 563–568, 2007.

- [21] S. N. Hood and I. Kassal, “Entropy and disorder enable charge separation in organic solar cells,” *J. Phys. Chem. Lett.*, vol. 7, no. 22, pp. 4495–4500, 2016.
- [22] B. A. Gregg, “Entropy of charge separation in organic photovoltaic cells: The benefit of higher dimensionality,” *J. Phys. Chem. Lett.*, vol. 2, no. 24, pp. 3013–3015, 2011.
- [23] F. Gao, W. Tress, J. Wang, and O. Inganäs, “Temperature dependence of charge carrier generation in organic photovoltaics,” *Phys. Rev. Lett.*, vol. 114, no. 12, a. 128701, 2015.
- [24] V. B. J.-L. Yi, Yuanping; Coropceanu, “Exciton-dissociation and charge-recombination processes in pentacene/c60 solar cells: Theoretical insight into the impact of interface geometry,” *J. Am. Chem. Soc.*, vol. 131, no. 43, pp. 15777–15783, 2009.
- [25] T. M. Burke, S. Sweetnam, K. Vandewal, and M. D. McGehee, “Beyond langevin recombination: How equilibrium between free carriers and charge transfer states determines the open-circuit voltage of organic solar cells,” *Adv. Energy Mater.*, vol. 5, no. 11, a. 1500123, 2015.
- [26] J. Hwang, A. Wan, and A. Kahn, “Energetics of metal-organic interfaces: New experiments and assessment of the field,” *Mater. Sci. Eng. R Rep.*, vol. 64, no. 1-2, pp. 1–31, 2009.
- [27] J. P. Sethna, *Statistical Mechanics: Entropy, Order Parameters, and Complexity*. Oxford ; New York: Oxford University Press, 2006.
- [28] J. D. Zimmerman, X. Xiao, C. K. Renshaw, S. Wang, V. V. Diev, M. E. Thompson, and S. R. Forrest, “Independent control of bulk and interfa-

cial morphologies of small molecular weight organic heterojunction solar cells,” *Nano Lett.*, vol. 12, no. 8, pp. 4366–4371, 2012.

- [29] N. C. Giebink, G. P. Wiederrecht, M. R. Wasielewski, and S. R. Forrest, “Ideal diode equation for organic heterojunctions. i. derivation and application,” *Phys. Rev. B*, vol. 82, no. 15, a. 155305, 2010.
- [30] B. P. Rand, D. Cheyons, K. Vasseur, N. C. Giebink, S. Mothy, Y. P. Yi, V. Coropceanu, D. Beljonne, J. Cornil, J.-L. Brédas, and J. Genoe, “The impact of molecular orientation on the photovoltaic properties of a phthalocyanine/fullerene heterojunction,” *Adv. Funct. Mater.*, vol. 22, no. 14, pp. 2987–2995, 2012.

## 요 약 (국문초록)

# 유기 광전자소자에서의 빛-물질 사이 상호작용의 나노광학적 제어

김 형 채  
나노융합학과  
융합과학기술대학원  
서울대학교

물질의 광 특성은 물질 자체의 특성 뿐만 아니라 그 주변의 전자기적 환경에 영향을 받는다. 예를 들어서, 금속-절연체-금속 구조의 발광 다이오드 또는 포토다이오드는 페브리-페롯 공명모드가 여기 되도록 절연체의 두께가 적절히 조절되었을 때 광추출 또는 광흡수 효율이 극대화 된다. 금속-절연체 계면에서 발생하며 높은 광자상태밀도를 특징으로 하는 플라즈모닉 모드는 자연에 존재하지 않는 완전 흡수체 또는 초고속 발광체를 구현하는데 이용될 수 있다. 키랄성 패턴을 포함하고 있는 나노캐비티 구조는 키랄성 분자의 키랄-광학적 특성을 증폭하거나 비키랄성 분자의 키랄-광학적 특성을 유도하는데 사용될 수 있다. 본 연구의 목표는 나노광학적 플랫폼으로 이용해서 유기 광전자소자의 전자기적 환경을 제어하고 이를 통해서 성능을 향상시키거나 이들에게 새로운 기능을 부여하는 것이다. 유기 분자가 광흡수 및 발광 특성이 우수할 뿐만 아니라 분극률의 조절이 용이해서 소자 내부의 빛-물질 상호작용을 맞춤 제어하기에 적합하기 때문에 광활성층의 재료로써 주로 유기 분자가 이용되었다. 유기태양전지 분야에서 난제로 남아있는 두 이슈인 근적외선 영역의 낮은 광흡수율 문제와 광자에너지의 열손실 문제를 해결하기 위해서 나는 두 종류의 태양전지 구조를 새롭게 제안하였으며 1차원 나노캐비티 구조인 이 태양전지의 광 특성을 최적화 하기 위해서 전달행렬방식의 시뮬레이션을 이용하였다. 또한 원편광 발광 소자의 키랄-광학적

특성에 대한 포괄적인 연구를 최초로 수행 되었으며, 이를 통해서 거울 반사에 기인한 원편광 상태의 소멸 문제를 극복하고 이성적으로 고성능 소자를 제작 할 수 있는 방법을 제안 하였다.

다음으로, 키랄성 나노캐비티가 비키랄성 분자의 원편광 이색성을 유도하는 광플랫폼으로 이용될 수 있음을 3차원 광시뮬레이션을 이용해서 보였다. 키랄성 캐비티 내부에서는 원편광 상태에 따라서 플라즈모닉 핫스팟이 선택적으로 여기되는 것이 관측되었으며 이는 전자기 모드 분석을 통해서 상부와 하부전극에서 발생하는 표면플라즈몬 모드 간의 혼성화에 기인한 현상임을 밝혀내었다. 키랄성 나노캐비티 기반의 유기포토다이오드는 본 연구에서 최초로 수치해석적으로 시연 되었으며 이들은 기존에 최고의 성능을 보여주던 분자 기반의 소자들과 비교했을 때 양자효율과 원형편광 비대칭성 측면에서 우수한 결과를 나타내었다. 나아가, 키랄성 나노캐비티는 현존하는 유기발광다이오드 기반 디스플레이의 에너지 효율을 크게 향상시키는데 이용되거나 삼차원 디스플레이 소자와 편광 반응성 광센서에 사용될 수 있으며 나아가 양자정보 시스템의 빌딩블록으로 응용될 것으로 기대된다.

**주요어:** 나노포토닉스, 플라즈모닉스, 유기발광다이오드, 유기태양전지, 유기광 검출기, 유기반도체, 키랄성

**학번:** 2011-23984